

Review

Fuel Cell Types, Properties of Membrane, and Operating Conditions: A Review

Noor H. Jawad ¹, Ali Amer Yahya ¹, Ali R. Al-Shathr ¹, Hussein G. Salih ¹, Khalid T. Rashid ¹,
Saad Al-Saadi ^{2,*}, Adnan A. AbdulRazak ¹, Issam K. Salih ³, Adel Zrelli ⁴ and Qusay F. Alsalhy ^{1,*}

¹ Membrane Technology Research Unit, Chemical Engineering Department, University of Technology—Iraq, Alsen'a Street No. 52, Baghdad 10066, Iraq

² Department of Mechanical and Aerospace Engineering, Monash University, Clayton, VIC 3800, Australia

³ Department of Chemical Engineering and Petroleum Industries, Al-Mustaqbal University College, Babylon 51001, Iraq

⁴ Higher Institute of Applied Science and Technology of Gabes, University of Gabes, Gabes 6072, Tunisia

* Correspondence: saad.al-saadi@monash.edu (S.A.-S.); qusay.f.abdulhameed@uotechnology.edu.iq (Q.F.A.)

Abstract: Fuel cells have lately received growing attention since they allow the use of non-precious metals as catalysts, which reduce the cost per kilowatt of power in fuel cell devices to some extent. Until recent years, the major barrier in the development of fuel cells was the obtainability of highly conductive anion exchange membranes (AEMs). On the other hand, improvements show that newly enhanced anion exchange membranes have already reached high conductivity levels, leading to the suitable presentation of the cell. Currently, an increasing number of studies have described the performance results of fuel cells. Much of the literature reporting cell performance is founded on hydrogen-anion exchange membrane fuel cells (AEMFCs), though a growing number of studies have also reported utilizing fuels other than hydrogen—such as alcohols, non-alcohol C-based fuels, and N-based fuels. This article reviews the types, performance, utilized membranes, and operational conditions of anion exchange membranes for fuel cells.

Keywords: fuel cells; anion exchange membrane; PEMFC; hydroxide exchange membrane; performance of AEMFC



Citation: Jawad, N.H.; Yahya, A.A.; Al-Shathr, A.R.; Salih, H.G.; Rashid, K.T.; Al-Saadi, S.; AbdulRazak, A.A.; Salih, I.K.; Zrelli, A.; Alsalhy, Q.F. Fuel Cell Types, Properties of Membrane, and Operating Conditions: A Review. *Sustainability* **2022**, *14*, 14653. <https://doi.org/10.3390/su142114653>

Academic Editor: Agostina Chiavola

Received: 3 October 2022

Accepted: 3 November 2022

Published: 7 November 2022

Publisher's Note: MDPI stays neutral with regard to jurisdictional claims in published maps and institutional affiliations.



Copyright: © 2022 by the authors. Licensee MDPI, Basel, Switzerland. This article is an open access article distributed under the terms and conditions of the Creative Commons Attribution (CC BY) license (<https://creativecommons.org/licenses/by/4.0/>).

1. Introduction

Rapid industrialization and a massive increase in the global population are the main reasons for the energy crisis and current resource deficiency. The global population is continuing to grow, increasing the demand for energy resources. The combustion of primary energy sources (fossil fuels, for example, coal, natural gas, and oil) produces greenhouse gas emissions and harms human health. Additionally, combustion is an incompetent conversion of chemical energy into electrical energy according to the second law of thermodynamics [1]. Over the earlier decades, the exhaustion and ineffective use of energy sources have been observed as the utmost critical issues in energy policy planning. The severe nature of these issues has led to an excessive rise in the request for new renewable energy technologies [2]. In latest years, clean energy technologies, for example, fuel cells, solar energy, wind power, and hydropower, are progressively preferred by governments and scientists. Of all types of renewable and new energy technologies, fuel cells are receiving growing attention since they can directly change chemical energy to electrical energy through the oxidation of fossil fuels that are devoid of discharged hazardous chemicals [3]. Fuel cells have potential in different implementations, for instance, portable power, vehicle propulsion, immobile electricity generation, and huge electrical plants. The fuel cells are categorized as reliant on several factors, such as conditions for the duration of operation (humidity, pressure, temperature), the structure of the fuel cell (implementation system and scale), and the appearance of the polymer electrolyte of the fuel cell [4].

Fuel cells appeared as green energy technology. Such an electrochemical system converts the chemical energy stored in H_2 into electricity. These electrochemical systems are developing technologies whose implementation is not limited to geographic constraints [5]. In the history of fuel cell improvement, alkaline fuel cells (AFCs) have been used as the first fuel cell technology in external space. Nevertheless, to discover the implementations of fuel cells on earth, polyelectrolyte membrane fuel cells (PMFCs) have concerned the attention of the research community because of the introduction of ion-exchange polyelectrolytes (H^+/OH^-) as solid electrolytes, which address the issues related with liquid-electrolyte leaks and the variability of electrolytes in anion fuel cells [6].

The first to report such cell performance were Lu et al. [7], who exhibited in 2008 a Ni–Cr anode and Ag catalyzed cathode with a favorable peak power density of 50 mW/cm^2 . Five years later, two more studies attained peak power densities of 76 and 40 mW/cm^2 , developing the membrane fuel cells founded on Ni/Ag and NiW/CoPPY-based (anode/cathode) electrocatalysts, respectively [8]. The anion exchange membrane fuel cells have attained significant attention, as illustrated in Figure 1, showing the number of publications in the anion exchange membrane fuel cells field since 2000. More than 2000 publications were reported on this technology over the years, whereas most were published in just the past four years, suggesting that this technology is a blooming research area in fuel cell technology. Most of the studies in the anion exchange membrane fuel cell field have been applied in various countries worldwide, with the maximum number of reports originating from China and North America [9].

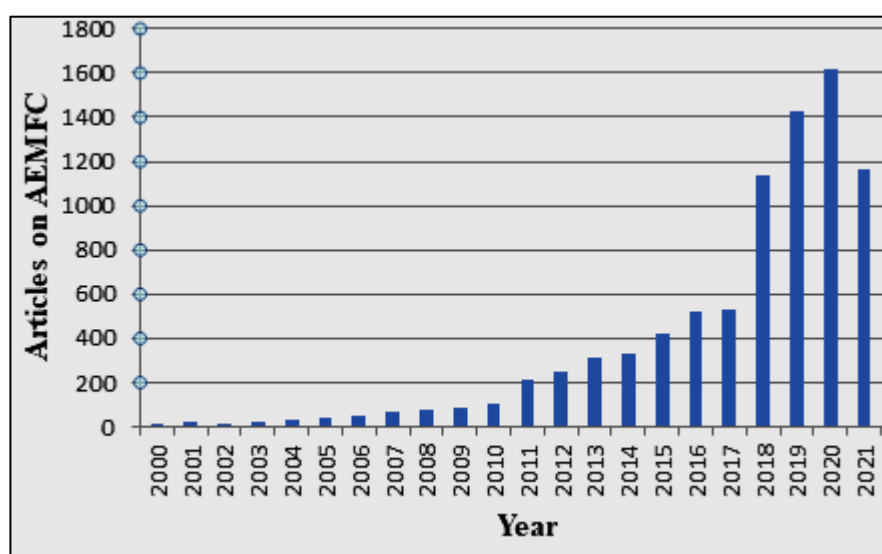


Figure 1. The number of research articles published on anion exchange membrane fuel cells.

Fuel cells that are under enormous study can be categorized into several types: viz, polymer exchange membrane fuel cells (i.e., proton exchange membrane fuel cells (PEMFCs)), alkaline fuel cells (AFCs), solid oxide fuel cells, phosphoric acid, and molten carbonate fuel cells [10]. Anion exchange membrane fuel cells are the utmost favorable alternative over PEMFCs. Over the past two decades, they have drawn incredible research interest due to several unique properties such as improved oxygen reduction kinetics, non-precious metal catalysts, minor corrosion, easy water management, and better fuel oxidation. As the major component of the anion exchange membrane fuel cells, anion exchange membrane (AEM) should have vital qualities such as low swelling ratio, good hydroxide conductivity, and prolonged alkaline stability [11]. The low-performance stability is mainly produced by the chemical removal of the anion conducting ionomers because of the high pH environment existing for the duration of the procedure of the fuel cell [12–14].

The development of different functional groups of the anion exchange membrane improved its stability in hydrated alkaline environments [15–21]. However, numerous

recent studies found that the high pH environment combined with a low hydration level at the cathode side of the cells could clarify the chemical degradation [22–24] and the decay in performance for the duration of the AEMFC process [9,25]. For instance, the high pH and low hydration levels expose the quaternary ammonium (QA) cation functional groups in the ionomer to chemical attack via poorly solvated and extremely reactive hydroxide anions [23]. This breakdown of the monomeric materials in the cell leads to a continuous harmful reduction in ion exchange capacity (IEC) which, in sequence, results in a continuous reduction in ionic conductivity and a rise in cell resistance, leading to a quick reduction in performance [9].

2. Classifications of Fuel Cells

Currently, five significant kinds of fuel cells can be recognized according to the type of electrolyte [26]. Any fuel cell is divided into three main components. The electrodes, electrolyte, and external circuit constitute a single fuel cell. Inter-connector plates are often used when it is desired to stack multiple fuel cells.

2.1. Alkaline Fuel Cells (AFCs)

A significant advantage of Alkaline Fuel Cell (AFC) technologies is the capability to use more abundant, inexpensive, and non-platinum catalysts [27]. While the air containing oxygen is fed across the cathode electrode, the fuel (H_2) is supplied over the anode. Generally, the liquid electrolyte used in an AFC is an aqueous KOH electrolyte. However, any CO_2 in the air feed stream leads to carbonate precipitation via the formation of large metal carbonate crystals, which possibly will close the pores of the gas diffusion layer on the electrode [28]. If electrolyte concentration is not high enough, water molecules and electrons are produced due to the reaction of hydroxyl ions from the cathode through the electrolyte and the hydrogen charged at the anode. The electrons are then transported through the external circuit back to the cathode, where the hydroxyl ions have been formed due to an oxygen reaction with water molecules (see Figure 2).

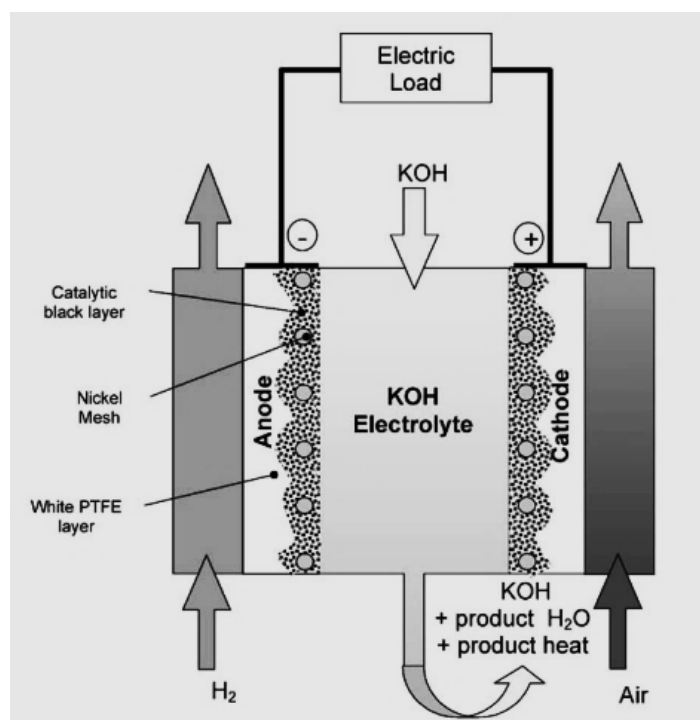
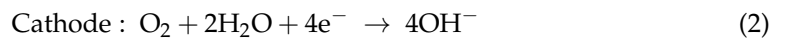
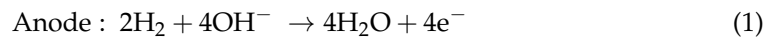


Figure 2. Alkaline fuel cell composition [28].

The reaction can be represented as follows:



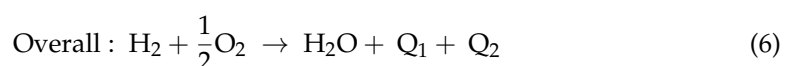
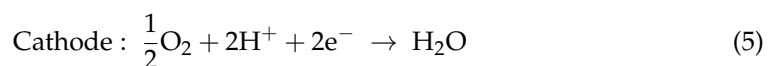
reduced by re-circulating the electrolyte, which raises the cell's efficiency, and the water generated can be removed by evaporation [29]. In AFCs, the reaction kinetics are more facile, resulting in higher cell voltages [30]. Compared to SOFC (>700 °C) and other fuel cells, AFCs are relatively easy to handle and have a rather low operating temperature (23–70 °C) [29]. AEMs are solid polymer electrolyte membranes that include positive ionic sets (normally quaternary ammonium (QA) functional sets, for example, poly-NMe⁺³) and moveable negatively charged anions. A widely quoted attention with AEMs is membrane stability, especially at raised temperatures [31,32]. The prevalent matters are:

1. The diffusion coefficients and motilities of OH[−] anions are fewer than H⁺ in many media and quaternary ammonium ionic sets are not as much dissociated as the standard sets of sulfonic acid where (acid dissociation constant) pK_a for sulfonic acid sets are usually −1. However, for quaternary ammonium groups, the associated pK_b values are approximately +4. There were worries that AEMs would not have sufficient intrinsic ionic conductivities for implementation in fuel cells [33].
2. The OH[−] anions are active nucleophiles that potentially cause removal by using (a) a direct nucleophilic dislocation and/or (b) a Hofmann removal reaction when a b-hydrogen is present; it is possible that OH[−] will also displace methyl groups (−CH₃), forming tertiary amines and methanol [31,32]. If the AEMs include good leaving sets (e.g., QA −NMe⁺³ sets), then the chemical stability of the AEMs may have been insufficient for use in fuel cells, mainly at elevated temperatures.
3. The precursor anion-exchange membranes are usually immersed in aqueous NaOH/KOH solutions to convert them to the OH[−] form AEM. The anion exchange membrane should have the chemical stability to endure this process. A decade ago, the stabilities of different benzyltrimethylammonium-based AEMs were tested and found to be stable up to 75 °C in NaOH_{aq} at concentrations up to 6 mol/dm³ for many days [34].

2.2. Proton Exchange Membrane Fuel Cells (PEMFCs)

Among all kinds of fuel cells, the proton exchange membrane fuel cell (PEMFC) has become extensively accepted for powering electric devices and vehicles [35]. Proton exchange membrane fuel cells, which ordinarily produce electricity over a chemical reaction amid hydrogen and oxygen or an additional oxidizing agent, have become more abundant in recent years because of their inherent benefits [36]. PEMFCs have several outstanding features, for example, high energy density; high energy efficiency; low working noise; low general cost; low working temperature; sulfur oxides, zero emissions of nitrogen oxides and CO₂; short startup time; zero corrosion; use of solid electrolytes; and long life [37]. The protons formed at the anode are transferred to the cathode through the proton exchange membrane, whereas electrons are transferred through graphite plates from the anode to the cathode via an external circuit. Oxygen and electrons generate water and heat at the cathode side. The proton exchange membrane is the heart of the fuel cell [38]. The basic design of the mono-proton exchange membrane fuel is displayed schematically in Figure 3.

The chemical reactions followed in the fuel cell are displayed below:



where Q₁ is electrical energy and Q₂ is heat energy.

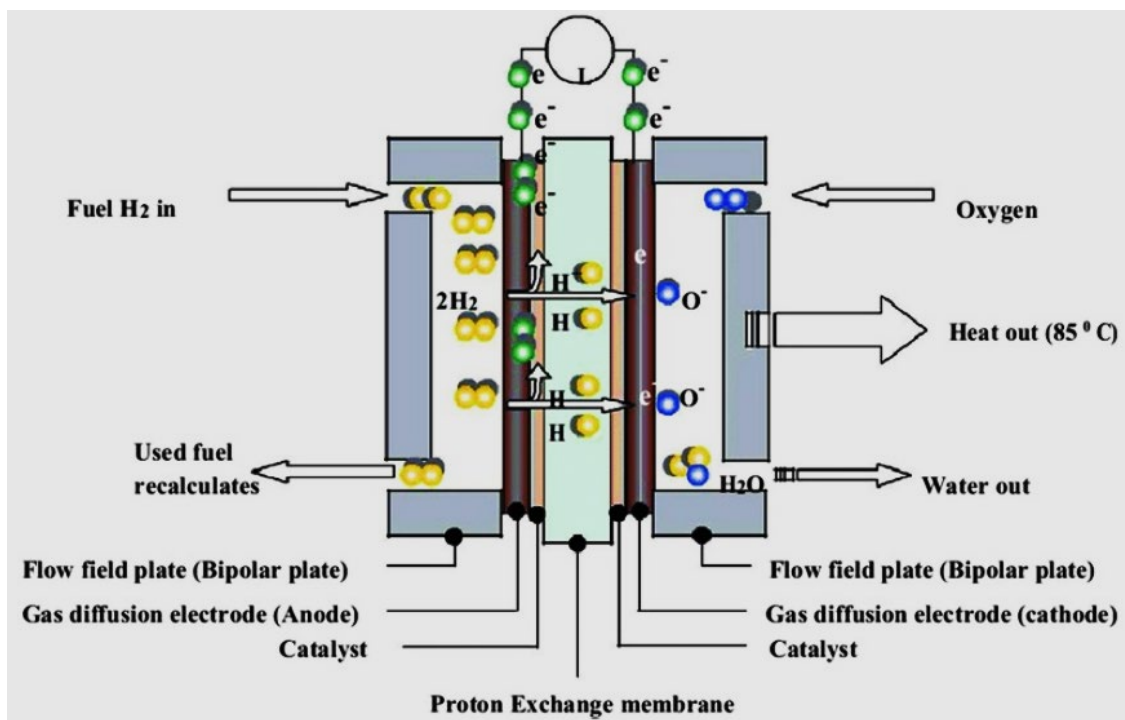


Figure 3. Operating Principle of PEMFC [35].

The sulfonated aromatic polymer is an ideal raw material for proton exchange membranes and is synthesized from industrialized monomers. Furthermore, its physicochemical features can be regulated via functionalizing monomers or adjusting the last polymer. Thus, as a substitute proton exchange membrane, the sulfonated aromatic polymer has made significant progress in the synthesis [39]. Generally, these sulfonated polymers need low equivalent weights (EW) to attain high electrical conductivity [40]. Unfortunately, low water content typically leads to high water content absorption and even the loss of mechanical features of membranes; nevertheless, sulfonated membrane crosslinking post-treatment can limit the absorption of water via sacrificing proton conductivity [41]. So, it is essential to preserve good proton conductivity and decrease water absorption to attain high mechanical properties.

A series of sulfonated poly (fluorene ether ketone nitriles) with low EW were created via one-step polycondensation from marketable raw materials. Varying from the conventional sulfonated aromatic polymers, they have high proton conductivity and a sudden decrease in water uptake. Additionally, they present excellent thermal and chemical stability. These features provide it with vast implementation visions in high-temperature PEMFCs [42].

2.3. Solid Oxide Fuel Cells (SOFCs)

The solid oxide fuel cell is a power production technology that, step by step, varies the traditional main scheme of power source into a decentralized scheme of power source and directly fits power generation with the consuming of power needs at the household position [43]. An essential benefit of this structure is its simple structure that does not need a separator or gas storage [44]. The electrochemical charge transference reaction and restructuring reaction happen in solid oxide fuel cells. On the cathode (air electrode), oxygen molecules attain electrons and are decreased to ions of oxygen. Under the action of an electric field, ions of oxygen transfer to the anode through the vacancies of oxygen in the electrolyte to trigger an oxidation reaction with fuel CH_4 or H_2 and electrons produce a current through external circuits, as displayed in Figure 4. The chemical potential energy (or Gibbs free energy) of the global reaction of the fuel and oxidant is transformed into

electricity and heat for the duration of the chemical reaction. The electrochemical reactions on the cathode and anode in solid oxide fuel cell are exothermic [45].

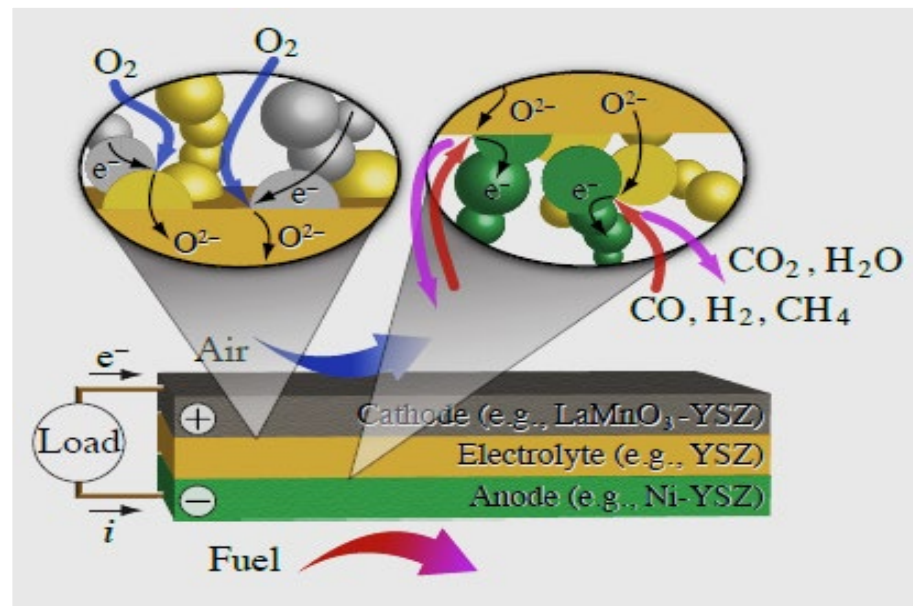


Figure 4. The basic operational principles of solid oxide fuel cell membrane electrode assembly (MEA). In the left bubble, oxygen molecules are dropped at the cathode and oxygen ions are conducted over the electrolyte. The ions of oxygen are transferred by the electrolyte to the anode (right bubble), where they are utilized for electrochemical oxidation of fuel at the three-phase boundary. Electrons free in the charge-transfer reactions are conducted over the anode (metal) to the external circuit [45].

The traditional materials utilized for solid oxide fuel cell cathodes and oxygen separation membranes are perovskites, for example, ferrites-nickelates (LSFN), Sr-doped La manganites (LSM), and ferrites-cobaltites (LSFC). Regardless of the high electronic (for LSM) or mixed ionic-electronic (for LSFC and LSFN) conductivity (from $\sim 10^2$ to 10^3 S/cm at 700 °C), these materials have subjects concerning their thermomechanical and chemical compatibility with electrolyte materials' lengthways (variations in the thermal expansion coefficient and formation of poor conducting Sr and La zirconates/cerates at the cathode-electrolyte interface) with their low stability to carbonization that limits their implementation [46]. Renouncing the strategy of doping the A-site with alkaline earth metal cations is one probable method to progress the chemical stability of perovskite materials (such materials are more stable to carbonization) [47–49] in addition to utilizing host A-cations with smaller ionic radii (such as Pr⁺³ [50]) since their zirconated and cerates are thermodynamically unstable [48,51,52]. Pr nickelates-cobaltites (PNC) are promising materials for solid oxide fuel cell cathodes and perm-selective layers of membranes of oxygen separation because of their compatibility with electrolytes (for example, doped ceria), their stability to carbonization and their higher oxygen transference characteristics (the oxygen tracer diffusion coefficient (D^*) value is up to $\sim 10^{-8}$ cm²/s at 700 °C) [53–55].

2.4. Phosphoric Acid Fuel Cells (PAFCs)

In phosphoric acid fuel cells, hydrogen can be produced in situ from methanol (or similar liquid fuel) compared to the traditional techniques where the compressed liquid hydrogen is used directly. Thus, the phosphoric acid fuel cells are working by utilizing accessible schemes of distribution and refueling [56]. A phosphoric acid fuel cell typically houses phosphoric acid (H₃PO₄, PA) trapped in a matrix (usually silicon carbide, SiC) as the electrolyte. Platinum with various loadings on carbon-based gas diffusion layers produces the electrodes, i.e., cathode and anode. The fuel source and the oxidant are circulated via bipolar plates (BPPs) on opposed sides of the electrolyte, as shown in Figure 5.

However, hydrogen is oxidized to electrons and protons at the anode. While the electrons route via the external circuit, the protons pass through the electrolyte. The oxygen is combined with the protons and electrons at the cathode for water production and the heat released during the reaction is generally utilized for heating water and space heating [57].

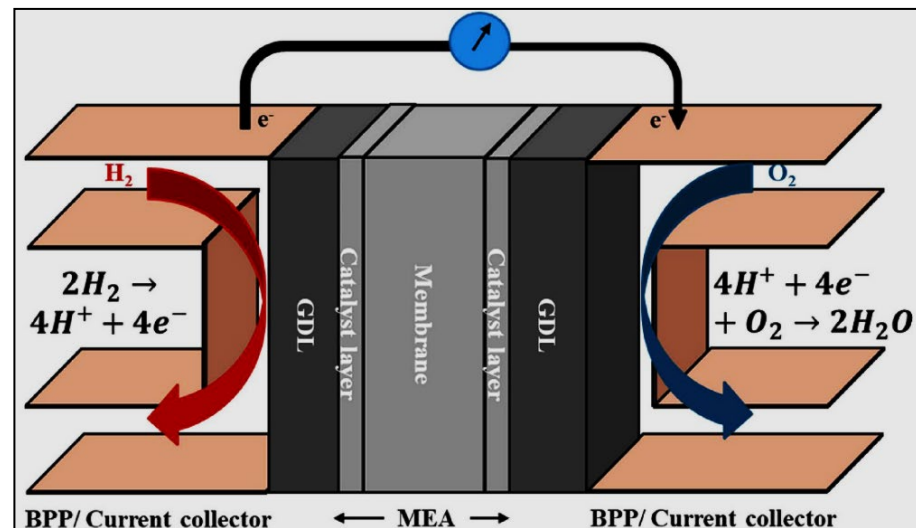


Figure 5. Constructional details and operating of a phosphoric acid fuel cells [57].

The overall Ohmic overpotential (η_{ohmic}) acquired in the cell is the totality of the losses because of the resistance of the membrane ($\eta_{membrane}$) and interfacial contact resistance (ICR) (η_{ICR}). If the membrane is hydrated sufficiently, it conducts protons efficiently, thus offering less resistance. On the other hand, a cell with insufficient clamping pressure will face high contact resistance subsequent to a significant ohmic drop. A correctly clamped cell is observed to have an interfacial contact resistance of almost 55% of the overall ohmic resistance (Figure 6) [58].

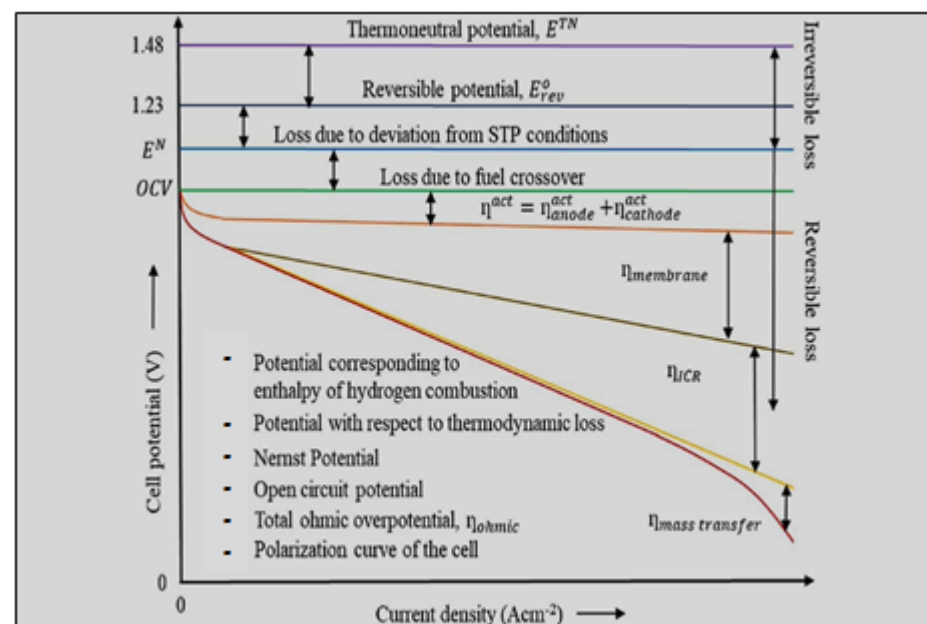


Figure 6. Characteristic curve of phosphoric acid fuel cells [57]. η_{anode}^{act} = anode activation overpotential; the quantity of energy essential to overwhelm the anode reaction activation barrier, $\eta_{cathode}^{act}$ = cathode activation overpotential; the quantity of energy essential to overwhelm the cathodic reaction activation barrier, and η^{act} = total activation overpotential of the reaction.

2.5. Molten Carbonate Fuel Cells (MCFCs)

As a high-temperature fuel cell, a molten carbonate fuel cell has an extensive range of fuel bases and does not depend on valuable metals as electrode catalysts. Additionally, molten carbonate fuel cells can be united using gas or steam turbines to attain collective power and heat, beneficent energy use, and conversion effectiveness [59]. The molten carbonate fuel cell arranges a mixing of alkali carbonates as the electrolyte and works at intermediary temperatures (550–650 °C) utilizing carbonaceous fuels such as natural gas. The important electrochemistry of a molten carbonate fuel cell includes the construction of carbonate ions (CO_3^{2-}) at the cathode via the mixture of O_2 , CO_2 , and two electrons; the passage of the ions carbonate to the anode over a carbonate-containing electrolyte (“matrix”); and, lastly, the reaction of the carbonate ion with hydrogen at the anode produces CO_2 , H_2O , and two electrons as displayed in Figure 7. The subsequent electrochemical reactions occur [60]:

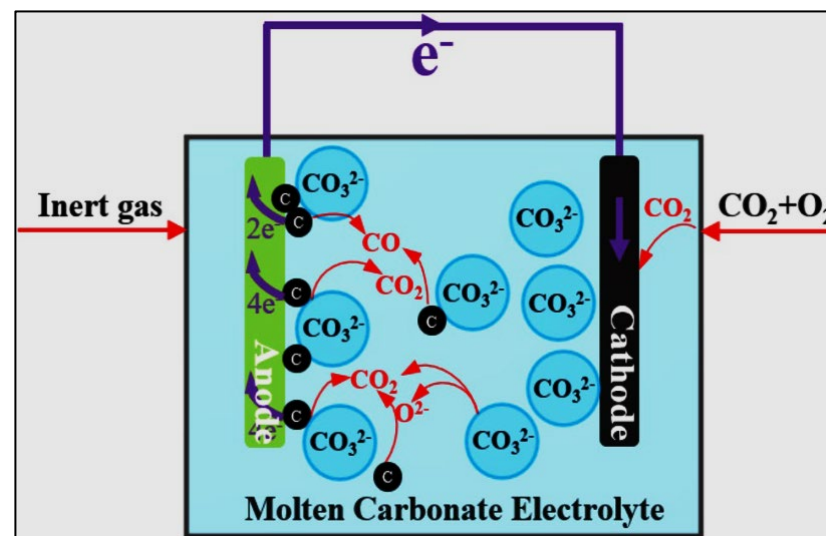
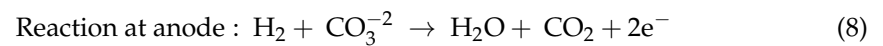
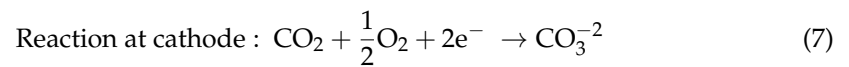


Figure 7. Schematic of the MCFC system: oxygen and carbon dioxide attain electrons to generate carbonate ions, carbon generates CO_2 or CO and electrons at the anode, and carbonate ions at the cathode. At the same time, the carbonate ion can possibly decompose into O^{2-} and CO_2 [61].

Figure 8 presents a graphical illustration of the system configuration. The reforming unit was equipped with water vapor and pre-heated fuel, which interacted with the catalytic combustion burner on a thermal basis to achieve the heat essential for reforming. Fuel products that were reformed arrived in the anode chamber containing CO_2 , H_2 , CO , and H_2O . In the catalytic combustion burner (CCB), the air supplied by the mechanical blower was mixed with the remaining fuels lengthways with a portion of the remaining air generated by the cathode. For the electrochemical processes in the stack of fuel cells, the cathode input was supplied with hot CO_2 -enriched air. The water vapor and fuel combinations were pre-heated using the hot consumed gas leftovers leaving the cathode and released into the atmosphere as evaporated water.

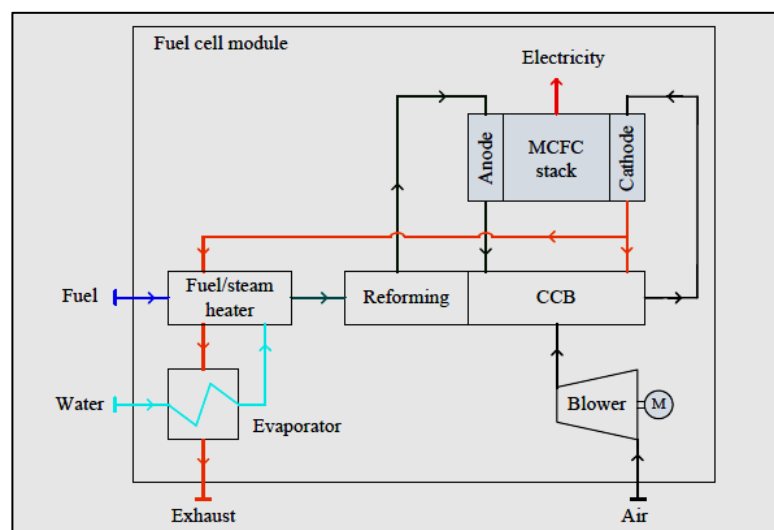


Figure 8. A standalone MCFC (molten carbonate fuel cell) module schematic diagram [62].

Regarding the technology of the membrane, utilized in a varied range of implementations for gas separation, many membrane kinds have been examined for CO₂ capture: inorganic, polymeric, mixed, facilitated transport membranes, hybrid, and capillary membranes, though most are for small-scale implementations. Mixed matrix membranes are a well-known route to improve the properties of the membrane. Their microstructure involves an inorganic material in the form of micro- or nanoparticles (discrete phase) incorporated into a polymeric matrix (continuous phase). Using two materials each with a different flux and selectivity delivers the probability of better designing a membrane for capturing CO₂ by permitting the synergistic mixture of polymers' easy process capabilities and the superior gas separation performance of inorganic materials. If scale-up problems were to be resolved, they would offer substantial advantages over absorption processes only for flue gases with a CO₂ content exceeding 20% [63–66].

Due to the MCFC CO₂-concentrating effect, the membrane separation sizing for the 800 MW Natural Gas Combined Cycles has a 4-fold lower feed flow and a 3.6-fold higher CO₂ concentration than the reference. Polyethylene oxide (PEO) is a promising material for CO₂-selective membranes due to its strong affinity to CO₂. Hence, CO₂ permeates selectively through the membrane and H₂ retains at the high-pressure feed side. High-pressure H₂ can therefore be produced without additional recompression since Kawakami et al. [67] found that PEO had a high CO₂ affinity. The membrane permeability and selectivity are based on [68,69]. This selectivity is consistent with the findings of Chen et al. [70] for CO₂/H₂ and CO₂/N₂ in the polymer-ionic liquid blend. Table 1 summarizes the fuel cell types according to their main components (viz, electrodes, electrolytes, and external circuits).

Table 1. The fuel cell types and their main components (electrodes, electrolyte, and external circuits).

Types of Fuel Cells	The Main Components of Fuel Cells		
	Electrodes	Electrolyte	External Circuit
Alkaline Fuel Cells (AFCs)	<p>✓ The electrodes consist of a double-layer structure: an active electrocatalyst layer and a hydrophobic layer. The active layer is composed of an organic mixture (carbon black, catalyst, and PTFE) that is ground and then rolled at room temperature to cross-link the powder and form a self-supporting sheet. The hydrophobic layer prevents the electrolyte from leaking into the reactant gas' low channels and ensures diffusion of the gases to the reaction site [28].</p>	<p>➤ AFCs use liquid KOH (a potassium hydroxide solution) as an electrolyte and are fueled by hydrogen. The oxidant must be pure oxygen, not air, due to the carbonation of the electrolyte by CO₂ content. The alkaline electrolyte means that carbon dioxide, which degrades (carbonates) the electrolyte, must be eliminated. Only highly purified hydrogen and oxygen can be used, the cost of which imposes a severe limitation to applications other than space [71]. Inorganic materials such as layered perovskite-type oxides such as LaSr₃Fe₃O₁₀, NaLaTiO₄, Sr₄Co_{1.6}Ti_{1.4}O₈(OH)₂·xH₂O, RbLaNb₂O₇, LaFeO₃, and NaCo₂O₄ have been used as the electrolyte in the alkaline fuel cell, but the study of these new inorganic electrolyte membranes is still in its infancy [27].</p>	<p>❖ AFCs produce electricity through oxidation-reduction reactions between oxygen and hydrogen. Water is generated from the chemical reaction and two electrons are released. The electrons flow through an external circuit and return to the cathode oxygen reduction in an electrochemical reaction; thus, hydroxide ions are produced. Electricity is created as a byproduct of this product [72]. The electronic charge balances the flow of ionic charge through the electrolyte and the external circuit, producing electricity up to 20 KW [28].</p>
Proton Exchange Membrane Fuel Cells (PEMFCs)	<p>✓ Anode and cathode are carbon-supported platinum deposited on both sides of a proton-conducting polymer membrane (electrolyte), and the assembly is called a Membrane Electrode Assembly (MEA), where the dissociation of hydrogen generates protons and electrons using the platinum catalyst [39].</p>	<p>➤ Careful monitoring of the electrolyte/acid structure and its leaching is also necessary to understand the performance degradation of the device. The widely used phosphoric acid and recently introduced phosphonic acid (and their derivatives) play a vital role in the proton conductivity of PEMFCs. These acids mostly undergo degradation because of high temperatures and oxidative degradation. Phosphonic acid and its derivatives degrade by condensation resulting in an adverse effect on the conductivity of the membrane. Moreover, the thermal stability of the electrolyte/acid could be improved by using additives. The addition of 20 wt% of perfluoroalkyl phosphonic acid (C₂F₅PO₃H₂ and CF₃PO₃H₂) in H₃PO₄ could lead the electrolyte mixtures to show excellent thermal stability for high-temperature PEMFCs operating between 140 and 200 °C [73].</p>	<p>❖ The electrons transfer from the anode side to the cathode side through an external circuit, while the proton will transfer through the electrolyte layer at the cathode side. The oxygen gas reacts with electrons and protons to generate water. The produced electrical power is up to 250 KW [38]. The ohmic polarization in the circuit of PEMFCs varies directly with the current, increasing over the entire range of the current because the cell resistance remains essentially constant. Ohmic losses occur due to the resistance of the electron transfer between electrodes and the protons traveling through the solid polymer membrane. The dominant ohmic losses through the electrolyte are reduced by decreasing the electrode separation and enhancing the ionic conductivity of the electrolyte [74].</p>
Solid Oxide Fuel Cells	<p>✓ The electrode consists of anode materials, particularly in the context of carbon deposition and tolerance to sulfur poisoning. However, the traditional materials utilized for solid oxide fuel cell cathodes and oxygen separation membranes are perovskites, for example, ferrites-nickelates (LSFN), Sr-doped La manganites (LSM), and ferrites-cobaltites (LSFC) [46].</p>	<p>➤ The electrolyte usually consists of a dense solid metal oxide. One of the most common electrolyte materials in SOFCs is yttria-stabilized zirconia (YSZ)-zirconia (ZrO₂) with 8% yttrium added as a dopant. In the temperature range of 650–1000 °C, YSZ is a good conductor of oxygen ions O²⁻ [45]. Other doped zirconia materials with higher ionic conductivities, such as Sc- and Yb-stabilized zirconia, are suggested to lower the cell working temperature. However, only YSZ provides a compromising combination of stability and ionic transport properties among doped zirconia-based electrolyte materials [47].</p>	<p>❖ Electrons from the chemical reaction at the anode surface must be transported to the external circuit. Since the electrolyte has a large surface area, a metallic-screen current collector is used to reduce the distance electrons must travel in the anode itself; the electrons are transported long distances to the external circuit by the current collector. Nevertheless, resistive losses within the anode must be minimized by having a catalytic anode that is an excellent electronic conductor. If the anode supports the thin ceramic electrolyte, the electrons must travel a longer distance in the anode to reach the current collector, which requires a higher electronic conductivity of the catalytic anode material [75]. The resultant electricity is near >200 KW [47].</p>

Table 1. Cont.

Types of Fuel Cells	The Main Components of Fuel Cells		
	Electrodes	Electrolyte	External Circuit
Phosphoric Acid Fuel Cells (PAFCs)	✓ Platinum with various loadings on carbon-based gas diffusion layer constitutes the electrodes, i.e., cathode and anode [56].	➤ Phosphoric acid, an inorganic acid in an utterly dissociated ionic state, is a good ionic conductor. Its high ionic conductivity makes it an ideal choice as an electrolyte in PAFCs. In the earlier developmental stages of PAFCs, diluted electrolytes were used to avoid corrosion. However, a concentrated electrolyte minimizes the water vapor pressure, thereby managing the water better and easier than PEMFCs [57].	❖ The negatively charged electrons are stripped from the hydrogen fuel through the external electrode circuit. The remaining positive ions travel through the electrolyte to the other porous electrode (the cathode), where they combine with oxygen ions that form when the free electrons combine with oxygen fed in at the cathode. The by-product of the reaction is electricity produced from the flow of electrons from the anode to the cathode. Cells are then “stacked” in series with their respective electrodes to create a prescribed direct current (DC) voltage level [76], which produces power about >50 KW [57].
Molten Carbonate Fuel Cells (MCFCs)	✓ The nickel anode is considered to have a much thinner electrolyte film because it is less wetted by the carbonate electrolyte compared with the nickel oxide (NiO) cathode. The anode material type is essential in the wetting properties and the active surface area. It has been reported that using Ni–Cr provides a more wetted area compared with other materials because of the formation of a large fraction of tiny pores (<0.4 mm) through the formation of lithium chromium dioxide (LiCrO ₂) (oxidation and lithiation of the chromium additive) [60].	➤ Molten carbonate salt is commonly used in MCFCs. It is compatible with CO ₂ as an electrolyte and provides excellent ionic conductivity at a relatively low temperature. The operating temperature of the MCFCs is reduced by changing the carbonate composition while maintaining cell performance, which is another positive factor when using molten carbonate as an electrolyte. The Li–Na carbonate has often been used as an electrolyte in MCFC to substitute the Li–K carbonate. Nevertheless, there may be a risk of a rapid decrease in cell voltage with Li–Na carbonate at atmospheric pressure and low temperature (≤600 °C) because of the relatively low solubility of oxygen in this eutectic [61].	❖ Introducing carbonate in the MCFC system is conducive to improving cell performance of open-circuit voltage and output power. The carbonate accelerates ion transfer as a medium or is a catalyst for carbon oxidation and gasification reaction with a producing power >1 MW [61]. The overall reaction is exo-energetic. This energy is an electric part consumed in the external electric circuit when the electrochemical reaction is reversible. One part of an energy TAS cannot be converted to electric energy and must be released as heat [77].

3. Basics and Materials

To confirm that the hydrogen oxidation reaction (HOR) and the oxygen reduction process (ORR) run efficiently, the fuel cell components must be chosen to maintain initial durability and lifetime effectiveness. Several issues need to be handled for activation enhancement and decreasing the transport losses, including, containing a durable electrocatalyst and lowering its loading, water management, contamination of the reactant/membrane, and removal. Consequently, material advancements and enhancements for fuel cells are essential and characteristics that provide a substance with its features and the fuel cell performance through various operating conditions are highly desirable [78].

3.1. Membrane

Membrane refers to a thin layer of electrolyte typically 10–100 μm that conducts protons from the anode to the cathode. The required membrane materials show high ionic conductivities, inhibiting the transference of electrons and the cross-over of oxygen reactants from the cathode and hydrogen fuel from the anode. Additionally, they must be chemically stable in environs with HO^- and HOO radicals, thermally stable through the operating temperatures, and mechanically robust. The present membranes are mainly based on perfluorosulfonic acid, the most protuberant Nafion, first developed by the Company of DuPont in the 1960s. Nafion[®] has a backbone structure of polytetrafluoroethylene (PTFE, recognized by the trade name Teflon), which delivers the membrane with physical strength. The sulfonic acid functional groups in Nafion deliver charge sites for the transference of proton. In addition, other perfluorinated polymer materials, for example, Neosepta-FTM (Tokuyama), FlemionTM (Asahi Glass Company), Gore-SelectTM (W.L. Gore and Associates, Inc.), and AsiplexTM (Asahi Chemical Industry) are also accepted for PEM fuel cell applications. Furthermore, materials of the membrane that can operate at high temperatures (100–200 $^{\circ}\text{C}$) are favored for high-temperature PEM fuel cells, which have the benefits of better catalyst tolerances to CO and stratagems of cooling for fuel cells [79,80].

Perfluorosulfonic acid (PFSA) is commonly used in PEM fuel cells as a PEM component. The main chain is highly hydrophobic and has Teflon-like characteristics. On the side chain, sulfonic acid is an extremely hydrophilic end group, enabling proton conduction by allowing water to adsorb. Membrane hydration is essential and should be regulated to the highest value possible to ensure enough water is available for proton passage without flooding the gas diffusion layers (GDLs) and catalyst layers (CLs). The side chain length is a necessary parameter in defining the stability and performance of the membrane. For implementations of proton exchange membrane fuel cells, two kinds of PFSA membranes are used and categorized, respectively, as long side chain (LSC), for example, Nafion[®], and short side chain (SSC), e.g., Aquiviun[®], membranes. The quantity of CF_2 units and the side chain structure are the most significant variances, as shown in Figure 9a [81]. Figure 9b demonstrates the morphology of a Nafion XL membrane (LSC) [75].

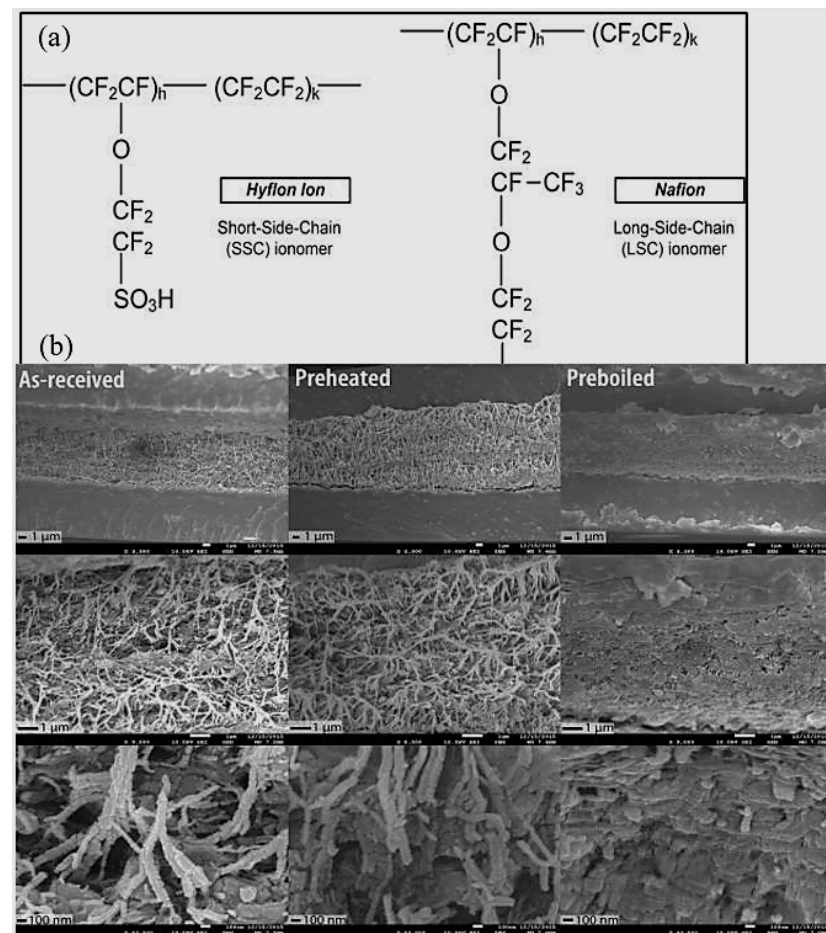


Figure 9. (a) Nafion and Hyflon Ion/Dow polymer structures [81], (b) shows the SEM image of Nafion XL membranes in their as-received shape after being handled using water. Small ($\times 3000$), moderate ($\times 9000$), and large ($\times 43,000$) magnification are presented throughout rows from topmost to bottommost [82].

Two main modes of transference occur in membranes: transport of water and proton. Gierke and Hsu defined the polymeric membrane, a cluster model, in terms of a reversed micellar structure in which the ion-exchange places are detached from the fluorocarbon backbone, joining the spherical clusters (pores) via short-cramped channels [83]. The cluster sizes rely on the content of local water. The gradient of the electrical potential of the electrolyte considers the major driving force for the transference of protons. The transference of protons crosses the membrane primarily because of the gradient of electrolyte potential and the relatively tiny diffusion influence. Water in the membrane is necessary for the transference of protons (diffusion of vehicular mechanism). By forming hydronium ions (H_3O^+), protons can transfer from high to low concentration regions, named the diffusion of vehicular [84]. So, this mechanism mainly relies on the diffusivity of water in the membranes. One more is through the “Hopping” mechanism that happens when the acceptable water content exists to attach the side chains of sulfonic groups, where protons can transfer straight from one site to another [85,86]. One of the furthestmost generally utilized proton-conductivity models is the experimental correlation advanced by Springer et al. [87] for the Nafion[®] 117 membranes:

$$K = (0.005193\lambda - 0.00326) \exp \left[1268 \left(\frac{1}{303} - \frac{1}{273 + T_{\text{cell}}} \right) \right] \quad (10)$$

λ : Water content

Additionally, according to one concept, the polymer backbone ($-\text{CF}_2-$) could react with hydrogen via $-\text{CF}_2- + 2\text{H}_2 \rightarrow -\text{CH}_2- + 2\text{HF}$, producing membrane degradation [88]. Therefore, for many years, the emphasis of polymer research in proton exchange membrane fuel cells was on developing cost-competitive membrane materials and providing superior endurance and stability along with a wide range of operating conditions, especially under extreme conditions of high temperature (e.g., $>120\text{ }^\circ\text{C}$) and sub-zero temperatures and low humidity (e.g., 0% RH); they have gained considerable attention in the scientific literature [89,90].

Low-cost solid polymer electrolyte compounds are available in various forms while eliminating the necessity of humidification. Nevertheless, for the period of the FC's working life, their stability and conductivity deteriorate. The main alternative membrane compositions are summarized in Table 2. Machine learning has the potential to significantly contribute to membrane material enhancement. Membranes with high conductivity of ions at a competitive price, durability, and slight hydration necessity are extremely required for proton exchange membrane fuel cells. Furthermore, other fields have extensively explored polymer membranes that conduct protons, such as Chlor-alkali production, metal-ion recovery, electrolysis of water, humidification/drying of gas, and flow battery. Machine learning aids analyze the massive amount of material data sets throughout literary works, for example, the structure of material, ionic conductivity, hybrid configuration, function groups, and performance of subfreezing, for the selection and optimization of material. In the operation of the fuel cell, the species cross-over, permeation/diffusion of water, transport of ions, and degradation of material all happen within the cell membrane, which can also be incorporated into machine learning along with its underlying mechanisms, control system enhancement, and diagnostics in real-time [78].

Table 2. Summary of alternative membrane materials to PFSA [78].

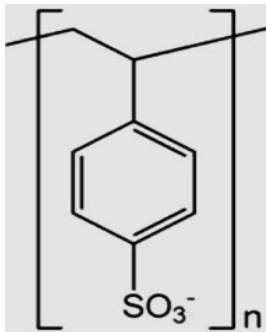
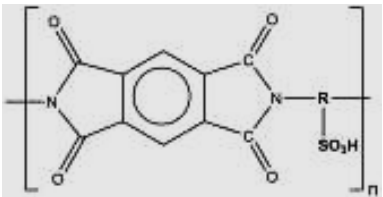
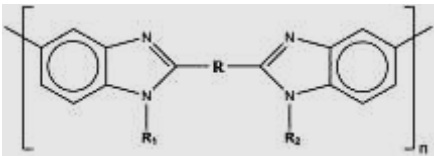
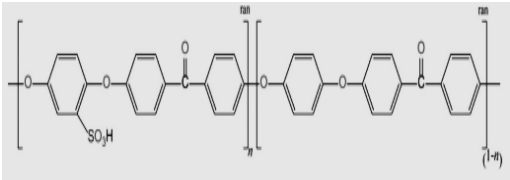
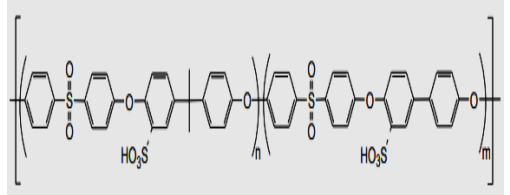
Material	Preparation	Comments
Polystyrene-sulfonic acid (PSSA) 	To prepare PSSA-Nafion composite membranes, the recast Nafion membranes (H ⁺ form) and PSSA, Nafion101 were initially transformed to the K ⁺ form via soaking them in a solution of 0.5 M KOH at 80 °C for 60 min. The membrane of PSSA could be attached firmly with Nafion101 or a recast Nafion membrane utilizing hot-pressing at 160 °C for 2 min. Then, the composite membranes were transformed to the H ⁺ form prior to creating the membrane fuel cell [91].	They are relatively inexpensive compared to Nafion, with the main disadvantage of their instability. Specifically, styrene sulfonic acid morsels are missing at great rates, dropping the ion exchange capacity and conductivity. The weak points are developed due to the aromatic ring protons and ternary benzylic hydrogen in the polymer chain. Strengthening these chains is vital.
Sulfonated polyimide (SPI)-based membranes 	The materials were utilized to generate sulfonated polyimide (SPI)-based membranes: 1,4,5,8 Naphthalenetetracarboxylic dianhydride acid (NTDA), 4,40-Diaminostilbene-2,20-disulfonic acid (DSDSA), 4,40-Diaminodiphenyl ether (ODA), 4,40-Diaminodiphenylmethane (MDA), Triethylamine, 3-Methylphenol (m-cresol), and benzoic acid. DSDSA, ODA, NTDA, and MDA were dried up in a vacuum oven at 120 °C [92].	Their main advantages are their high mechanical and thermal properties and durability against harsh chemicals and heat because of their thermos ability. The sulfonation of polyimides has been used to increase proton conductivity. Their main drawback originates from their instability under hydrated states due to hydrolytic, oxidative, and swelling-stress stability.
Polybenzimidazole (PBI)-based membranes 	3,3'-diamino benzidine (3.1150 g) and isophthalic acid (4.0180 g) were mixed with Polyphthalamide (60 g) and put in a round-bottom flask delivered with a reflux condenser with an inlet for nitrogen. The mixture was raised in temperature to 190 °C for 20 h. The Polybenzimidazole PBI powder was collected and then dissolved in n-n DiMethyl Acetamide to prepare 10 wt% of the solution of PBI. The incompletely dissolved Polybenzimidazole powder in DiMethyl Acetamide was eliminated via simple centrifugation [93].	They are tailored for operation at 160–220 °C and thus are suitable for PAFCs. The main challenges are: (i) electrolyte leakage, (ii) the presence of a liquid electrolyte and hence possible GDL flooding, and (iii) unsuitability for portable and transport applications. R&D also uses them in a new class of membranes with an improved matrix for H ₃ PO ₄ .

Table 2. Cont.

Material	Preparation	Comments
<p data-bbox="136 352 658 405">Sulfonated aromatic main-chain polymers I: Poly (arylene ether)-based SPEs</p>  <p>The structure shows a repeating unit of a poly(arylene ether) sulfone. It consists of two 4,4'-diphenyl ether units linked by an ether oxygen atom. The central carbonyl group is part of a sulfone ring. One of the phenyl rings is substituted with a sulfonic acid group (-SO₃H). The unit is enclosed in brackets with a subscript (1-n).</p>	<p data-bbox="714 352 1406 523">1.259 g (5 mmol) of 4,4'- difluorodiphenyl sulfone, 2.290 g (5 mmol) of 3,3'-disulfonic acid salt-bis (4-chlorophenyl) sulfone, and 25 mL sulfolane (TMS) were added continually to the dry three-port flask delivered with a condenser, magnetic stirrer, and water separator. Once the SPES-50 was prepared, 2.020 g (10 mmol) of 4,4'-dihydroxydiphenyl ether was added [94].</p>	<p data-bbox="1435 352 2128 523">They comprise sulfonated aromatic main-chain polymers and are cost-competitive with high mechanical strength and chemical/thermal stability. The SPEAKs and SPEEKs are the most studied, where various combinations are possible [95]. The main disadvantage is durability due to the scission of their main chain. Structural improvement of their backbone is vital.</p>
<p data-bbox="136 603 658 735">Sulfonated aromatic main-chain polymers II: Polysulfone-, polysulfone-ether-, and polyphenylsulfone-based SPEs</p>  <p>The structure shows a repeating unit of a sulfonated polysulfone. It consists of two 4,4'-diphenyl ether units linked by a sulfone group (-SO₂-). One of the phenyl rings is substituted with a sulfonic acid group (-SO₃H). The unit is enclosed in brackets with a subscript m.</p>	<p data-bbox="714 647 1406 882">Dissolving about 1.0 g of polymer in 5 to 10 mL of N, N-dimethylacetamide (DMAc) and casting the polymer solution on a glass plate led to the production of transparent membranes of sulfonated polysulfone. Dry membranes with thicknesses ranging from 2 to 10 cm were gained via changing the quantity of solvent or the distance between the Gardner knife and the plate for the duration of the casting process. Lastly, the membranes remained in acid form with 1M of HCl for 15 h at 50–60 °C [96].</p>	<p data-bbox="1435 647 2128 818">They are sulfonated aromatic main-chain polymers with the main advantages of cost competitiveness and thermal/chemical stability. Their mechanical properties rely on chemical modulation processing due to their amorphous nature. The main drawback is durability, especially in the presence of oxides. Thus, durability and stability enhancement are vital.</p>

Modification of Membranes for Fuel Cell Applications

The construction strategies for Nafion membranes can be classified into two categories: (i) material engineering toward Nafion-based composite membranes and non-Nafion membranes and (ii) structural engineering oriented toward surface-patterned Nafion membranes SPNMs. The composite membrane is based on a material composition process for reshaping the membrane's material properties, fuel crossover reduction, and mechanical properties improvement [97].

Many studies investigate the role of membranes and focus on the synthesis, characterization, and modification of these membranes to achieve the best results for fuel cell applications. Salleh et al. [98] investigated the stability of SPEEK/Cloisite[®]/TAP nanocomposite membrane in the Fenton reagent test to duplicate the polymer electrolyte membrane degradation mechanism using the radical attack during direct methanol fuel cell operation. The SP/CL/TAP nanocomposite membrane has shown higher water uptake, proton conductivity, and methanol permeability changes than the Nafion[®] membrane. Figure 10 shows that the Nafion[®] 117 membrane has the lowest weight loss among the tested membranes, followed by the SP/CL/TAP nanocomposite membrane and the pristine SPEEK membrane [98].

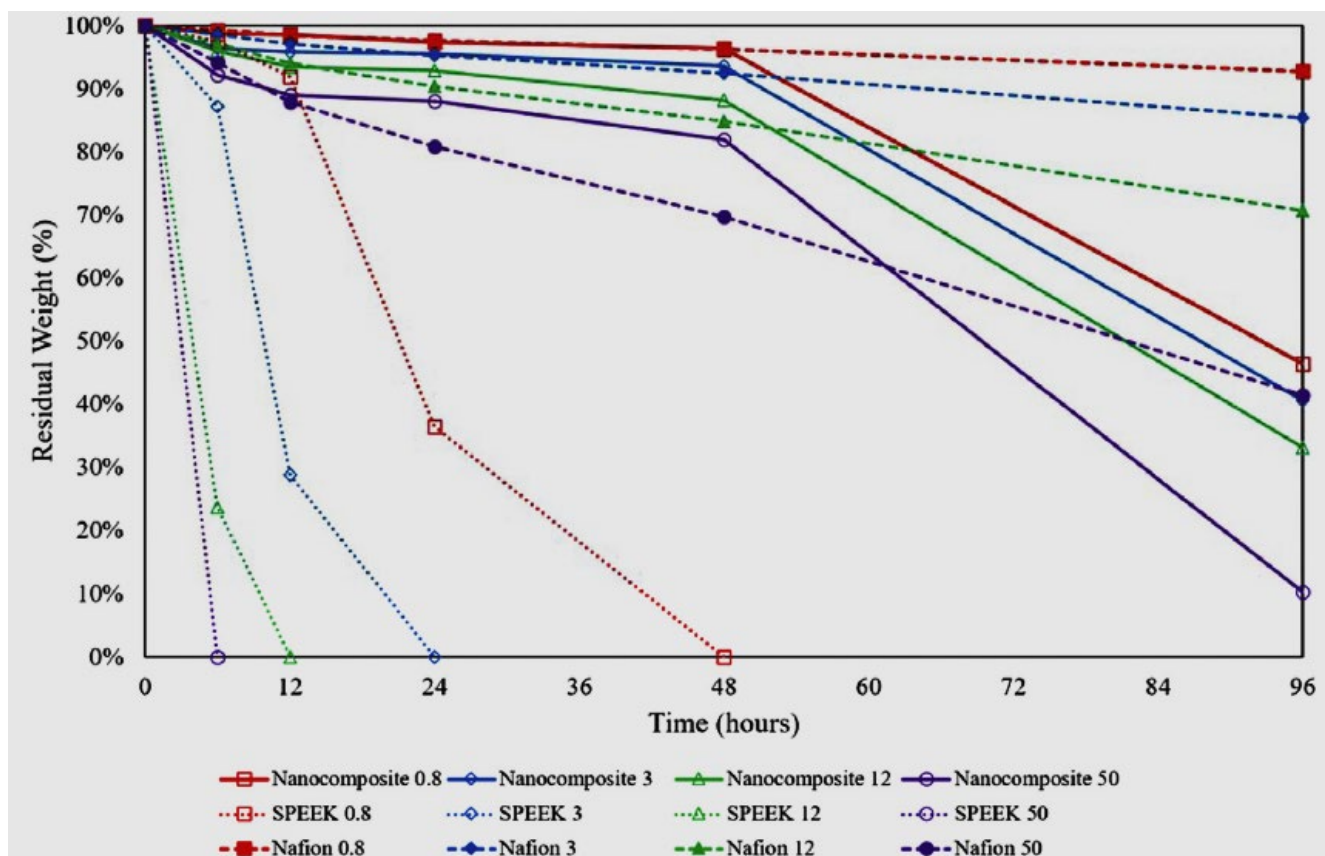


Figure 10. The residual weight of pristine SPEEK, SP/CL/TAP nanocomposite, and Nafion[®] 117 membranes after exposure to the Fenton reagent solution for 96 h [96].

In another study, novel hybrid composite membranes were fabricated by blending polyethylene glycol functionalized polyhedral oligomeric silsesquioxane [PPOSS] as a nanofiller. The concentration of the nanofiller was from 1 to 5% (*w/w*) into sulfonated polyether ether ketone [SPEEK], with the degree of sulfonation 55% for proton exchange membrane fuel cells [PEMFCs]. Figure 11 depicts the plot of the storage modulus versus

the temperature for neat SPEEK, composite, and Nafion 112 membranes. SPEEK, and its composite membranes, exhibits higher storage modulus values than Nafion 112 over the whole temperature range [99].

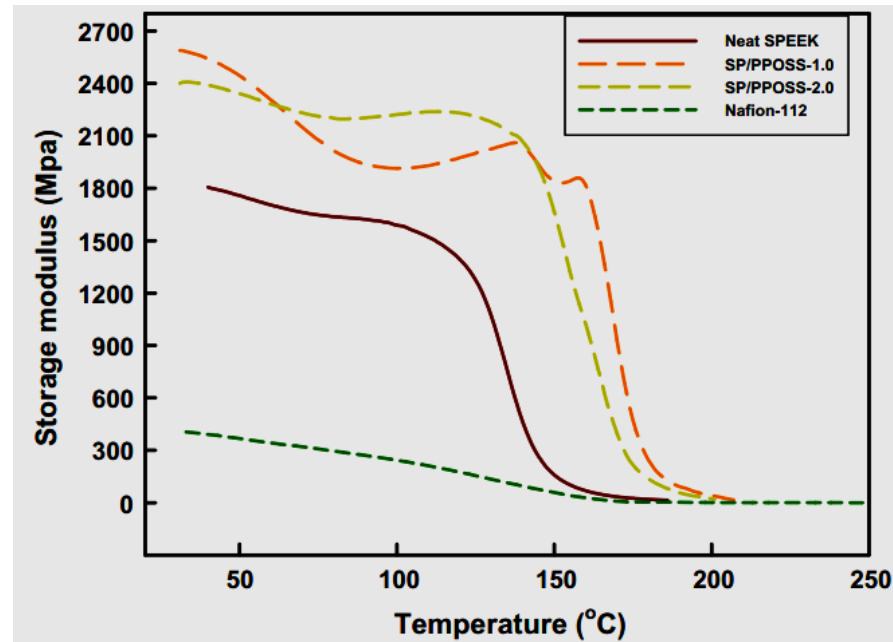


Figure 11. Plot of storage modulus vs. temperature for neat SPEEK, composite membranes, and Nafion 112 [97].

Ni et al. [100] fabricated two sulfonated fluorenyl-containing polyether ether ketone ketones (SFPEEKs) to be the matrix of composite proton exchange membranes via directly sulfonating copolymer precursors comprising non-sulfonatable fluorinated segments and sulfonatable fluorenyl-containing segments. The proton conductivity of each membrane increased as the temperature increased, as shown in Figure 12a,b. They found that proton conductivity was a thermally activated process and that the proton conductivity of pure SFPEEK-30 membrane was $0.106 \text{ S}\cdot\text{cm}^{-1}$ at 90°C , compared to that of Nafion 117 [100].

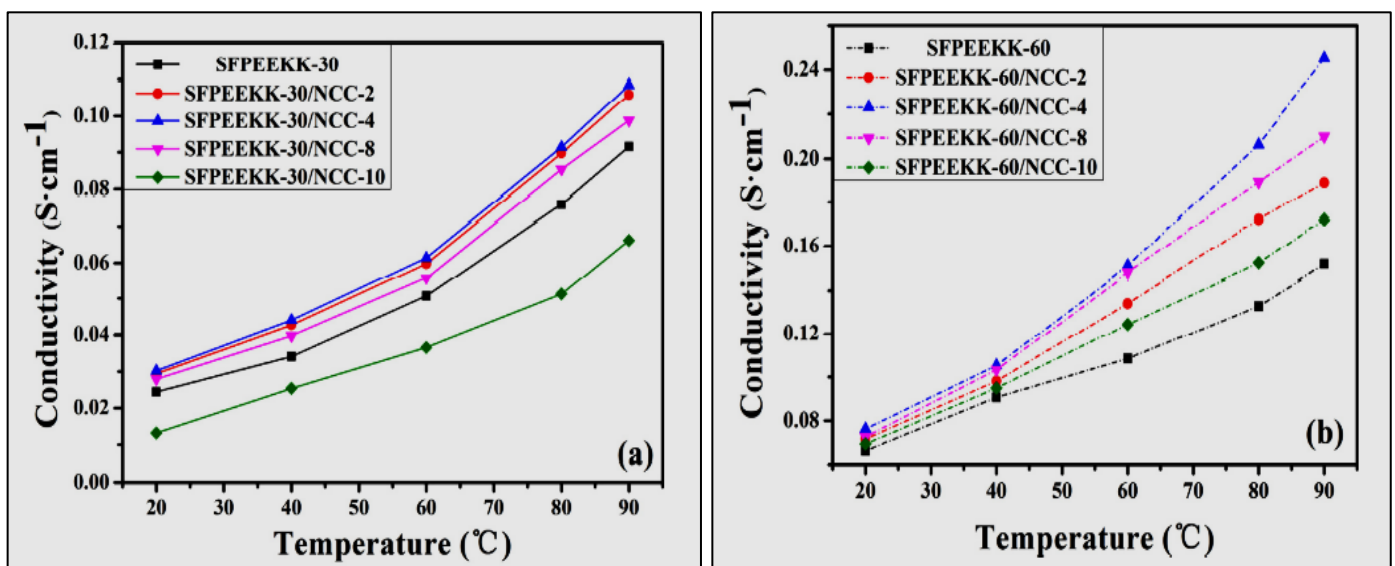


Figure 12. Proton conductivity of the membranes. (a) SFPEEKK-30/NCC series; (b) SFPEEKK-60/NCC series [100].

Quaternary-ammonium or quaternary-phosphonium functional groups are used as high-performance engineering polymers for anion exchange membrane fabrication. However, the membranes with such high functional group concentrations could suffer from significant swelling leading to efficiency reduction. Cross-linking between polymer chains is used to minimize the unwanted effects [101]. Among the various anion exchange functional groups that can hold hydroxide ions, quaternized trimethylamine has been used as a fluorinated film for the radiolytic preparation of anion exchange membranes through the radiation grafting of vinylbenzyl chloride (VBC) monomer and subsequent treatment with trimethylamine [102]. Due to low maintenance costs and favorable environmental properties, proton exchange membrane (PEM) technology has recently attracted more attention. The hydrogen storage concept is summarized in three main steps: production, storage, and consumption. These steps are performed in a PEM electrolyzer (PEME), pressurized hydrogen tank, and PEM fuel cell (PEMFC) [103]. Elumalai et al. [104] synthesized a series of novel composite anion exchange membranes for alkaline fuel cells. The membranes were prepared by casting the synthesized quaternary ammonium functionalized Polyhedral Oligomeric Silsesquioxane (QA-POSS) with Quaternary polysulfone (QPSU). The electrochemical tests in Figure 13 showed that the composite membranes possessed high OCVs of 0.835, 0.895, and 0.955 V for 5%, 10%, and 15% QA-POSS/QPSU, respectively, compared to the neat QPSU (0.66 V). They reported that the formation of denser composite membranes than the neat QPSU might reduce the fuel cross-over. Polarization plots showed that the maximum power density values were 154, 215, 248, and 321 mW/cm² of QPSU, 5% QA-POSS/QPSU, 10%QA-POSS/QPSU, and 15% QA-POSS/QPSU, respectively. Additionally, the current densities of QPSU, 5% QA-POSS/QPSU, 10%QA-POSS/QPSU, and 15% QA-POSS/QPSU were 425, 610, 680, and 720 mA/cm² (Figure 13). The higher hydroxide conductivity of the composite membranes is due to using different percentages of QA-POSS and some degree of water uptake, leading to higher fuel cell performance [104].

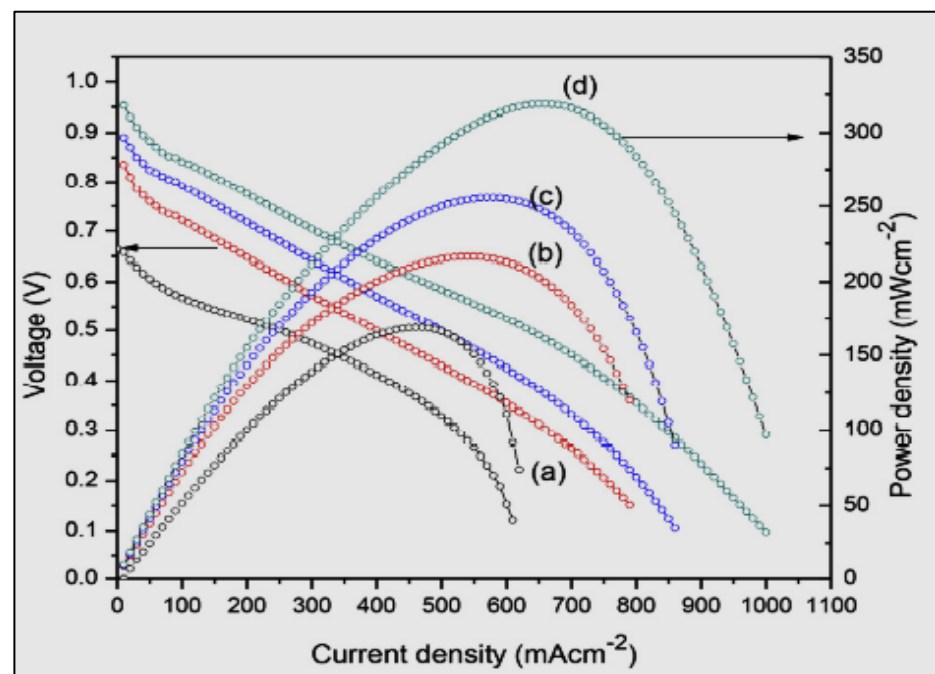


Figure 13. Polarization curves of QPSU (a), 5% QA-POSS/QPSU (b), 10%QA-POSS/QPSU (c), and 15% QA-POSS/QPSU (d) [104].

Modifying functionalized polymers using hydrophilic polymers to enhance the organic-organic phase interaction and thermal properties were reported for thermal-specific applications. However, different inorganic materials, such as silica, clays, metal oxides, carbon nanotubes, and a few others, are used to improve the properties of proton exchange mem-

branes [105]. Incorporating inorganic materials into proton exchange membranes results in the formation of nanocomposite membranes, where the nanostructures improve the thermal and mechanical stability of such membranes [106]. Feife et al. [107] synthesized a mixed matrix membrane comprising sulfonated graphene nanoplates (sGNP) and Nafion ionomers with aligned proton channels vertical to the membrane surface with an alternating electric field. They found that embedding sGNP enhanced the membrane's trans-plane conductivity. The trans-plane conductivity of the mixed matrix membrane can reach 0.155 S cm^{-1} at $80 \text{ }^\circ\text{C}$ and 100% RH (a 48% increase compared with the conventional cast Nafion membrane). In terms of H_2/O_2 fuel cells' power outputs, all mixed matrix membranes are superior to the traditional cast Nafion membrane (Figure 14).

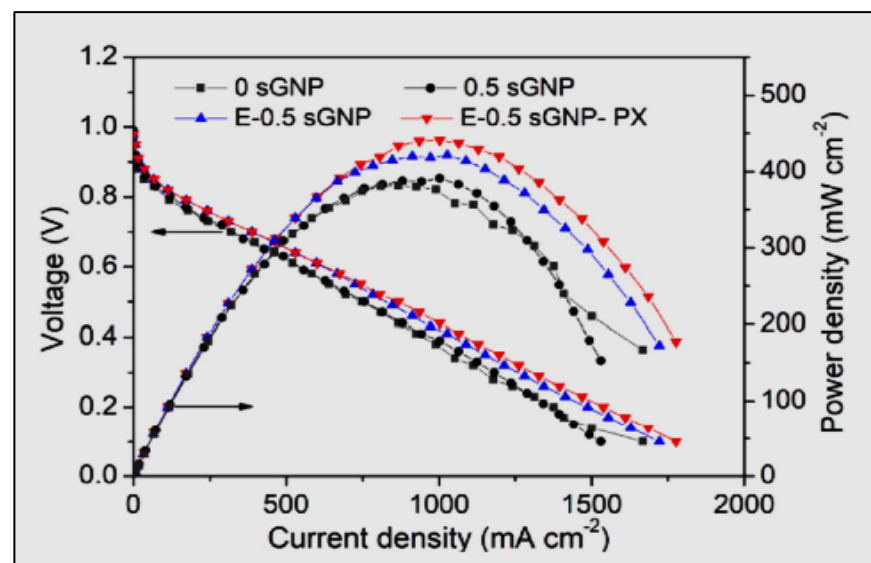


Figure 14. Performances of single fuel cell with pure Nafion or sGNP-Nafion mixed matrix membranes. The feeding flow rate of the humidified H_2 and O_2 gas were 75 mL min^{-1} and 150 mL min^{-1} , respectively. The operating temperature and backpressure were $80 \text{ }^\circ\text{C}$ and 0.1 MPa [107].

3.2. Catalyst Layers

The catalyst layer (CL) is a very thin active site (about $10 \text{ }\mu\text{m}$) where the oxygen reduction reaction (ORR) or hydrogen oxidation reaction (HOR) happens. Several phases included in a catalyst layer are essential to the electrochemical reaction: (1) carbon enhancement with particles of Pt catalyst spread on the carbon surface, (2) ionomer, and (3) space of void. The catalyst plays a serious role in dropping the reaction activation barrier. The oxygen reduction reaction occurs in the cathode, whereas hydrogen fuel is oxidized in the anode. An alloy of platinum or platinum element is a prevalent catalyst for oxygen reduction and hydrogen oxidation reactions. Consequently, the catalysts layer contributes an integral part of the cost of a fuel cell. Platinum and its alloys (Pt-Co, Pt-Ni, Pt-Fe, Pt-V, Pt-Mn, and Pt-Cr) show good catalyst kinetics. The lattice parameter of Pt in PtCo/C catalyst was 0.3820 nm , which is lesser than the Pt/C catalyst of 0.3920 nm . The lessening in the lattice factor of the alloy of PtCo/C shows that adding cobalt to the Pt crystal dropped the spacing of the atoms of Pt-Pt, which is considered a mechanism for improving oxygen dropping activity [108–110]. The Pt loading is a significant parameter in the improvement of CL. The US Department of Energy target is 0.30 and 0.20 mg.cm^{-2} for 2010 and 2015, respectively, and lately the 3 M company attains 0.150 mg.cm^{-2} with PtCoMn alloy [111]. The ionomer functions as a conductor of proton and a linker for the Pt/C particles. The difference in the loading of ionomers increases the transference or ohmic loss; including a minimal number of ionomers reduces proton conductivity, while a great quantity boosts the resistance of gaseous reactants to the transference. On the other hand, non-conventional catalyst layers are structured such that one of the main parts

in their traditional counterparts is removed. The kind and content of the binder define the permeability of gas, durability, catalytic activity, wettability, and ionic conductivity of CL [95,112,113].

The nanostructured thin film (NSTF) catalysts layer from 3M is the most effective non-conventional catalyst layer. They involve whiskers, in which the catalyst is implanted without the ionomer specified for proton conduction to deliver a more advanced activity than traditional catalyst layers over time [114].

Pt is the ideal electrocatalyst option within the reaction of oxygen reduction in fuel cells based on PEM since it has a great activity. Pt loading at a high level is essential for reaching the objective duration when deprived of a significant loss of efficiency and when the catalyst of Pt is arranged in a method that does not entirely use the catalyst layer. Yun et al. employed a spherical agglomerate model to enhance the content of the ionomer and the loading of Pt in the cathode. They considered three formulations and concluded that a classified distribution of Pt might develop using Pt [115–117]. Other CLs that are either Pt alloys or Pt-free are being explored. Two prominent past studies on the subject are provided by [118,119]. A brief of the various catalysts, their present statuses, and their challenges are delivered in Figure 15 and Table 3.

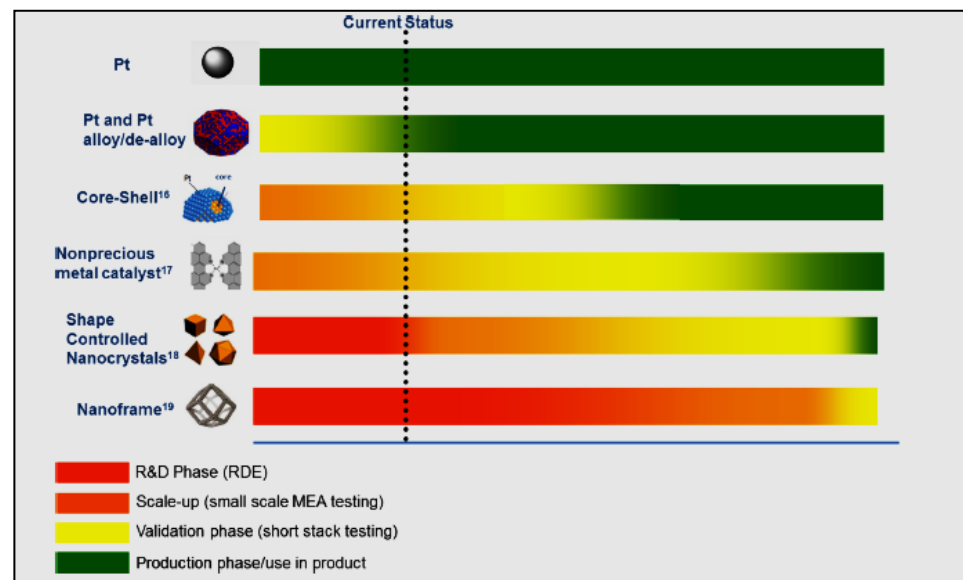
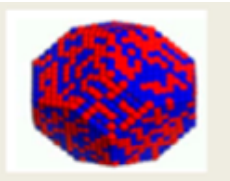
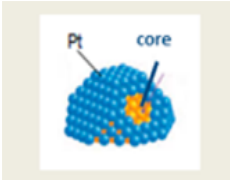
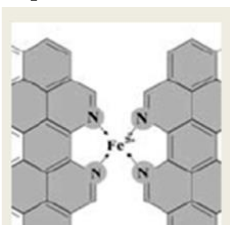


Figure 15. Improvement timelines for Pt, core-shell, Pt alloy/de-alloy, nonprecious metal, shape-controlled, and nano-frame oxygen reduction reaction electrocatalysts [118].

Though thin, the catalyst layer structure is complex and usually contains a number of unified networks for proton, electron, and reactant transference; projected mathematical techniques have been used to recreate the microstructure digitally [120].

Furthermore, the catalyst layer might be exposed to mass transference limitation or a significant ohmic loss. The basic cube size is $25 \times 10^{-2} \mu\text{m}$, signifying the size of the pore that is selected. So, 40 cubes are carried out in the thickness direction to simulate the $10.0 \mu\text{m}$ thick CL comparable to the method in the companion paper [121]. By the way, further dropping the catalyst layer thickness is essential to advance its presentation. A catalyst layer model that sufficiently captures the major transport phenomena and the hydrogen oxidation reaction or oxygen reduction reaction at the three-phase interface can be used to enhance the thickness of the catalyst layer. Such a model can clarify the influence of CL thinning on the performance of proton exchange membrane fuel cells [122,123].

Table 3. Illustrates the benefits and challenges of electrocatalysts [118].

Catalysts Type	Benefits	Remaining Challenges
Pt 	<ul style="list-style-type: none"> ❖ Mature technology. 	<ul style="list-style-type: none"> ❖ Failed to meet long-term automotive Pt loading and catalyst layer durability target.
Pt alloy/de-alloy 	<ul style="list-style-type: none"> ❖ Developed technology. ❖ Improved membrane/MEA durability. ❖ Better presentation over Pt/C. 	<ul style="list-style-type: none"> ❖ Unable to meet long-term automotive Pt loading target.
Core-shell 	<ul style="list-style-type: none"> ❖ Mass activity is improved over the Pt alloy. ❖ Durability enhancement over Pt/C. ❖ Highest reported ECSA. 	<ul style="list-style-type: none"> ❖ Difficult to maintain quality of the “shell”. ❖ Discussion of the “core” is still a concern.
Shaped controlled nanocrystal 	<ul style="list-style-type: none"> ❖ Significantly higher mass activity (~15 x) over Pt. ❖ Easy to scale up compared to core-shell. 	<ul style="list-style-type: none"> ❖ Scale-up can be performed at an early stage. ❖ Conflicting data on the stability. ❖ MEA performance has not been proven yet.
Nanoframe/nanocage 	<ul style="list-style-type: none"> ❖ Significantly higher mass activity (> 15 x) over Pt. ❖ Highly stable (improved durability over Pt/C). 	<ul style="list-style-type: none"> ❖ Scale-up can be performed at an early stage. ❖ Ionomer penetration into nanocage will likely be difficult. ❖ MEA performance at high current density may be difficult.
Nano-precious metal catalyst 	<ul style="list-style-type: none"> ❖ Potentially offer the most considerable benefit (significant cost reduction). ❖ Tolerance to common contaminants. 	<ul style="list-style-type: none"> ❖ Close to meeting targets for non-automotive applications such as backup power, but far from meeting automotive demands. ❖ PGM loading is not a significant concern for non-automotive applications at current volumes.

3.3. Gas Diffusion Layers

Gas diffusion layers (GDLs) and micro-porous layers (MPLs), together named diffusion media (DM), perform several roles: (1) transference of reactant and elimination of heat/water, (2) electronic connection amid the bipolar plate with channel-land structure and the electrode, (3) mechanical enhancement to the membrane electrode assemblage (MEA), and (4) safeguarding

of the CL from corrosion or erosion affected by flows or other causes. In the case of interdigitated projects, the diffusion media convective permeability should be great enough to allow the path of gas to be deprived of the extreme reduction in pressure [124–126]. The gas diffusion layer is a critical section of the anion exchange membrane fuel cell system as they have various functions and are the auxiliary substance for membrane electrode assemblage [127]. The gas diffusion layers are expected to have a great permeability of gas to transfer the reactant gases to the catalyst layer. They must be enhanced to balance the hydrophobicity to eject water out of the cell- and hydrophilicity to recollect the water and save the adequately hydrated membrane [128]. They must also have outstanding electronic conductivity to drive the electrons from the catalyst layer to the circuit and great thermal and chemical stability below vital conditions [129,130]. Woven carbon fibers or cloths are usually recognized as substrates of the gas diffusion layer through which gases are transported to the catalyst layer; these are preserved using polytetrafluoroethylene to be hydrophobized and avoid liquid water accumulation [129]. As the gas diffusion layer is in direct interaction with catalyst layers where the water is formed and expanded, its suitable engineering is active to manage water. Numerous plans have been created to fabricate an ideal gas diffusion layer to efficiently achieve the liquid water in the cell, including changing the hydrophobicity, containing a varying microstructure, adding hydrophobic and/or hydrophilic additives, and including/excluding hydrophobic microporous layers [131]. Carbon sheets are a combination of carbon fibers with fibers that are 7.0 μm in diameter. A binder holds the fibers collected, accounting for 5–15% of the last paperweight [124]. The carbon paper gas diffusion layer should be hydrophobic to develop the removal of water and prevent the flooding of the electrode. Polytetrafluoroethylene PTFE trademark (Teflon) is frequently added to carbon paper hydrophobicity enhancement. Additionally, the formation of carbon paper gas diffusion layers is anisotropic, as demonstrated in Figure 16.

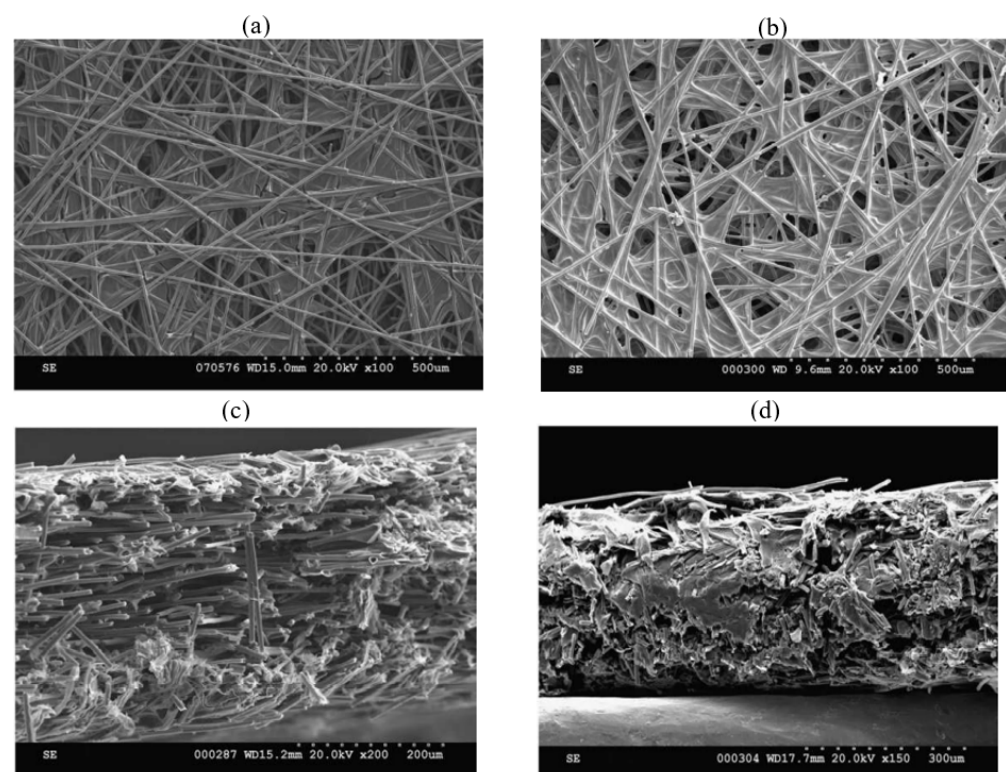


Figure 16. SEM images of (a) TORAY-TPGH-120 with 0.0% Polytetrafluoroethylene and (b) TORAY TPGH-120 with 50.0% Polytetrafluoroethylene; (c) cross-section image of TORAY-TPGH-120 with 20.0% Polytetrafluoroethylene; and (d) cross-sectional image of TORAY-TPGH-120 with 50.0% Polytetrafluoroethylene—the in-plane path is definite as the plane vertical to the carbon fibers (a and b display the xy plane, c and d show the xz plane, and the in-plane path is vertical to the xz plane) [132].

Furthermore, gas diffusion layers might be applied to disintegration after long-term processes, for example, wettability variation because of the loss of polytetrafluoroethylene and breakage of fiber rising from freeze/thaw cycling. The features of the surface were assessed via Wood et al. [133], who introduced single fiber contact-angle and surface-energy data of a broad spectrum of gas diffusion layer kinds to define the influences of hydrophobic post-processing handlings. Wang et al. [134] further exhibited the cathode catalyst layer and gas diffusion layer mass-transport overpotentials and examined the variations in durability. They discovered a minor rise in the gas diffusion layer mass-transport overpotential for the duration of the first period of approximately 500 h, but a substantial rise during the second period of roughly 500 h. Though Mukherjee et al. [135] showed a mathematical analysis on the influence of the durability gas diffusion layer on fuel-cell performance, the modeling of degradation mechanisms is still lacking and remains a challenge and therefore needs more studies.

A microporous layer (MPL) is regularly presented amid the two layers to develop the physical interaction of the gas diffusion layer-catalyst layer. It typically has a pore size amid the gas diffusion layer and catalyst layer and has been stated to improve the performance of a fuel cell sometimes due to the enhanced management of water in the cathode [136]. It has pores that are mostly smaller than 0.50 μm with a 0.320 μm mean size [137], whereas those in the gas diffusion layer and catalyst layer are typically around (6–20) μm and less than 0.020 μm , respectively [138]. Firmly compacted carbon black particles are collected in a microporous layer, bound by polytetrafluoroethylene, causing the microporous layer to be hydrophobic. The microporous layer ink is typically coated onto the surface of the gas diffusion layer for the duration of fabrication. Their primary goal is to deliver a smooth catalyst and continuous interface amid a gas diffusion layer, thus decreasing the interfacial resistance. The advantages of having additional microporous layers include: (i) the modification of electrode flooding; (ii) reduced general ohmic loss mostly because of the rise of membrane hydration; and (iii) improvement of the membrane electrode assemblage mechanical and chemical stability [139,140]. Machine learning can be carried out to enhance the gas diffusion layers and microporous layer design, containing the sizes of the pore, permeability, polytetrafluoroethylene loading, and physical dimensions. The equations of heat transfer and electric current conductance, species transference, Darcy's law, and the two-phase flow model are essential to be determined in the neural networks for active physics-informed machine learning.

Briefly, in the actual electrochemical reaction process, the functional layers of GDL, CL, and PEM must coordinate and participate together. Improving the material structure of each functional layer could play a significant role in improving the PEMFC performance [141]. A GDL plays a critical role in evacuating the water generated inside the fuel cell during the redox process and distributing the reacting gases on the catalyst surface. Several studies have been carried out to evaluate the role played by the GDLs on the performance and durability of a fuel cell and how specific GDL characteristics, such as their thickness and pore size distribution, affect its performance [142]. Water vapor transport through the GDL on the microscale is dominated by two diffusion mechanisms—molecular diffusion and Knudsen diffusion [143]. Various correlations have been developed between microscale parameters such as GDL material morphology and larger scale parameters (viz, tortuosity, diffusivity, and velocity) via pore-scale modeling and pore network modeling [144]. Nam et al. [145] used scanning electron microscopy to observe vapor condensation, liquid water morphology, and breakthrough in porous GDLs. Their model found that the morphology of the liquid deteriorates the efficiency of the electrochemical reactions in the catalyst layer and increases the water saturation in GDL. As the water droplets start to accumulate and occupy the pore space in the GDL, it blocks critical passages and reduces the gas reactants supply to the catalyst, which decreases the cell efficiency and performance. Carbon paper and carbon cloth are the two materials commonly used as GDL in fuel cells. The surface of the GDL material is usually treated with hydrophobic additives to promote droplet removal and the walls of other surfaces may be hydrophilic to draw water away from the GDL surface.

El. Kharouf [146] investigated the effect of different GDL properties of a wide range of commercial DGL materials on the performance of membrane electrode assembly (MEA) as different GDLs were used as cathode diffusion layers. The results show a decrease in the performance of MEA with increasing GDL thickness. The main effect of the GDL thickness is evident in the mass transport region. The water transport ability of the MEA is significantly affected by the increase in the thickness of GDL due to the increase in the permeability. Navarro [147] suggested that the GDL is the main component at the heart of a fuel cell. Thus, an *ex situ* and *in situ* study was carried out to show the characteristics of the new GDL called eCo. They concluded that the new gas diffusion layer called the eCo Cell shows an optimum performance for the range of temperatures studied due to its high hydrophobicity, bimodal pore distribution, low thermal conductivity, and high electrical conductivity.

Intuitively, a thinner GDL could aid the electrode performance because it would reduce resistance to the transport of oxygen and electrons. However, simulation results indicate the average distance from the current collector edge to a catalyst site at the middle of the flow channel compared to a catalyst site directly underneath the current collector. In general, increasing the GDL thickness can flatten the current density profile across the channel and land area. However, the effect of the GDL thickness on the local reaction rate (current density) is complicated and depends on the competing effects of oxygen and electron transport. At low overpotential, electron transport plays a more critical role in determining the local reaction rate [148].

4. Effect of Operating Conditions on AEMFCs Performance

The operating conditions of anion exchange membrane fuel cells, for example, inlet relative humidity, current density, and backpressure, deliver exterior controls to reduce the influence of flooding on performance. For the cathode and anode, irregular relative humidity and pressure operations were projected to simplify the diffusion of water from the anode to the cathode [149]. Water vapor pressure at the cathode can be improved using unbalanced pressure operation, which lessens the ohmic loss and develops the performance of cell. In contrast, the backpressure and relative humidity in the anode need to be excellently regulated [150]. The boiling point of water increases once the backpressure increases, which is not conducive to remove water from the anode. Studies of fuel cells determine the significance of the asymmetric regulation of anode and cathode inlet gases for enhancing environs of transfer of mass and electrochemical reactions. Likewise, relative humidity proved that inadequate humidification of the cathode is valuable for cell performance [151]. Unsaturated humidification at the cathode can raise the water gradient amid the anode and cathode, which is conducive to speeding up the back diffusion of water to cathode from anode. Therefore, this alleviates the flooding of the anode and resolves the problem of drying the cathode. The anion exchange membrane fuel cell catalyst layer is a complex subassembly affected by various parameters. A comprehensive study of the effects of inlet gas relative humidity, ionomer content, anode backpressure, and the role of MPL was carried out [152]. It is found that better performance of the cell is achieved with improved ionomer content under gas relative humidity due to the enhancement of membrane hydration and enrichment of the ionic conductivity in the catalyst layer. The insignificant rise of anode backpressure simplifies the transference of water to the cathode from the anode and develops the management of water. Plentiful water increases the hydration of the ionomer and membrane, leading to advanced ionic conductivity and lower resistance. In contrast, excess water closes the porous structure of the catalyst layer, leading to high mass-transfer resistance and deprived electrochemical reactivity [153].

4.1. Effect of Cell Operating Temperature

Figure 17a displays the anion exchange membrane fuel cells performance run at different temperatures in the cells with the enhanced anode/cathode gases inlet dew points. The outcome presents that the enhanced performance of the cell can be regularly developed

by means of growing the temperature at which the cell operates. A similar pattern can be seen when the temperature in the cell is between 60 and 70 °C due to the factors of process temperature dependence of the anion exchange membrane fuel cell. The ion conductivity of the membrane and the electrode reaction kinetics can be enhanced once the AEMFC is operated at an extraordinary cell temperature [154,155]. Williams et al. [156] reported that the performance of the cell is powerfully influenced via the operational temperature, especially under dry operation. Likewise, Natarajan D. and T. Van Nguyen [157] concluded that a growth in the operating temperature of a cell should be complemented via a rise in the anode humidification level to preclude the damage to the performance.

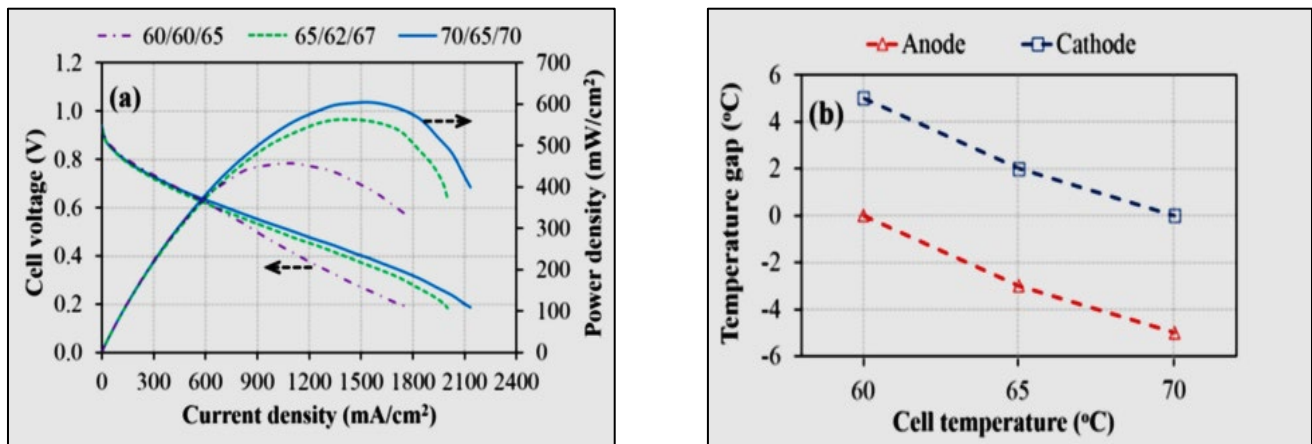


Figure 17. (a) Power density and polarization curves of anion exchange membrane fuel cells running at 60, 65, and 70 °C with enhanced dew points of the anode/cathode supply gases at 60 °C / 65 °C (60/60/65), 62 °C / 67 °C (65/62/67), and 65 °C / 70 °C (70/65/70), respectively; (b) The tap of temperature amid improved cell temperature and dew points (the symbol of 60/60/65 signifies that cell temperature and anode and cathode dew points are 60, 60, and 65 °C, respectively) [158].

The advanced temperature of cell operating could contribute to enhanced water transference in the gas diffusion substrate, driven via evaporation and shear force, resulting in a reduction in liquid water captured within the gas diffusion substrate and thus simplifying the permeability of reactant gases that have been humidified and efficient water elimination for the duration of cell operation [159]. Nevertheless, when the anion exchange membrane fuel cell is conducted at 75 °C, its progress begins to deteriorate after the entire experiment because of the incompetence of the membrane electrode assemblies in the anion exchange membrane. When comparing the effectiveness of three anion exchange membrane fuel cells at different temperatures, it can be detected that the gap in temperatures between the improved cell temperature and the dew point is enlarged at the anode and dropped at the cathode upon raising the temperature of the cell operating. These gaps of temperature at the anode/cathode are 0 °C/5 °C, 3 °C/2 °C, and 5 °C/0 °C, while the cells were maintained at a temperature of 60, 65, and 70 °C, respectively, as demonstrated in Figure 17b. This outcome shows that the necessity of inlet gas humidification at the anode and cathode to attain the required performance is reliant on the temperature of the cell, mostly since higher gas dew points carry more water content. Upon raising the dew point from 60 to 70 °C, the quantity of water vapor in the air will meaningfully rise from 150 to 234.8 g/m³. Furthermore, for the anion exchange membrane fuel cell operating below great current density, the rise in anode water production will partially permeate to the cathode and participate in the oxidation-reduction reaction. So, the difference in temperature among enhanced dew points at the anode and cathode as well as cell temperature varied depending on the temperature of the cell. This finding is appreciated by those who progress the anion exchange membrane regarding the design of the humidity control scheme [158].

The base-case anion exchange membrane fuel cell process was simulated for various operational temperatures of 45, 60, 90, and 120 °C to study the effect of operating temperature on the cell's stability and performance. Figure 18a shows the simulated preliminary polarization and power density curves. The outcomes present a vital improvement in cell performance once the temperature rises from 45 to 120 °C and are in accordance with available data in the literature reviews [160,161]; this includes the open circuit voltage values of 0.950–0.960 V and current densities at 0.80 V of 70–300 mA/cm² that were reported for the acidic high temperature-proton exchange membrane fuel cell operating at 100–120 °C [162]. A rise in the operative temperature from 45 to 120 °C develops the electrochemical reactions of the anode and cathode, leading to a three-fold increase in the current density in the activation (0.90 V) zone (Table 4). Additionally, the increase in temperature improves the OH⁻ conductivity and simplifies the transference of water over the membrane, dropping losses of ohmic and water transport. Consequently, greater power densities and a limiting current are attained. Table 4 presents the performance factors (current density at 0.90 and 0.60 V, peak power density, cell voltage at 0.60 A/cm²), which quantitatively exhibit a clear benefit to the high temperature operating of the anion exchange membrane fuel cell considered here. Figure 18b displays the expected variation in performance of an anion exchange membrane fuel cell with a constant current density of 0.60 A/cm² through time for temperatures ranging from 45 to 120 °C. Remarkably, whenever the temperature rises, the operational stability significantly improves, attaining an anion exchange membrane fuel cell entire life cycle of 6000 h at 0.670 V when the temperature is maintained at 120 °C [158,163].

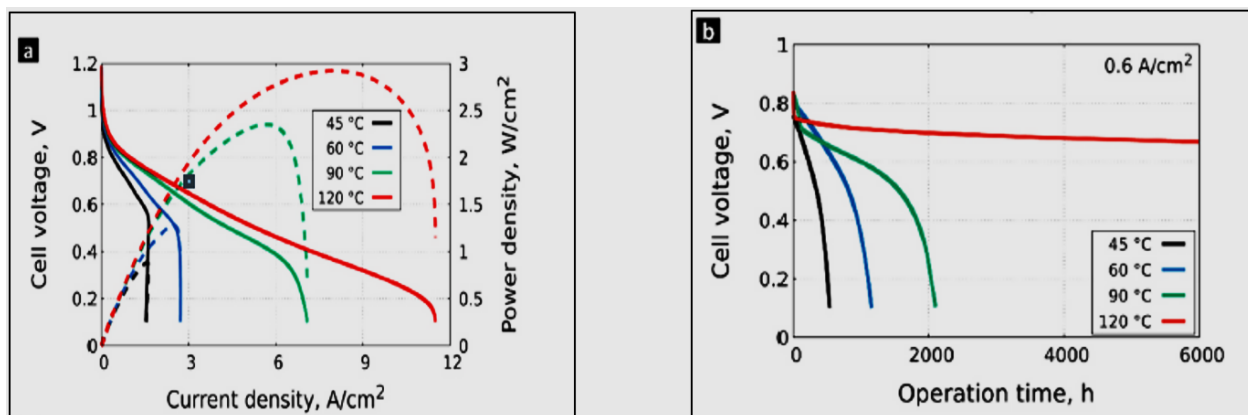


Figure 18. The simulated influence of operating temperature on the performance of a fuel cell with an anion exchange membrane and stability of performance; preliminary power density (dashed lines) and polarization (solid lines) curves (a) for various operating temperature values (45, 60, 90, and 120 °C). The voltage of the cell versus time of operation of an anion exchange membrane fuel cell operated below a constant current density of 0.60 A/cm² (b) for various operational temperature values [160].

Table 4. A quantitative comparison distinguished from simulated polarization curves and the influence of operational temperature (Figure 18a) [160].

Operational Temperature (°C)	Current Density at 0.90 V (A/cm ²)	Current Density at 0.70 V (A/cm ²)	Peak Power Density (W/cm ²)	Limiting Current Density (A/cm ²)	Cell Voltage at 0.60 A/cm ² (V)
45	0.093	1.42	0.89	1.54	0.759
60	0.159	1.89	1.29	2.71	0.798
90	0.225	3.06	2.36	7.04	0.828
120	0.282	3.89	2.94	11.46	0.842

The cause of this non-intuitive outcome is possibly a fine “competition” amid removal and diffusion, both associated with water content [164]. Whereas growing the temperature improves the rate of degradation of the ionomeric materials, it concurrently advances the diffusivity of water in the anion-exchange membrane, which simplifies the transport of water from the anode to the cathode. In the particular example that has been addressed in Figure 18b, though the temperature grew to 120 °C, the increase in the diffusivity of water is meaningfully more prevailing than the thermally induced rise of the rate of degradation of the ionomer [165,166].

Moreover, no additional products (because of thermal degradation) were detected at the advanced temperatures. The average energy barrier from these three temperatures concluding down to 80 °C outcomes in an expected half-life more significant than 4 years, with only 10 percent degradation happening after 5300 h, were used [167]. The rate of degradation of quaternary ammonium (QA) groups rises dramatically with the concentration of OH[−] and temperature, representing the position of adequate hydration of hydroxide exchange membranes in alkaline fuel cells for attaining long half-life times [168]. After ageing at extraordinary temperatures, the anion exchange membranes become insoluble, representing the cross-linking reaction [169].

4.2. Effect of Relative Humidity in Inlet Gases

A greater fuel inlet humidification temperature includes an advanced quantity of water, which can wet the membrane and drop transmission impedance, thus supporting the fuel cell performance. Growing the humidification temperature advances the hydrogen-oxygen reaction at the catalyst and overwhelms the performance removal affected by the inadequate concentration of gas, though the extreme inlet humidification temperature can produce internal water flooding [170,171]. The influence of moisture content on the fuel cell has been examined by reducing the relative humidity of the supply gases to 70% at either the cathode or anode. The logarithmic curve demonstrates this in Figure 19a, the variations in relative humidity do not upset the activity in the section with a low current density. Nevertheless, some performance damages are detected at advanced current densities, as seen in Figure 19b. As probable, the utmost substantial influence of reduced relative humidity in the input gas can be observed at the cathode when water is a reactant. Lower humidity at the anode declines performance, while once current densities are extremely high an insignificant performance rise is noted. The Nyquist graphs were compiled at a current density of 16 mA/cm², shown in Figure 19c, demonstrating that reduced humidity causes the high-frequency semicircle to expand independently; the electrode is included amid 100 Hz and 100 kHz, moving the right semicircle further to the right. The size of the semicircle at the low-frequency range is unaffected by relative humidity. The frugal influence of humidity on the high-frequency interrupt displays that the resistance of the membrane is not meaningfully improved at this current density [172].

The water supply necessity in anion exchange membrane fuel cells is utilized to endure the oxidation-reduction reaction in cathode electrodes and the hydration of anion exchange membranes. The water deficiency in anion exchange membrane fuel cells could directly affect the method of the membrane conductivity and electrochemical reaction producing a reduction in the performance of the cell. Consequently, the performance of cells is significantly dropped once the cathode inlet humidification is much less than the augmented level, as shown in Figure 20. It is found in Figure 20c that the procedure of the anion exchange membrane fuel cells utilizing the dew point of 70 °C (70/65/70) and 65 °C (70/65/65) at the cathode has an analogous performance at current densities lower than 10³ mA/cm². The performance of an anion exchange membrane fuel cell utilizing the dew point of 65 °C drops significantly at current densities greater than 10³ mA/cm² because of the excessive request for water in the oxygen reduction reaction below high-current conditions. Dissimilarly, the anion exchange membrane fuel cell that utilizes the dew point of 75 °C (70/65/75) has a lesser performance related to that utilizing the dew point of 70 °C (70/65/70) [158]. The use of an excessive humidification supply can

be attributed to the oxygen mass transportation constraint at the cathode side since the microporous channels inside the gas diffusion layer are being closed by condensed liquid water. Additionally, setting a greater cathode dew point will produce a greater quantity of water vapor and a slighter molecule number of O_2 in the gas stream at a similar rate of flow, causing less O_2 molecules to exist for the oxygen reduction reaction and thus lessening the performance of cell [173]. Comparable outcomes can be observed once the cell is operated at lesser temperatures (60/60/65)/(60/60/70) in Figure 20a and (65/62/67)/(65/62/72) in Figure 20b [158,174].

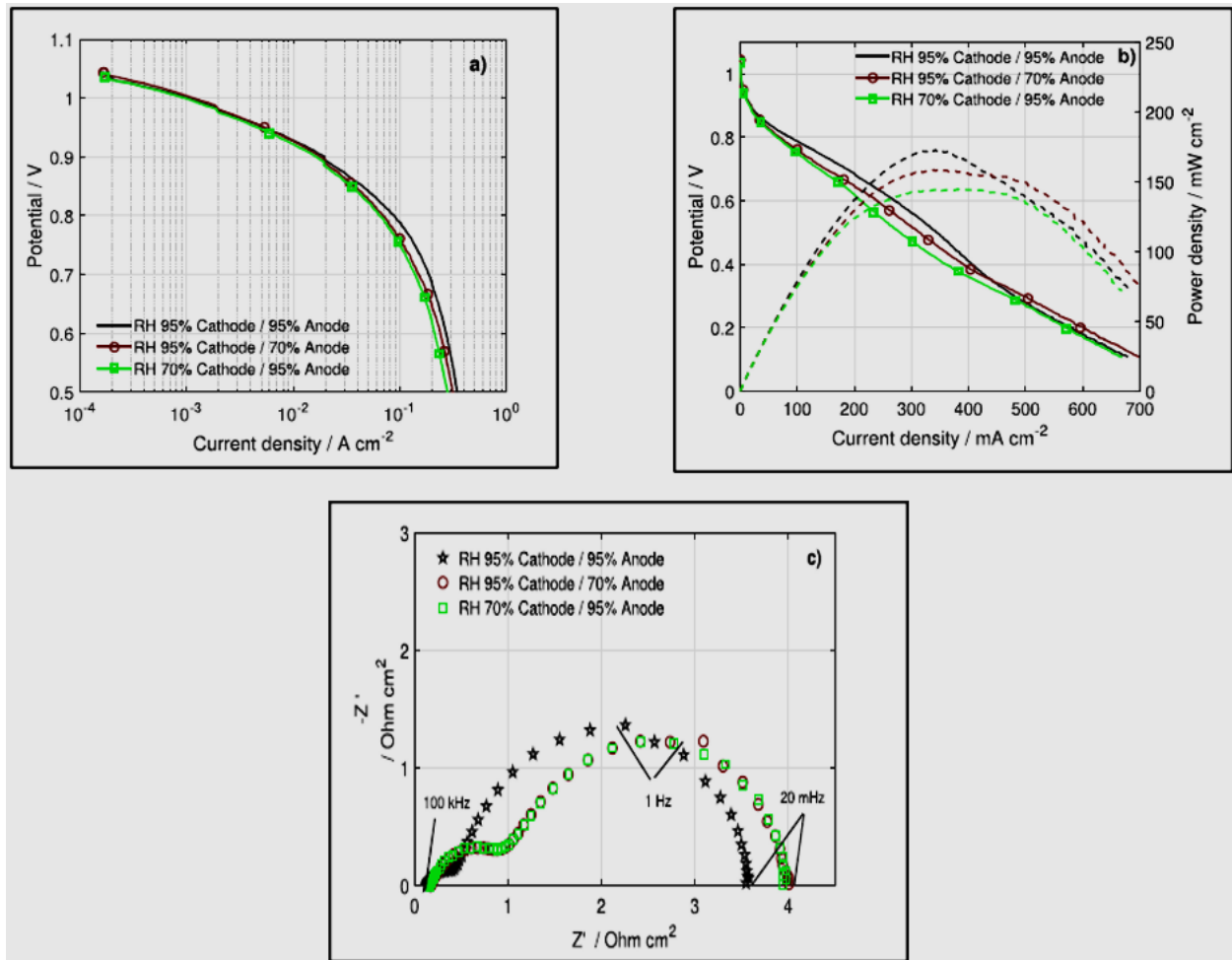


Figure 19. Influence of changing relative humidity on the anode and cathode, respectively, (a) Logarithmic graphs with IR correction, (b) Profiles of IR-corrected polarization and power density, and (c) EIS Nyquist plot from 100 kHz to 20 mHz at 16 mA/cm² [172].

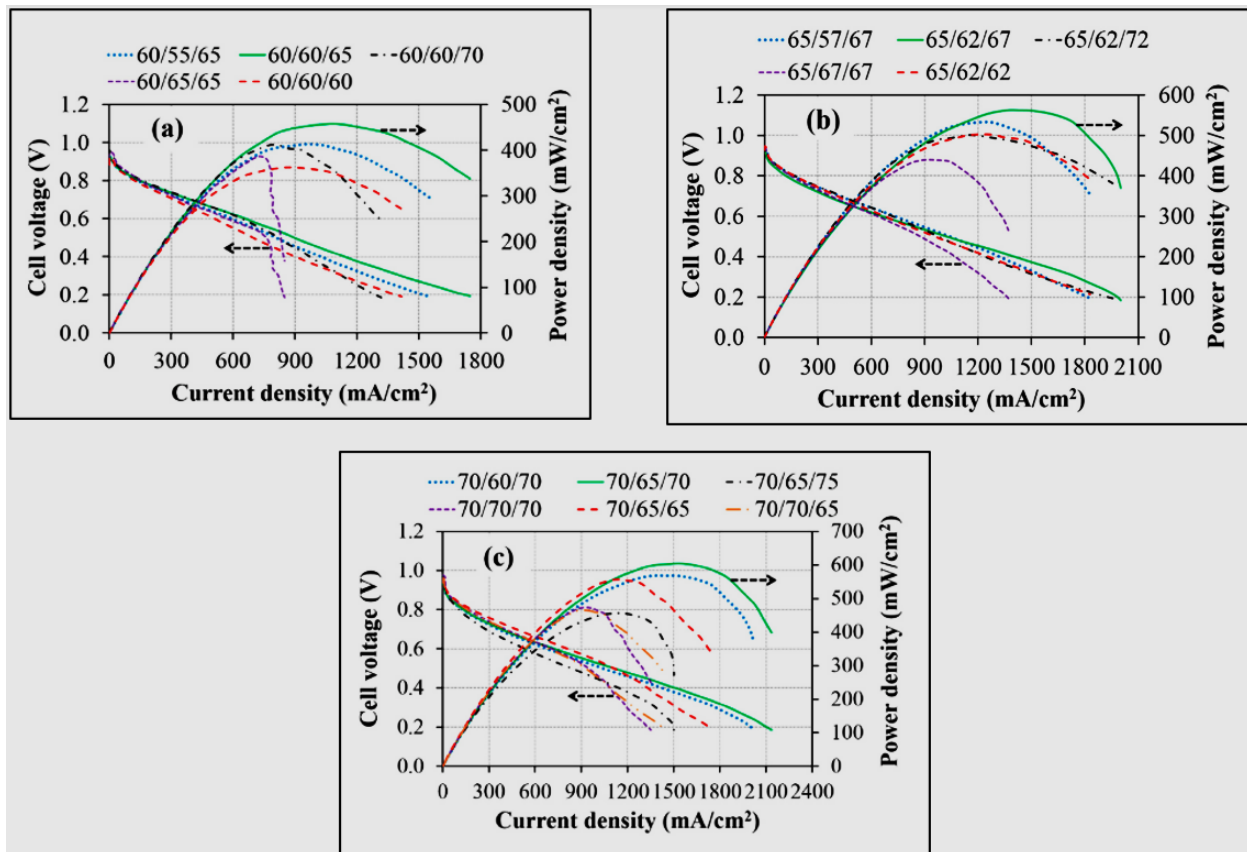


Figure 20. Polarization and power density curves of anion exchange membrane fuel cells operated at cell temperature of (a) 60 °C, (b) 65 °C, and (c) 70 °C with various dew points of the anode/cathode inlet gases (the mark of 60/55/65 means that the cell temperature and dew points of the anode and cathode are 60 °C, 55 °C, and 65 °C, respectively) [158].

4.3. Effect of Flow Direction

Figure 21 exhibits the average water areal density and performance for cell 1 operating under various flow configurations. In the counter-flow configuration, the hydrogen inlet is the opposite of the air inlet (Figure 21a). This makes a more significant gradient in water concentration through the membrane electrode assembly at the operational condition and more supports the recirculation of water amid the anode and cathode sides, i.e., interior humidification as defined by Büchi and Srinivasan [175]. The internal humidification outcomes improved hydrated membrane electrode assembly and improved performance (Figure 21b). Additionally, more water develops on the anode electrode, which is particularly apparent at a low velocity of 0.40 A/cm², resulting in a significant difference in water content between the two different arrangements, 5.50 mg/cm² in the event of a counter-flow arrangement and 1.70 mg·cm⁻² for the other. As current density rises, the variance reduces. The images of neutrons of each of the flow fields (Figure 21c) display that in addition to a higher proportion of water in the overall composition with the counter-flow procedure, as exposed by Kim et al. [176], there appear separate water distributions amid the two configurations.

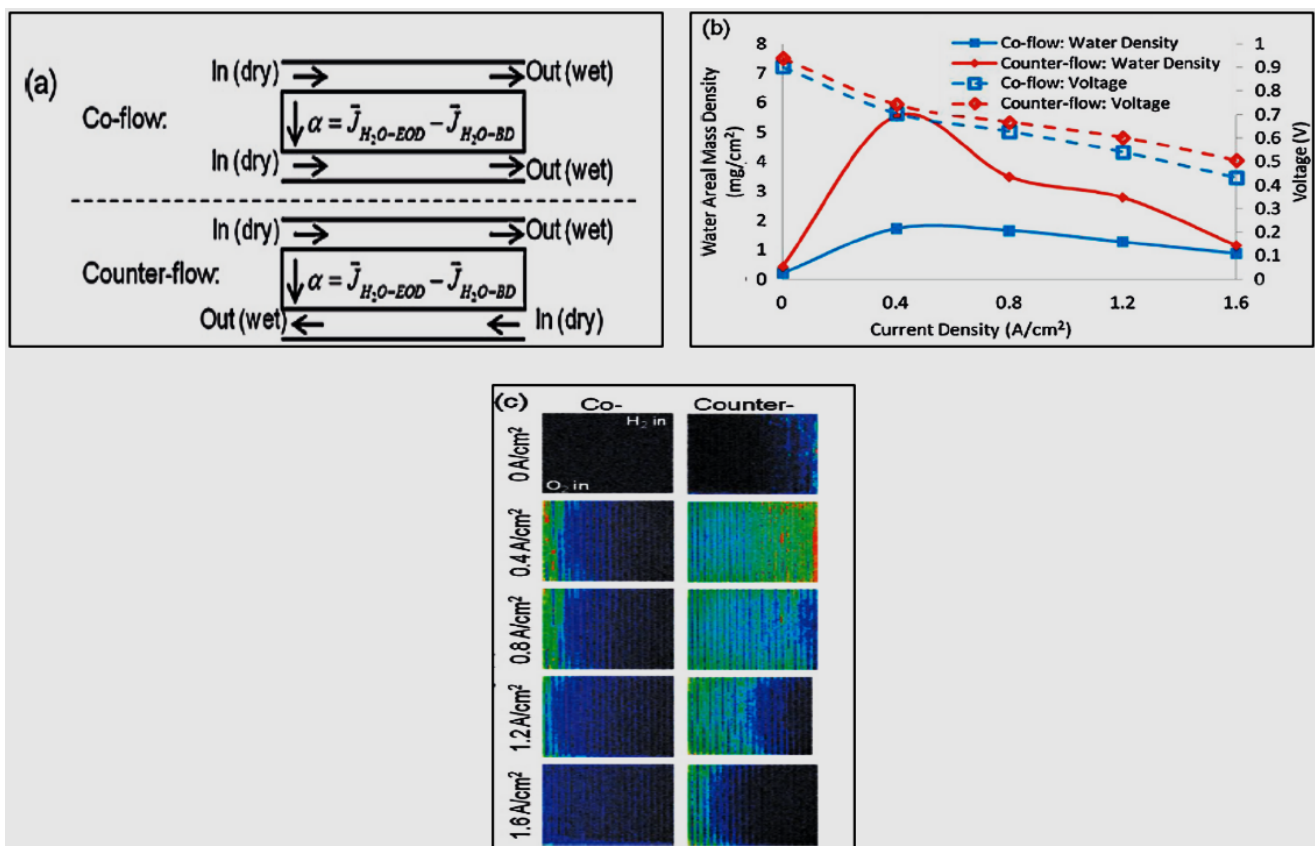


Figure 21. (a) Co-flow and counter-flow operations are illustrated in a flow diagram., (b) the density and effectiveness of water in cell 1 under varying operating arrangements at 50 percent inlet relative humidity, and (c) the corresponding-colored neutron images (c) [177].

The dynamic reply of the no humidification proton exchange membrane fuel cell was observed as the current density raised suddenly from (1 to 1.40) A/cm² at the operational temperature of 80 °C and 0 percent relative humidity. As exposed in Figure 22a, in both the counter- and co-flow cells, voltage undershoots were observed following the load change. After the change of load, the undershoot refers to the variance amid the smallest and enduring values. In the no humidified condition (0% RH), the voltage undershoot happened mainly due to membrane hydration time delay [178]. The voltage immensely reduced instantly after the increase in the current density, as the ionic resistance of the membrane was still reasonably high related to the raised current. Then, membrane ionic resistance regularly reduced with the rise in the water content of the membrane, as exposed in Figure 22b, owing to the improved self-humidification because of the augmented water generation. Following the undershoot, the voltage augmented suddenly and regularly approached the steady-state value. Though, in the co-flow cell, the voltage undershoots led to a short period of zero power density due to poor performance. As presented in Figure 23, for all load change conditions, the zero-power periods were detected in the co-flow cell. The counter-flow cell's zero-power period was not noted because of the greater voltage with the high-water content associated with the co-flow cell. In general, the zero-power period afterwards the load change in the co-flow cell can produce a deadly defect for the duration of the acceleration procedure once the cell is utilized as a power resource [179].

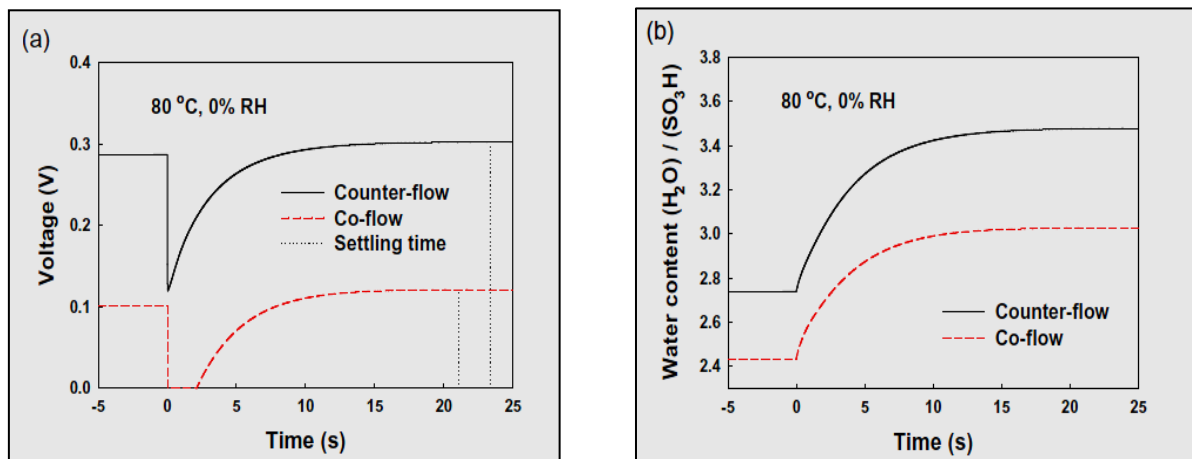


Figure 22. Dynamic responses of (a) cell voltage and (b) membrane water content for the duration of the stepwise rise in current density from (1.0 to 1.40) A/cm² [179].

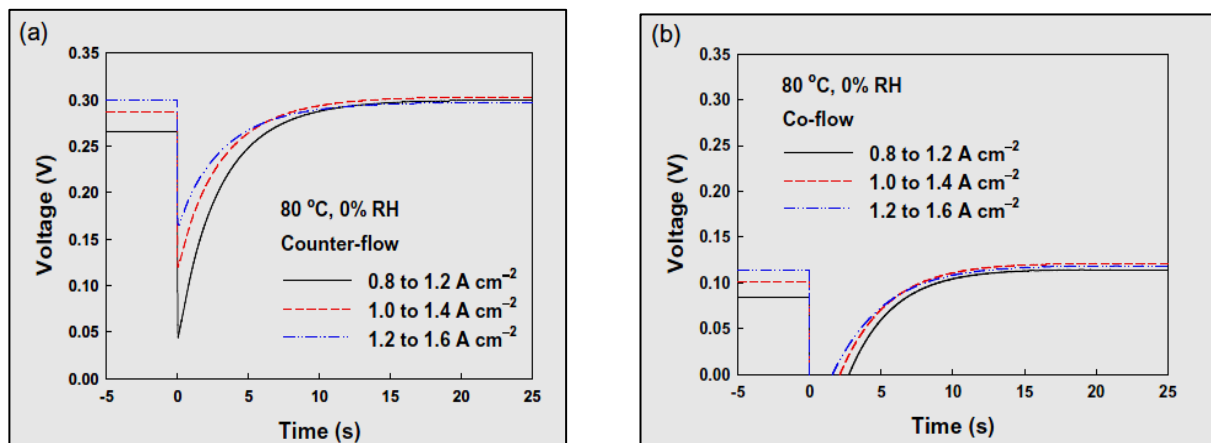


Figure 23. Dynamic responses of cell voltage in (a) counter-flow and (b) co-flow cells for the duration of the stepwise rises in current density from (0.80 to 1.20) A/cm², from (1 to 1.4) A/cm², and from (1.20 to 1.6) A/cm² [179].

4.4. Various Polytetrafluoro Ethylene Loadings in Gas Diffusion Layers (GDLs) and Layers of Microporous Structure

Figure 24 shows that cell 4 has a lower polytetrafluoro ethylene loading in the microporous anode layer and cell 2 has various polytetrafluoro ethylene loadings in the cathode gas diffusion layers (GDL) and microporous layer (MPL). Both water content and cell performance vary when changing the wettability of gas diffusion or microporous layers. To be specific, a development in cell performance is referred to when growing the polytetrafluoro ethylene loading within the microporous anode layer from 5.0 percent (triangles or cell 4) to 23.0 percent (squares or cell 1), as exposed in Figure 24 [177]. Moreover, higher water content is found in cell 4 at 0.40 A/cm², which can be expressed by its less hydrophobic anode microporous layer. Anode channel flooding may occur if there is more water in the anode, it can be very intense at 0.40 A/cm² because of the equivalent low gas flow rate. Related to cell 1, cell 2 has a more hydrophobic cathode microporous layer; more water is being forced from the cathode to the anode. With growing current density, flooding of the anode channel can be enhanced due to the increased gas flow rates and electro-osmotic drag and the water contents in both cells 2 and 4 are found to drop quickly. Furthermore, cell 2 has more hydrophobic microporous layers in both the anode and cathode. Thus, the water transference barrier across the microporous layers is higher, leading to a more hydrated membrane electrode assembly, as shown by the high-frequency resistance (HFR) exposed

in Table 5, and hence a reduced ohmic loss. This might be one leading cause for the greater performance of cell 2.

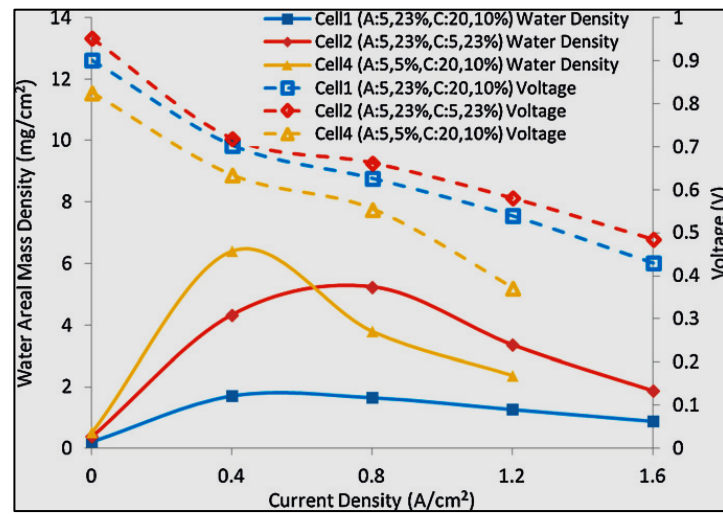


Figure 24. Water areal density and cell performance for various polytetrafluoro ethylene loadings in the gas diffusion layer substrate and microporous layer at 50.0 percent inlet relative humidity [177].

Table 5. High frequency resistance of the tested fuel cells [177].

Current ($A \cdot cm^{-2}$)	High-Frequency Resistance ($\Omega \cdot cm^2$)			
	Cell 1 (A: 5%, 23%; C: 20%, 10%)	Cell 2 (A: 5%, 23%; C: 5%, 23%)	Cell 3 (A: 5%, 23%; C: 20%, 10%)	Cell 4 (A: 5%, 5%; C: 20%, 10%)
50% inlet RH				
0.40	0.0620	0.0460	0.0550	0.0440
0.80	0.0570	0.0400	0.0510	0.0580
1.20	0.0570	0.0410	0.0590	0.0560
1.60	0.0640	0.0430	0.0800	–
100% inlet RH				
0.40	0.0420	–	0.0390	0.0410
0.80	0.0420	–	0.0380	0.0410
1.20	0.0420	0.0390	0.0390	–
1.60	0.0430	0.0390	0.0390	–
Cell 1 (A: 5%, 23%; C: 20%, 10%)				
	Co-flow, 50% inlet RH	Co-flow, 100% inlet RH	Counter-flow, 50% inlet RH	
0.40	0.0620	0.0420	0.0450	
0.80	0.0570	0.0420	0.0450	
1.20	0.0570	0.0420	0.0460	
1.60	0.0640	0.0430	0.0500	

The influence of the microporous layer is stable using the model analysis by Pasaogullari et al. [180] and Weber et al. [181], and the through-plane radiography by Mukundan et al. [182]. Moreover, at $1.2 A \cdot cm^{-2}$, cell 4 shows a quick reduction in cell performance, though its averaged water content is less than that of cell 2. This can probably be clarified utilizing similar facts as stated above: cell 4 is subject to anode flooding because of its less hy-

drophobic microporous anode layer. The liquid water in the anode hinders the hydrogen source, restraining the current density. As for cell 2, its microporous layers are more hydrophobic, resulting in an improved hydrated membrane in a larger field of the fuel cell.

Figure 25 displays the assessed through-plane permeability of the microporous layer-coated gas diffusion layers as a function of the polytetrafluoro ethylene loading for the differently considered carbon loadings, namely 0.50, 1.0, 1.50, 2.0, and 2.50 mg/cm² in the microporous layer. All the curves express three common trends for all the carbon loadings studied. One of these common trends is that after 20 percent polytetrafluoro ethylene loading the permeability rises with growing polytetrafluoro ethylene loading in the microporous layer. The literature has justified this by describing that the relatively large polytetrafluoro ethylene particles cannot enter the relatively small pores within the carbon agglomerate except in the larger pores amid these agglomerates. Growing the sizes of the agglomerates raises the porosity of the carbon-PTFE mixture [183]. This has been proven as definite by means of the pore size distribution (PSD) measurements, conducted by Uchida et al. [184], which present the increasing of the pore size in polytetrafluoro ethylene loading as the carbon-PTFE mixture rises. The second common trend is that the permeability of the gas diffusion layer drops once the polytetrafluoro ethylene loading in the microporous layer is improved from 10 to 20%. This can be clarified by stating that (i) the rise in the polytetrafluoro ethylene loading raises the thickness of the microporous layer and (ii) the polytetrafluoro ethylene loading is not adequately great to cause its “positive” porosity-increasing influence to overwhelm its “negative” thickness-growing influence. The latest common trend is that the gas permeability of the coated gas diffusion layer is at its minimum with 20.0 wt. percent polytetrafluoro ethylene loading in the microporous layer [184].

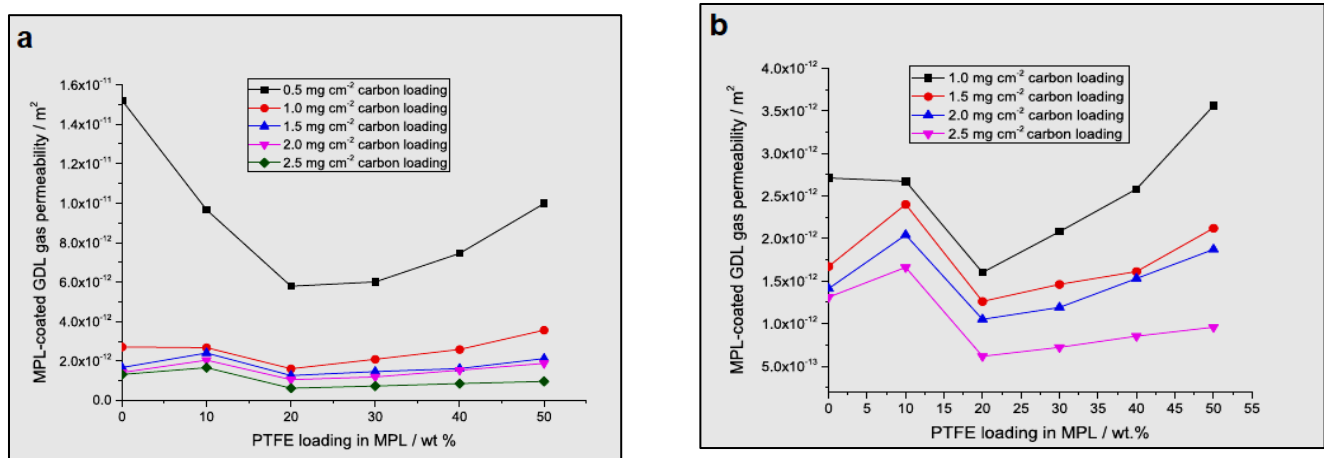


Figure 25. (a) The curves represent the gas permeability of the microporous layer-coated gas diffusion layers as a function of polytetrafluoro ethylene loading for different carbon black loading and (b) the above curves after exclude the 0.5 mg/cm² carbon loading curve [185].

For a dual-layer gas diffusion layer, a fluorinated polymer as a binder and hydrophobic agent has been utilized to simplify the liquid water transportation to the gas flow channel. On the other hand, numerous research groups used extra hydrophilic materials for hydrophobic MPL to wick water from the catalyst layer [186]. There is an optimal quantity of polytetrafluoro ethylene at which the through-plane permeability of the SGL samples is extreme, that is 5.0 percent by weight. One might assume that adding a small quantity of polytetrafluoro ethylene improves the through-plane permeability of the carbon substrates [187]. The permeability of the microporous layer coated gas diffusion layers was measured and found to be in the order of 10⁻¹³ m⁻², thus suggesting that adding the low-in-porosity microporous layer to the carbon substrates meaningfully drops the through-plane permeability of the latter substrates by 1–2 orders of magnitude [188].

Interestingly, the polytetrafluoro ethylene loading is sensitive to the carbon loading in the polytetrafluoro ethylene loading range from 0 to 10 percent. That is the permeability in this range: (1) drops for the 0.5 mg/cm² carbon loading, (2) stays almost the same for 1.0 mg/cm² carbon loading, and (3) rises for the 1.50, 2.0, and 2.50 mg/cm² carbon loadings. The 0.50 mg/cm² carbon loading is not adequately great to wholly cover the large pores on the carbon substrate surface. Figure 26a displays that, with 0.50 mg/cm², the skeleton of the carbon substrate can be seen. This also explains the large gap amid the permeability values of the gas diffusion layer coated with 0.50 mg/cm² and those coated with greater carbon loadings. So, the addition of some material of polytetrafluoro ethylene to the carbon black decreases the size of the above large pores and thus drops the permeability. For relatively large carbon loadings, i.e., 1.5, 2.0, and 2.5 mg/cm², the carbon loading is appropriately high to cover the large pores on the substrate's surface and "absorb" the moderately low additional quantity of polytetrafluoro ethylene.

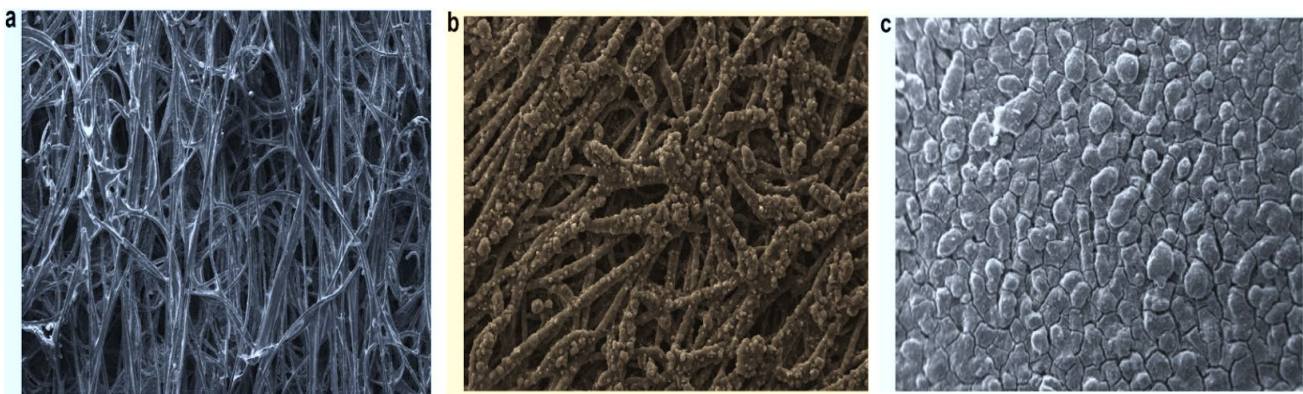


Figure 26. Typical surface SEM images for (a) carbon substrate sample (b) micro-porous layer-coated gas diffusion layer with 0.5 mg/cm² carbon loading and (c) micro-porous layer-coated gas diffusion layer with 2.0 mg/cm² carbon loading [185].

As clarified above, the additional particles of polytetrafluoro ethylene raise the micro-porous layer's porosity and permeability. The 1.0 mg/cm² carbon loading is completed once the above competing influencings of the 10 percent polytetrafluoro ethylene loading are counterbalanced. However, the above explanation for the trends in the polytetrafluoro ethylene loading range from 0 to 10 percent needs some enhancing evidence, so a further complementary study is necessary [185].

4.5. High-Temperature Hydroxide Conductivity

Figure 27a displays the anion conductivity of the anion exchange membrane for the duration of decarbonation. Following 1 h of stabilization at 60 °C, a direct current of 0.10 mA was applied, producing OH⁻ via water electrolysis and HCO₃⁻ to be purged from the anion exchange membrane via the evolution of CO₂. For the duration of the exchange of the HCO₃⁻ to OH⁻, as in Figure 27a blue, the conductivity quickly rises (OH⁻ ions have higher mobility). After 30–40 h, the anion exchange membrane is in its true OH⁻ form, yielding a stable conductivity plateau recognized as the proper OH⁻ conductivity (166 mS/cm, cf. 152 mS/cm reported by Zhegur-Khais et al. [189]). The transient and sharp rises in the conductivities are firstly seen as the temperature is elevated first to 80 °C and then to 105 °C because of the temperature and humidity fluctuations after the variations. The anion exchange membrane's true OH⁻ conductivity rises with the temperature (as estimated by [190,191]): values of 190 and 201 mS/cm¹ were attained at 80 °C (Figure 27a green) and 105 °C (Figure 27a red), respectively. Because of the high testing temperature, the accurate OH⁻ conductivity measured is the utmost value reported for the anion exchange membranes. There is a regular linear reduction in the conductivity up to a critical ion exchange capacity; below it, there is a sharp reduction in conductivity,

resulting in an inflection point. At low ion exchange capacity, where water approval is also relatively low, the reduction in conductivity becomes modest and the conductivity values drop to zero. The trend described in the literature amid HCO_3^- conductivity and ion exchange capacity measured for a series of nondegraded membranes is various, presenting a gradual exponential rise in the ion exchange capacity [192,193]. The ideal anion exchange membrane must have high hydroxide conductivity and chemical stability. At relevant fuel cell temperatures, the anion exchange membrane is unstable and the cationic sites are subject to degradation in the alkaline environs present for the duration of the anion exchange membrane fuel cell procedure [194].

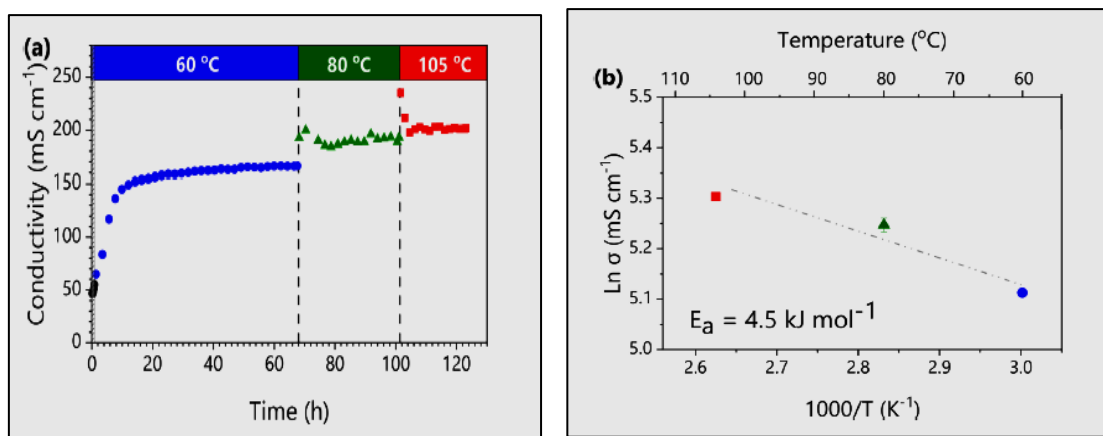


Figure 27. (a) “True” OH^- conductivity (four-probe) of the radiation-grafted ETFEBTMA-based anion exchange membrane, estimated at 60, 80, and 105 °C. Conditions: 0.1 mA direct current, N_2 flow of 500 mL/min at relative humidity of 90% (b). Arrhenius plots utilizing the data extracted from (a) [195].

It could be concluded that the hydroxide conductivity of the PEEK/QA-P(ES1-co-ES2)-20 membrane was appropriate, especially in the range of temperature of 50–90 °C [196]. A number of researchers have suggested that hydronium ions can be obviously integrated into the hydrogen-bonding network of water, while hydroxide ions tend to have stable solvation shells that reorder the solvent molecules and disturb the hydrogen-bond network [197].

The activation energy (E_a) of 4.5 kJ/mol (0.045 eV), estimated from the definite OH^- conductivities of the anion exchange membrane (Figure 27b), is amongst the lowermost reported for anion exchange membranes and is even lesser than that of the Nafion[®] H^+ conducting membrane [195,198]. A low E_a value is desirable, as it shows a lesser barrier for the OH^- conduction. Moreover, the greater mobility of the OH^- ions and the augmented hydration levels at the great temperature (formation of continuous hydrated ion-conducting channels over the anion exchange membrane [199,200]) contribute to the low E_a values, which are wholly consistent with the OH^- transportation happening using a Grotthuss-type mechanism [201,202].

The actual hydroxide conductivity [203,204] of the LDPE-BTMA AEM was determined at 40 and 110 °C. As seen in Figure 28, at 40 °C, the true hydroxide conductivity reaches a very high value of 130 mS/cm. This high conductivity is reliable with the values formerly reported [205]. An estimated Arrhenius-type temperature dependency of the conductivity was noted for these nominated membranes at the temperature range of 30–80 °C. QPAF-DMBA (1.33 mequiv/g) showed the utmost conductivity (152 mS/cm at 80 °C) [206]. The hydroxide ion conductivity measurements confirmed the superior chemical stability of the synthesized poly fluorene ionomers in high-pH solution at raised temperatures [207]. After 1:30 h of equilibration at 40 °C and 90% RH, 1.75 V was carried out across the membrane to generate OH^- at the cathode. A regular rise in membrane conductivity was noted because of a rise in the hydroxide content within the membrane [208]. The hydroxide conductivity at 25 and 80 °C was 95.2 and 198 mS/cm, respectively [193].

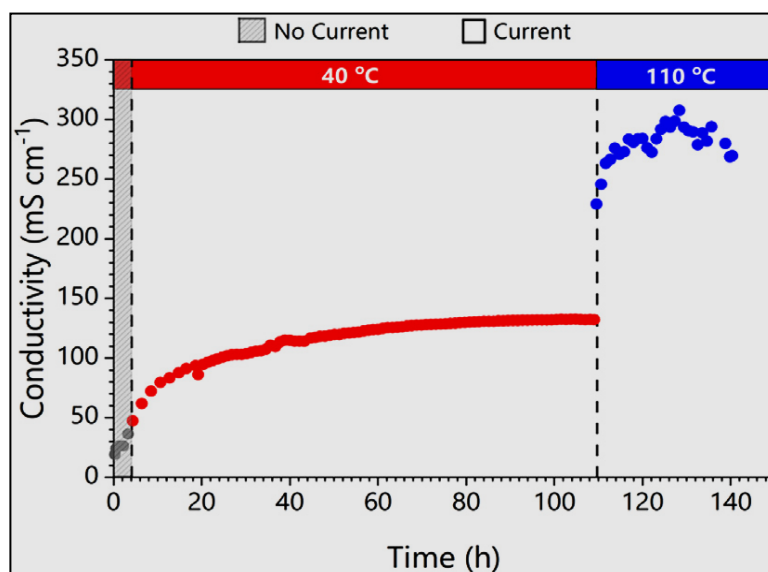


Figure 28. “True” hydroxide conductivity (four-probe) of the LDPE-BTMA AEM, determined at 40 and 110 °C. Conditions: 0.1 mA direct current, under nitrogen flow at RH of 95% [163].

At the high temperature of 110 °C, the anion exchange membrane reaches an outstanding high hydroxide conductivity value of 290 mS/cm (Figure 28). However, at this temperature, the reading tends to be a little noisy (analogous to those measured in reports [204,205]), the anion exchange membrane displays evident stability at this temperature, as exposed by the steady, definite hydroxide conductivity measured for more than 24 h for the duration of the test time (Figure 28, in blue).

4.6. Transportation of Water with Inert Humidified Gas

For the experiments in inert humidified gas, in Figure 29a, the variance in water partial pressure (water activity) amid the two sides of the membrane electrode assembly is the only driving force for water transport across the membrane. The two sides are named A and B in the following discussion. Figure 30a displays a typical flux measurement. Side A has a greater inlet relative humidity, here constant at 86%, while side B is firstly set to 60%. After steady-state data have been attained for roughly 100 s, the temperature setpoint of the humidifier on side B is reduced to reach a relative humidity of 51%. As realized, it takes approximately 2000 s for the new humidity to stabilize because of the humidifier cooling. At this point, a new steady-state condition is reached; in this case, there is a relative humidity of 86% for the side A and relative humidity of 51% for the side B inlets. The relative humidity variation amid sides A and B at the outlets is lesser than at the inlets, which means that water readily disperses over the membrane. A mass balance of water over the cell displays that the loss in A corresponds to the gain in B. This refers to no loss or accumulation of water for the duration of these measurements, which could happen because of gas leaks or condensation of water within the system, as both procedures drop the overall quantity of water [209].

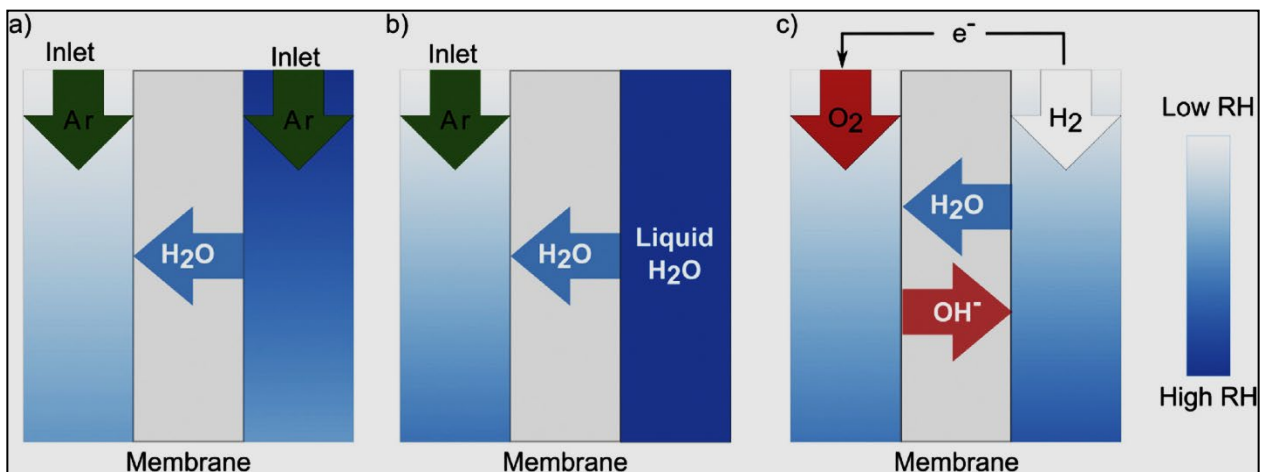


Figure 29. Visualization of achieved experiments to calculate the water flux across the membrane. (a) Flux of vaporous water in argon once the two sides have various inlet relative humidity, (b) Flux of water once one side is in interaction with liquid water and the other with vaporous water in argon. (c) Water flux when both sides have a similar inlet relative humidity and a current is carried out [209].

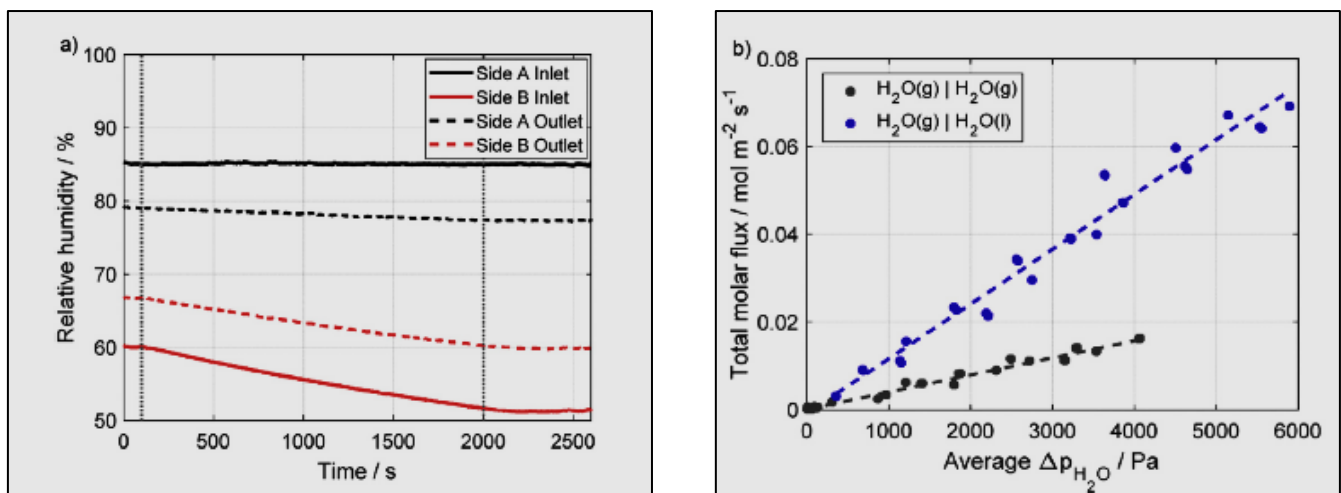


Figure 30. (a) Steady-state measurement of flux over the membrane attained under constant argon flow of 7.33 lnh⁻¹ on both sides and a cell temperature of 50 °C. The humidification of the inlet gas was set to 86% at side A and diverse from 51–60% at side B. Vertical dotted lines refer to the interval when the relative humidity is varied. (b) The overall molar flux of water across the cell as a function of average pressure. The standard errors are assessed to 0.95 and 3.96 mmol/m² s for the vaporous (grey) and liquid (blue) measurements, respectively. Trend lines are for visual aid only [209].

The molar flux of water crossways through the membrane can be counted from the local temperature T and relative humidity RH , recorded via the humidity sensors. The variations in partial pressure of water are utilized to estimate the molar flows of water in the gas stream, supposing that the system's dry flow and total pressure are fixed as stated by the equations below:

$$P_{\text{H}_2\text{O}} = \left(\frac{RH}{100} \right) P_{\text{H}_2\text{O}}^{\text{sat}}(T) \quad (11)$$

$$N_{\text{H}_2\text{O}} = N_{\text{Dry}} \left(\frac{P_{\text{H}_2\text{O}}}{P - P_{\text{H}_2\text{O}}} \right) \quad (12)$$

Equation (11) explains the linear relationship amid relative humidity and the partial pressure of water; $P_{\text{H}_2\text{O}}$, for a specified vapor saturation pressure, $P_{\text{H}_2\text{O}}^{\text{sat}}(T)$. The value for $P_{\text{sat}}(T)$ was estimated utilizing a modified Antoine equation with coefficients defined in [210].

Equation (12) describes the non-linear relationship amid the partial pressure of water, $P_{\text{H}_2\text{O}}$, and the molar flow of water in the gas stream, $N_{\text{H}_2\text{O}}$. The dry molar flow, N_{Dry} , is estimated from the volumetric flow rate over the ideal gas law. The profile of RH over the cell is not recognized. Here, it is as a first calculation supposed to be linear. The average pressure variance of water amid A and B is provided by:

$$\Delta P_{\text{H}_2\text{O}, \text{ave.}} = \frac{(P_{\text{H}_2\text{O},\text{A}} - P_{\text{H}_2\text{O},\text{B}})_{\text{in.}} + (P_{\text{H}_2\text{O},\text{A}} - P_{\text{H}_2\text{O},\text{B}})_{\text{out.}}}{2} \quad (13)$$

Utilizing Equations (11)–(13) for numerous combinations of inlet relative humidities, the molar fluxes versus average water pressure variance can be plotted as exposed in Figure 30b. The linear trend displays that the flux is directly proportional to the partial pressure variation. The major driving force for the flux is the variance in partial pressure of water between the two sides. The linear trend proposes that the membrane water content varies with relative humidity and does not affect the transport properties. The experiments with liquid water on one side, Figure 29b, were also completed to the ones exposed in Figure 30a. The flux when utilizing liquid water on one side is included in Figure 30b, utilizing a constant partial pressure equal to the saturation pressure on the liquid waterside in Equation (13). When one side is present in liquid water, the flux rises roughly three times for the similar driving force. The usually greater water flux noted when utilizing liquid water displays that the transportation of water is phase-dependent, depending on the previous outcomes on Nafion[®] and Fumapem[®] FAA3 membranes [211].

5. Conclusions

Fuel cells that are presently under enormous study can be classified into several types as polymer exchange membrane fuel cells (i.e., proton exchange membrane fuel cells (PEMFCs), solid oxide fuel cells, alkaline fuel cells (AFCs), phosphoric acid, and molten carbonate fuel cells. Investigations have been performed to classify the fuel cells, membrane, and operating parameters. This work critically reviewed the operating factors containing the relative humidity of inlet gas flow direction, operating temperature, various PTFE loadings in GDLs and MPLs, high-temperature hydroxide conductivity, and water transport with inert humidified gas. The main observations can be summarized as follows:

1. For AFCs, generally, the liquid electrolyte used is an aqueous KOH solution. However, the presence of CO₂ in the air feed stream leads to the formation of carbonate precipitation via the formation of large metal carbonate crystals, which might close the pores of the GDL on the electrode. Moreover, the inadequacy and instability could be attributed to the positive ionic sets and the moveable negatively charged anions within AEMs.
2. PEMFCs, which ordinarily produce electricity over a chemical reaction amid hydrogen and oxygen or another oxidizing agent, have become more abundant in recent years because of their essential benefits. The outstanding characteristics of PEMFCs include: high energy density and efficiency; low working noise, cost, working temperature, and sulfur oxides; zero emissions of nitrogen oxides and CO₂; short startup time; zero corrosion; and long life.
3. SOFCs are a power-producing technology that regularly varies the traditional central system of the power supply into a decentralized power source system and directly installs power generation depending on the power consumption desires at the household position. The important benefit of this structure is its simple structure, which needs neither a separator nor gas storage.
4. PAFCs do not have such a requirement as hydrogen and can be produced in situ from methanol (or similar liquid fuel). This permits phosphoric acid fuel cells to utilize available refueling and distribution systems. A phosphoric acid fuel cell usually houses phosphoric acid (H₃PO₄, PA) trapped in a matrix (normally of silicon carbide,

- SiC) as the electrolyte. Platinum with various loadings on carbon-based GDLs forms the electrodes, i.e., the anode and cathode.
5. MCFCs can be united with gas or steam turbines to attain combined heat and power, developing energy use and conversion efficiency. The molten carbonate fuel cell organizes a mixture of alkali carbonates as the electrolyte and works at intermediate temperatures (550–650 °C) utilizing carbonaceous fuels, for example, the natural gas.
 6. Perfluorosulfonic acid (PFSA) is normally utilized as a proton exchange membrane material for PEM fuel cells. The major chain is Teflon-like and extremely hydrophobic. The sulfonic acid group as an end group of the side chain is greatly hydrophilic; therefore, it permits water adsorption for proton conduction.
 7. The catalyst plays a critical role in dropping the reaction activation barrier. Hydrogen fuel is oxidized in the anode, while the oxygen reduction reaction happens in the cathode. Platinum or its alloy is the prevalent catalyst for the oxygen reduction and hydrogen oxidation reactions. Consequently, the catalyst layer contributes an essential part of the cost of the fuel cell.
 8. When the anion exchange membrane fuel cell is operated at a high cell temperature, the membrane ion conductivity and reaction kinetics at the electrodes can be developed. In contrast, the greater cell operating temperature could contribute to better water transportation in the gas diffusion substrate, driven by shear force and evaporation, resulting in less liquid water entrapped inside the gas diffusion substrate and thus simplifying the permeability of humidified reactant gases and active water removal for the duration of the cell procedure.
 9. The rise of the humidification temperature advances the hydrogen-oxygen reaction at the catalyst and overwhelms the performance degradation produced via inadequate gas concentration. Though, the extreme inlet humidification temperature is prospective to cause internal water flooding.
 10. The flow path in the channels does not meaningfully affect the fuel cell's whole performance since the reactant materials supplied to the CL are not affected by the flow path for these operational conditions.
 11. Especially, a development in the performance of the cell is referred to when raising the polytetrafluoro ethylene loading in the anode microporous layer from 5 to 23%.
 12. For the duration of the exchange of the HCO₃⁻ to OH⁻, the electrolyte's conductivity quickly rises, and the mobility OH⁻ ions are increased. After 30–40 h, the anion exchange membrane is in its true OH⁻ form, yielding a stable conductivity plateau recognized as the proper OH⁻ conductivity (166 mS/cm, cf. 152 mS/cm).
 13. The variance in water partial pressure is the only driving force for the transportation of water crossways in the membrane (water activity) amid the two sides of the membrane exchange assembly.

Author Contributions: N.H.J.: Conceptualization and writing. A.A.Y.: Conceptualization and writing. A.R.A.-S.: Conceptualization and writing. H.G.S.: Conceptualization and writing. K.T.R.: Conceptualization and writing. S.A.-S.: Conceptualization, writing and editing. A.A.A.: Conceptualization, and writing. I.K.S.: Conceptualization and writing. A.Z.: Conceptualization and writing. Q.F.A.: Conceptualization, writing and editing. All authors have read and agreed to the published version of the manuscript.

Funding: This research received no external funding.

Institutional Review Board Statement: Not applicable.

Informed Consent Statement: Not applicable.

Data Availability Statement: Data is contained within the article.

Acknowledgments: Qusay F. Alsathy would like to thank the Chemical Engineering Department, University of Technology, Iraq.

Conflicts of Interest: The authors declare no conflict of interest.

References

1. Mandal, M. Recent advancement on anion exchange membranes for fuel cell and water electrolysis. *ChemElectroChem* **2021**, *8*, 36–45. [[CrossRef](#)]
2. Cha, M.S.; Lee, J.Y.; Kim, T.-H.; Jeong, H.Y.; Shin, H.Y.; Oh, S.-G.; Hong, Y.T. Preparation and characterization of crosslinked anion exchange membrane (AEM) materials with poly (phenylene ether)-based short hydrophilic block for use in electrochemical applications. *J. Membr. Sci.* **2017**, *530*, 73–83. [[CrossRef](#)]
3. Yang, Q.; Li, L.; Lin, C.X.; Gao, X.L.; Zhao, C.H.; Zhang, Q.G.; Zhu, A.M.; Liu, Q.L. Hyperbranched poly (arylene ether ketone) anion exchange membranes for fuel cells. *J. Membr. Sci.* **2018**, *560*, 77–86. [[CrossRef](#)]
4. Sazali, N.; Wan Salleh, W.N.; Jamaludin, A.S.; Mhd Razali, M.N. New perspectives on fuel cell technology: A brief review. *Membranes* **2020**, *10*, 99. [[CrossRef](#)] [[PubMed](#)]
5. Ramirez-Nava, J.; Martínez-Castrejón, M.; García-Mesino, R.L.; López-Díaz, J.A.; Talavera-Mendoza, O.; Sarmiento-Villagrana, A.; Rojano, F.; Hernández-Flores, G. The Implications of Membranes Used as Separators in Microbial Fuel Cells. *Membranes* **2021**, *11*, 738. [[CrossRef](#)] [[PubMed](#)]
6. Chen, N.; Lee, Y.M. Anion exchange polyelectrolytes for membranes and ionomers. *Prog. Polym. Sci.* **2021**, *113*, 101345. [[CrossRef](#)]
7. Lu, S.; Pan, J.; Huang, A.; Zhuang, L.; Lu, J. Alkaline polymer electrolyte fuel cells completely free from noble metal catalysts. *Proc. Natl. Acad. Sci. USA* **2008**, *105*, 20611–20614. [[CrossRef](#)]
8. Biemolt, J.; Douglin, J.C.; Singh, R.K.; Davydova, E.S.; Yan, N.; Rothenberg, G.; Dekel, D.R. An Anion-Exchange Membrane Fuel Cell Containing Only Abundant and Affordable Materials. *Energy Technol.* **2021**, *9*, 2000909. [[CrossRef](#)]
9. Dekel, D.R. Review of cell performance in anion exchange membrane fuel cells. *J. Power Sources* **2018**, *375*, 158–169. [[CrossRef](#)]
10. Giorgi, L.; Leccese, F. Fuel Cells: Technologies and Applications. *Open Fuel Cells J.* **2013**, *6*, 1–20. [[CrossRef](#)]
11. Omasta, T.; Wang, L.; Peng, X.; Lewis, C.; Varcoe, J.; Mustain, W.E. Importance of balancing membrane and electrode water in anion exchange membrane fuel cells. *J. Power Sources* **2018**, *375*, 205–213. [[CrossRef](#)]
12. Mustain, W.E.; Chatenet, M.; Page, M.; Kim, Y.S. Durability challenges of anion exchange membrane fuel cells. *Energy Environ. Sci.* **2020**, *13*, 2805–2838. [[CrossRef](#)]
13. Dekel, D.R.; Rasin, I.G.; Brandon, S. Predicting performance stability of anion exchange membrane fuel cells. *J. Power Sources* **2019**, *420*, 118–123. [[CrossRef](#)]
14. Mohanty, A.D.; Tignor, S.E.; Sturgeon, M.R.; Long, H.; Pivovar, B.S.; Bae, C. Thermochemical stability study of alkyl-tethered quaternary ammonium cations for anion exchange membrane fuel cells. *J. Electrochem. Soc.* **2017**, *164*, F1279. [[CrossRef](#)]
15. Pan, D.; Pham, T.H.; Jannasch, P. Poly (arylene piperidine) Anion Exchange Membranes with Tunable N-Alicyclic Quaternary Ammonium Side Chains. *ACS Appl. Energy Mater.* **2021**, *4*, 11652–11665. [[CrossRef](#)]
16. Wright, A.G.; Fan, J.; Britton, B.; Weissbach, T.; Lee, H.-F.; Kitching, E.A.; Peckham, T.J.; Holdcroft, S. Hexamethyl-p-terphenyl poly (benzimidazolium): A universal hydroxide-conducting polymer for energy conversion devices. *Energy Environ. Sci.* **2016**, *9*, 2130–2142. [[CrossRef](#)]
17. Hugar, K.M.; Kostalik IV, H.A.; Coates, G.W. Imidazolium cations with exceptional alkaline stability: A systematic study of structure–stability relationships. *J. Am. Chem. Soc.* **2015**, *137*, 8730–8737. [[CrossRef](#)]
18. Nunez, S.A.; Capparelli, C.; Hickner, M.A. N-alkyl interstitial spacers and terminal pendants influence the alkaline stability of tetraalkylammonium cations for anion exchange membrane fuel cells. *Chem. Mater.* **2016**, *28*, 2589–2598. [[CrossRef](#)]
19. Dang, H.-S.; Jannasch, P. Anion-exchange membranes with polycationic alkyl side chains attached via spacer units. *J. Mater. Chem. A* **2016**, *4*, 17138–17153. [[CrossRef](#)]
20. Fan, J.; Wright, A.G.; Britton, B.; Weissbach, T.; Skalski, T.J.; Ward, J.; Peckham, T.J.; Holdcroft, S. Cationic polyelectrolytes, stable in 10 M KOHaq at 100 °C. *ACS Macro Lett.* **2017**, *6*, 1089–1093. [[CrossRef](#)]
21. Mohanty, A.D.; Ryu, C.Y.; Kim, Y.S.; Bae, C. Stable elastomeric anion exchange membranes based on quaternary ammonium-tethered polystyrene-b-poly (ethylene-co-butylene)-b-polystyrene triblock copolymers. *Macromolecules* **2015**, *48*, 7085–7095. [[CrossRef](#)]
22. Dekel, D.R.; Amar, M.; Willdorf, S.; Kosa, M.; Dhara, S.; Diesendruck, C.E. Effect of water on the stability of quaternary ammonium groups for anion exchange membrane fuel cell applications. *Chem. Mater.* **2017**, *29*, 4425–4431. [[CrossRef](#)]
23. Diesendruck, C.E.; Dekel, D.R. Water—A key parameter in the stability of anion exchange membrane fuel cells. *Curr. Opin. Electrochem.* **2018**, *9*, 173–178. [[CrossRef](#)]
24. Willdorf-Cohen, S.; Mondal, A.N.; Dekel, D.R.; Diesendruck, C.E. Chemical stability of poly (phenylene oxide)-based ionomers in an anion exchange-membrane fuel cell environment. *J. Mater. Chem. A* **2018**, *6*, 22234–22239. [[CrossRef](#)]
25. Dekel, D.R.; Willdorf, S.; Ash, U.; Amar, M.; Pusara, S.; Dhara, S.; Srebnik, S.; Diesendruck, C.E. The critical relation between chemical stability of cations and water in anion exchange membrane fuel cells environment. *J. Power Sources* **2018**, *375*, 351–360. [[CrossRef](#)]
26. Merle, G.; Wessling, M.; Nijmeijer, K. Anion exchange membranes for alkaline fuel cells: A review. *J. Membr. Sci.* **2011**, *377*, 1–35. [[CrossRef](#)]
27. Zeng, R.; Varcoe, J. R Alkaline anion exchange membranes for fuel cells—a patent review. *Recent Pat. Chem. Eng.* **2011**, *4*, 93–115. [[CrossRef](#)]
28. McLean, G.; Niet, T.; Prince-Richard, S.; Djilali, N. An assessment of alkaline fuel cell technology. *Int. J. Hydrog. Energy* **2002**, *27*, 507–526. [[CrossRef](#)]

29. Khade, A.R. Anion Exchange Membranes for Alkaline Fuel Cells. *Int. J. Sci. Res.* **2015**, *4*, 1406–1408.
30. Khade, A.R. Fuel Cell Technologies and Applications. *Int. J. Sci. Res.* **2014**, *3*, 978–982.
31. Zagorodni, A.A.; Kotova, D.L.; Selemenev, V.F. Infrared spectroscopy of ion exchange resins: Chemical deterioration of the resins. *React. Funct. Polym.* **2002**, *53*, 157–171. [[CrossRef](#)]
32. Neagu, V.; Bunia, I.; Plesca, I. Ionic polymers VI. Chemical stability of strong base anion exchangers in aggressive media. *Polym. Degrad. Stab.* **2000**, *70*, 463–468. [[CrossRef](#)]
33. Slade, R.C.; Kizewski, J.P.; Poynton, S.D.; Zeng, R.; Varcoe, J.R. Alkaline membrane fuel cells. In *Fuel Cells*; Springer: Berlin/Heidelberg, Germany, 2013; pp. 9–29.
34. Sata, T.; Tsujimoto, M.; Yamaguchi, T.; Matsusaki, K. Change of anion exchange membranes in an aqueous sodium hydroxide solution at high temperature. *J. Membr. Sci.* **1996**, *112*, 161–170. [[CrossRef](#)]
35. Habib, M.S.; Arefin, P.; Salam, M.A.; Ahmed, K.; Uddin, M.S.; Hossain, T.; Papri, N.; Islam, T. Proton Exchange Membrane Fuel Cell (PEMFC) Durability Factors, Challenges, and Future Perspectives: A Detailed Review. *Mat. Sci. Res. India* **2021**, *18*, 217–234. [[CrossRef](#)]
36. Jia, J.; Li, Q.; Wang, Y.; Cham, Y.; Han, M. Modeling and dynamic characteristic simulation of a proton exchange membrane fuel cell. *IEEE Trans. Energy Convers.* **2009**, *24*, 283–291. [[CrossRef](#)]
37. Al-Shamma'a, A.A.; Ali, F.A.A.; Alhoshan, M.S.; Alturki, F.A.; Farh, H.M.; Alam, J.; AlSharabi, K. Proton Exchange Membrane Fuel Cell Parameter Extraction Using a Supply–Demand-Based Optimization Algorithm. *Processes* **2021**, *9*, 1416. [[CrossRef](#)]
38. Chikhaliya, N.P.; Rathwa, Y.J.; Likhariya, T. Polybenzimidazoles as proton exchange membrane in fuel cell applications. *High Perform. Polym.* **2021**, *33*, 998–1011. [[CrossRef](#)]
39. Zou, Y.; Yang, M.; Liu, G.; Xu, C. Sulfonated poly (fluorenyl ether ketone nitrile) membranes used for high temperature PEM fuel cell. *Heliyon* **2020**, *6*, e04855. [[CrossRef](#)]
40. Miyake, J.; Miyatake, K. Fluorine-free sulfonated aromatic polymers as proton exchange membranes. *Polym. J.* **2017**, *49*, 487–495. [[CrossRef](#)]
41. Zheng, P.; Liu, Q.; Li, Z.; Wang, D.; Liu, X. Effect of crosslinking degree on sulfonated poly (aryl ether nitrile) s as candidates for proton exchange membranes. *Polymers* **2019**, *11*, 964. [[CrossRef](#)]
42. Tian, S.; Shu, D.; Wang, S.; Xiao, M.; Meng, Y. Sulfonated poly (fluorenyl ether ketone nitrile) electrolyte membrane with high proton conductivity and low water uptake. *J. Power Sources* **2010**, *195*, 97–103. [[CrossRef](#)]
43. Cocco, D.; Tola, V. Externally reformed solid oxide fuel cell–micro-gas turbine (SOFC–MGT) hybrid systems fueled by methanol and di-methyl-ether (DME). *Energy* **2009**, *34*, 2124–2130. [[CrossRef](#)]
44. Li, W.; Wang, Y.; Liu, W. A review of solid oxide fuel cell application. In *IOP Conference Series: Earth and Environmental Science*; IOP Publishing: Bristol, UK, 2020; p. 619.
45. Hanna, J.; Lee, W.Y.; Shi, Y.; Ghoniem, A.F. Fundamentals of electro- and thermochemistry in the anode of solid-oxide fuel cells with hydrocarbon and syngas fuels. *Prog. Energy Combust. Sci.* **2014**, *40*, 74–111. [[CrossRef](#)]
46. Sadykov, V.A.; Sadvovskaya, E.M.; Ereemeev, N.F.; Pikalova, E.Y.; Bogdanovich, N.M.; Filonova, E.A.; Krieger, T.A.; Fedorova, Y.E.; Krasnov, A.V.; Skriabin, P.I. Novel materials for solid oxide fuel cells cathodes and oxygen separation membranes: Fundamentals of oxygen transport and performance. *Carbon Resour. Convers.* **2020**, *3*, 112–121. [[CrossRef](#)]
47. Sadykov, V.A.; Mezentseva, N.V.; Bobrova, L.; Smorygo, O. Advanced materials for solid oxide fuel cells and membrane catalytic reactors. In *Advanced Nanomaterials for Catalysis and Energy: Synthesis, Characterization and Applications*; Elsevier: Amsterdam, The Netherlands, 2019; Chapter 12; pp. 435–514.
48. Sadykov, V.; Sadvovskaya, E.; Ereemeev, N.; Skriabin, P.; Krasnov, A.; Bepalko, Y.N.; Pavlova, S.; Fedorova, Y.E.; Pikalova, E.Y.; Shlyakhtina, A. Oxygen mobility in the materials for solid oxide fuel cells and catalytic membranes. *Russ. J. Electrochem.* **2019**, *55*, 701–718. [[CrossRef](#)]
49. Sadykov, V.A.; Muzykantov, V.S.; Yeremeev, N.F.; Pelipenko, V.V.; Sadvovskaya, E.M.; Bobin, A.S.; Fedorova, Y.E.; Amanbaeva, D.G.; Smirnova, A.L. Solid oxide fuel cell cathodes: Importance of chemical composition and morphology. *Catal. Sustain. Energy* **2015**, *2*, 57–70. [[CrossRef](#)]
50. Adler, S.B.; Lane, J.; Steele, B. Electrode kinetics of porous mixed-conducting oxygen electrodes. *J. Electrochem. Soc.* **1996**, *143*, 3554. [[CrossRef](#)]
51. Steele, B.C.; Heinzel, A. Materials for fuel-cell technologies. In *Materials for Sustainable Energy: A Collection of Peer-Reviewed Research and Review Articles from Nature Publishing Group*; World Scientific: Singapore, 2011; pp. 224–231.
52. Basu, S. *Fuel Cell Science and Technology*; Springer: Berlin/Heidelberg, Germany, 2007.
53. Sadykov, V.; Ereemeev, N.; Alikina, G.; Sadvovskaya, E.; Muzykantov, V.; Pelipenko, V.; Bobin, A.; Krieger, T.; Belyaev, V.; Ivanov, V. Oxygen mobility and surface reactivity of PrNi1–xCoxO3+δ–CeO. 9Y0. 1O2–δ cathode nanocomposites. *Solid State Ion.* **2014**, *262*, 707–712. [[CrossRef](#)]
54. Sadykov, V.; Ereemeev, N.; Vinokurov, Z.; Shmakov, A.; Kriventsov, V.; Lukashevich, A.; Krasnov, A.; Ishchenko, A. Structural studies of pr nickelate-cobaltite-Y-doped ceria nanocomposite. *J. Ceram. Sci. Technol.* **2017**, *8*, 129–140.
55. Sadykov, V.; Sadvovskaya, E.; Ereemeev, N.; Pikalova, E.; Bogdanovich, N.; Filonova, E.; Fedorova, Y.; Krasnov, A.; Skriabin, P.; Lukashevich, A. Design of materials for solid oxide fuel cells cathodes and oxygen separation membranes based on fundamental studies of their oxygen mobility and surface reactivity. In *E3S Web of Conferences*; EDP Sciences: Wroclaw, Poland, 2019.
56. Wang, H.-S.; Chang, C.-P.; Huang, Y.-J.; Su, Y.-C.; Tseng, F.-G. A high-yield and ultra-low-temperature methanol reformer integratable with phosphoric acid fuel cell (PAFC). *Energy* **2017**, *133*, 1142–1152. [[CrossRef](#)]

57. Bhosale, A.C.; Suseendiran, S.R.; Ramya, R.; Choudhury, S.R.; Rengaswamy, R. 4.17-Phosphoric Acid Fuel Cells. In *Comprehensive Renewable Energy*, 2nd ed.; Letcher, T.M., Ed.; Elsevier: Oxford, UK, 2022; pp. 437–458.
58. Netwall, C.J.; Gould, B.D.; Rodgers, J.A.; Nasello, N.J.; Swider-Lyons, K.E. Decreasing contact resistance in proton-exchange membrane fuel cells with metal bipolar plates. *J. Power Sources* **2013**, *227*, 137–144. [[CrossRef](#)]
59. Tanno, K.; Makino, H. Development tendency and prospect of high performance coal utilization power generation system for low carbon society. *KONA Powder Part. J.* **2018**, *35*, 139–149. [[CrossRef](#)]
60. Hilmi, A.; Yuh, C.; Farooque, M. Fuel Cells—Molten Carbonate Fuel Cells | Anodes. *ECS Trans.* **2014**, *61*. [[CrossRef](#)]
61. Cui, C.; Li, S.; Gong, J.; Wei, K.; Hou, X.; Jiang, C.; Yao, Y.; Ma, J. Review of molten carbonate-based direct carbon fuel cells. *Mater. Renew. Sustain. Energy* **2021**, *10*, 1–24.
62. Xing, H.; Stuart, C.; Spence, S.; Chen, H. Fuel cell power systems for maritime applications: Progress and perspectives. *Sustainability* **2021**, *13*, 1213. [[CrossRef](#)]
63. Brunetti, A.; Scura, F.; Barbieri, G.; Drioli, E. Membrane technologies for CO₂ separation. *J. Membr. Sci.* **2010**, *359*, 115–125. [[CrossRef](#)]
64. Merkel, T.C.; Lin, H.; Wei, X.; Baker, R. Power plant post-combustion carbon dioxide capture: An opportunity for membranes. *J. Membr. Sci.* **2010**, *359*, 126–139. [[CrossRef](#)]
65. Zhao, L.; Riensche, E.; Blum, L.; Stolten, D. Multi-stage gas separation membrane processes used in post-combustion capture: Energetic and economic analyses. *J. Membr. Sci.* **2010**, *359*, 160–172. [[CrossRef](#)]
66. Hu, Q.; Marand, E.; Dhingra, S.; Fritsch, D.; Wen, J.; Wilkes, G. Poly (amide-imide)/TiO₂ nano-composite gas separation membranes: Fabrication and characterization. *J. Membr. Sci.* **1997**, *135*, 65–79. [[CrossRef](#)]
67. Kawakami, M.; Iwanaga, H.; Hara, Y.; Iwamoto, M.; Kagawa, S. Gas permeabilities of cellulose nitrate/poly (ethylene glycol) blend membranes. *J. Appl. Polym. Sci.* **1982**, *27*, 2387–2393. [[CrossRef](#)]
68. Ma'mum, S.; Svendsen, H.F.; Hoff, K.A.; Juliussen, O. Selection of new absorbents for carbon dioxide capture. In *Greenhouse Gas Control Technologies 7*; Elsevier: Amsterdam, The Netherlands, 2005; pp. 45–53.
69. Lin, H.; Freeman, B.D. Materials selection guidelines for membranes that remove CO₂ from gas mixtures. *J. Mol. Struct.* **2005**, *739*, 57–74. [[CrossRef](#)]
70. Chen, H.Z.; Li, P.; Chung, T.-S. PVDF/ionic liquid polymer blends with superior separation performance for removing CO₂ from hydrogen and flue gas. *Int. J. Hydrog. Energy* **2012**, *37*, 11796–11804. [[CrossRef](#)]
71. Alhassan, M.; Garba, M.U. Design of an Alkaline Fuel Cell. *Leonardo Electron. J. Pract. Technol.* **2006**, *5*, 99–106.
72. Ariyanfar, L.; Ghadaman, H.; Roshandel, R. Alkaline Fuel Cell (AFC) engineering design, modeling and simulation for UPS provide in laboratory application. In *World Renewable Energy Congress-Sweden, Linköping; Sweden, 8–13 May; 2011*; Linköping Electronic Press: Linköping, Sweden, 2011.
73. Zhang, S.; Reimer, U.; Rahim, Y.; Beale, S.B.; Lehnert, W. Numerical modeling of polymer electrolyte fuel cells with analytical and experimental validation. *J. Electrochem. Energy Convers. Storage* **2019**, *16*, 031002. [[CrossRef](#)]
74. Buasri, P.; Salameh, Z.M. An electrical circuit model for a proton exchange membrane fuel cell (PEMFC). In Proceedings of the 2006 IEEE Power Engineering Society General Meeting, Montreal, QC, Canada, 18–22 June 2006.
75. Goodenough, J.B.; Huang, Y.-H. Alternative anode materials for solid oxide fuel cells. *J. Power Sources* **2007**, *173*, 1–10. [[CrossRef](#)]
76. Holcomb, F.H.B.; Taylor, M.J.; Torrey, W.R.; Westerman, J.M.; John, F. *Phosphoric Acid Fuel Cells*; E.R.a.D. Center, Ed.; Defense Technical Information Center: Fort Belvoir, VI, USA, 2000.
77. Zhang, H.; Lin, G.; Chen, J. Performance analysis and multi-objective optimization of a new molten carbonate fuel cell system. *Int. J. Hydrog. Energy* **2011**, *36*, 4015–4021. [[CrossRef](#)]
78. Wang, Y.; Seo, B.; Wang, B.; Zamel, N.; Jiao, K.; Adroher, X.C. Fundamentals, materials, and machine learning of polymer electrolyte membrane fuel cell technology. *Energy AI* **2020**, *1*, 100014. [[CrossRef](#)]
79. Ma, Y.-L.; Wainright, J.; Litt, M.; Savinell, R. Conductivity of PBI membranes for high-temperature polymer electrolyte fuel cells. *J. Electrochem. Soc.* **2003**, *151*, A8. [[CrossRef](#)]
80. Zhang, J.; Xie, Z.; Zhang, J.; Tang, Y.; Song, C.; Navessin, T.; Shi, Z.; Song, D.; Wang, H.; Wilkinson, D.P. High temperature PEM fuel cells. *J. Power Sources* **2006**, *160*, 872–891. [[CrossRef](#)]
81. Zaidi, J.; Matsuura, T. *Polymer Membranes for Fuel Cells*; Springer: Cham, Switzerland, 2009; pp. 1–431.
82. Shi, S.; Weber, A.Z.; Kusoglu, A. Structure/property relationship of Nafion XL composite membranes. *J. Membr. Sci.* **2016**, *516*, 123–134. [[CrossRef](#)]
83. Eisenberg, A.; Yeager, H.L. *Perfluorinated Ionomer Membranes*; ACS Publications: Washington, DC, USA, 1982.
84. Kreuer, K.D.; Rabenau, A.; Weppner, W. Vehicle mechanism, a new model for the interpretation of the conductivity of fast proton conductors. *Angew. Chem. Int. Ed. Engl.* **1982**, *21*, 208–209. [[CrossRef](#)]
85. Kornyshev, A.; Kuznetsov, A.; Spohr, E.; Ulstrup, J. *Kinetics of Proton Transport in Water*; ACS Publications: Washington, DC, USA, 2003; pp. 3351–3366.
86. Marx, D.; Tuckerman, M.E.; Hutter, J.; Parrinello, M. The nature of the hydrated excess proton in water. *Nature* **1999**, *397*, 601–604. [[CrossRef](#)]
87. Springer, T.E.; Zawodzinski, T.; Gottesfeld, S. Polymer electrolyte fuel cell model. *J. Electrochem. Soc.* **1991**, *138*, 2334. [[CrossRef](#)]
88. Wu, J.; Yuan, X.Z.; Martin, J.J.; Wang, H.; Zhang, J.; Shen, J.; Wu, S.; Merida, W. A review of PEM fuel cell durability: Degradation mechanisms and mitigation strategies. *J. Power Sources* **2008**, *184*, 104–119. [[CrossRef](#)]

89. Kraysberg, A.; Ein-Eli, Y. Review of advanced materials for proton exchange membrane fuel cells. *Energy Fuels* **2014**, *28*, 7303–7330. [[CrossRef](#)]
90. Mehta, V.; Cooper, J.S. Review and analysis of PEM fuel cell design and manufacturing. *J. Power Sources* **2003**, *114*, 32–53. [[CrossRef](#)]
91. Yu, J.; Yi, B.; Xing, D.; Liu, F.; Shao, Z.; Fu, Y.; Zhang, H. Degradation mechanism of polystyrene sulfonic acid membrane and application of its composite membranes in fuel cells. *Phys. Chem. Chem. Phys.* **2003**, *5*, 611–615. [[CrossRef](#)]
92. Adanur, S.; Zheng, H. Synthesis and characterization of sulfonated polyimide based membranes for proton exchange membrane fuel cells. *J. Fuel Cell Sci. Technol.* **2013**, *10*, 041001. [[CrossRef](#)]
93. Hwang, K.; Kim, J.-H.; Kim, S.-Y.; Byun, H. Preparation of polybenzimidazole-based membranes and their potential applications in the fuel cell system. *Energies* **2014**, *7*, 1721–1732. [[CrossRef](#)]
94. Gao, Y.; Zhang, Z.; Zhong, S.; Daneshfar, R. Preparation and Application of Aromatic Polymer Proton Exchange Membrane with Low-Sulfonation Degree. *Int. J. Chem. Eng.* **2020**, *2020*, 8834471. [[CrossRef](#)]
95. Zamel, N. The catalyst layer and its dimensionality—A look into its ingredients and how to characterize their effects. *J. Power Sources* **2016**, *309*, 141–159. [[CrossRef](#)]
96. Lufrano, F.; Squadrito, G.; Patti, A.; Passalacqua, E. Sulfonated polysulfone as promising membranes for polymer electrolyte fuel cells. *J. Appl. Polym. Sci.* **2000**, *77*, 1250–1256. [[CrossRef](#)]
97. Wang, L.; Liu, Y.; Yang, X.; Fang, Y.; Chen, Y.; Wang, Y. A high-performance direct methanol fuel cell with a polymer fiber membrane and RuO₂/CNTs as a cathode catalyst. *J. Mater. Chem. A* **2013**, *1*, 1834–1839. [[CrossRef](#)]
98. Salleh, M.T.; Jaafar, J.; Mohamed, M.; Norddin, M.; Ismail, A.; Othman, M.; Rahman, M.; Yusof, N.; Aziz, F.; Salleh, W. Stability of SPEEK/Cloisite®/TAP nanocomposite membrane under Fenton reagent condition for direct methanol fuel cell application. *Polym. Degrad. Stab.* **2017**, *137*, 83–99. [[CrossRef](#)]
99. Gupta, D.; Choudhary, V. Non-fluorinated hybrid composite membranes based on polyethylene glycol functionalized polyhedral oligomeric silsesquioxane [PPOSS] and sulfonated poly(ether ether ketone) [SPEEK] for fuel cell applications. *React. Funct. Polym.* **2013**, *73*, 1268–1280. [[CrossRef](#)]
100. Ni, C.; Wei, Y.; Zhao, Q.; Liu, B.; Sun, Z.; Gu, Y.; Zhang, M.; Hu, W. Novel proton exchange membranes based on structure-optimized poly(ether ether ketone) and nanocrystalline cellulose. *Appl. Surf. Sci.* **2018**, *434*, 163–175. [[CrossRef](#)]
101. Wang, W.; Wang, S.; Li, W.; Xie, X.; Lv, Y. Synthesis and characterization of a fluorinated cross-linked anion exchange membrane. *Int. J. Hydrog. Energy* **2013**, *38*, 11045–11052. [[CrossRef](#)]
102. Ko, B.-S.; Sohn, J.-Y.; Shin, J. Radiation-induced synthesis of solid alkaline exchange membranes with quaternized 1,4-diazabicyclo[2,2,2] octane pendant groups for fuel cell application. *Polymer* **2012**, *53*, 4652–4661. [[CrossRef](#)]
103. Razmi, A.; Alirahmi, S.; Nabat, M.; Assareh, E.; Shahbakhti, M. A green hydrogen energy storage concept based on parabolic trough collector and proton exchange membrane electrolyzer/fuel cell: Thermodynamic and exergoeconomic analyses with multi-objective optimization. *Int. J. Hydrog. Energy* **2022**, *47*, 26468–26489. [[CrossRef](#)]
104. Elumalai, V.; Sangeetha, D. Anion exchange composite membrane based on octa quaternary ammonium Polyhedral Oligomeric Silsesquioxane for alkaline fuel cells. *J. Power Sources* **2018**, *375*, 412–420. [[CrossRef](#)]
105. Lade, H.; Kumar, V.; Arthanareeswaran, G.; Ismail, A. Sulfonated poly(arylene ether sulfone) nanocomposite electrolyte membrane for fuel cell applications: A review. *Int. J. Hydrog. Energy* **2017**, *42*, 1063–1074. [[CrossRef](#)]
106. Kim, D.J.; Jo, M.J.; Nam, S.Y. A review of polymer–nanocomposite electrolyte membranes for fuel cell application. *J. Ind. Eng. Chem.* **2015**, *21*, 36–52. [[CrossRef](#)]
107. Fang, F.; Liu, L.; Min, L.; Xu, L.; Zhang, W.; Wang, Y. Enhanced proton conductivity of Nafion membrane with electrically aligned sulfonated graphene nanoplates. *Int. J. Hydrog. Energy* **2021**, *4*, 17784–17792. [[CrossRef](#)]
108. Yu, P.; Pemberton, M.; Plasse, P. PtCo/C cathode catalyst for improved durability in PEMFCs. *J. Power Sources* **2005**, *144*, 11–20. [[CrossRef](#)]
109. Ferreira, P.; Shao-Horn, Y.; Morgan, D.; Makharia, R.; Kocha, S.; Gasteiger, H. Instability of Pt/C electrocatalysts in proton exchange membrane fuel cells: A mechanistic investigation. *J. Electrochem. Soc.* **2005**, *152*, A2256. [[CrossRef](#)]
110. Vielstich, W.; Lamm, A.; Gasteiger, H. *Handbook of Fuel Cells: Fundamentals, Technology, Applications*; Wiley: Hoboken, NJ, USA, 2003.
111. Debe, M. *Advanced Cathode Catalysts and Supports for PEM Fuel Cells*; 3M Company: Maplewood, MN, USA, 2012.
112. Debe, M.K. Electrocatalyst approaches and challenges for automotive fuel cells. *Nature* **2012**, *48*, 43–51. [[CrossRef](#)]
113. Rao, R.M.; Rengaswamy, R. Optimization study of an agglomerate model for platinum reduction and performance in PEM fuel cell cathode. *Chem. Eng. Res. Des.* **2006**, *84*, 952–964.
114. Van Der Vliet, D.F.; Wang, C.; Tripkovic, D.; Strmcnik, D.; Zhang, X.F.; Debe, M.K.; Atanasoski, R.T.; Markovic, N.M.; Stamenkovic, V.R. Mesoporous thin films as electrocatalysts with tunable composition and surface morphology. *Nat. Mater.* **2012**, *11*, 1051–1058. [[CrossRef](#)]
115. Wang, Y.; Feng, X. Analysis of the reaction rates in the cathode electrode of polymer electrolyte fuel Cells: II. Dual-Layer electrodes. *J. Electrochem. Soc.* **2009**, *156*, B403. [[CrossRef](#)]
116. Feng, X.; Wang, Y. Multi-layer configuration for the cathode electrode of polymer electrolyte fuel cell. *Electrochim. Acta* **2010**, *55*, 4579–4586. [[CrossRef](#)]
117. He, W.; Yi, J.S.; van Nguyen, T. Two-phase flow model of the cathode of PEM fuel cells using interdigitated flow fields. *AIChE J.* **2000**, *46*, 2053–2064. [[CrossRef](#)]

118. Banham, D.; Ye, S. Current status and future development of catalyst materials and catalyst layers for proton exchange membrane fuel cells: An industrial perspective. *ACS Energy Lett.* **2017**, *2*, 629–638. [[CrossRef](#)]
119. Othman, R.; Dicks, A.L.; Zhu, Z. Non Precious Metal Catalysts for the PEM Fuel Cell Cathode. *Int. J. Hydrog. Energy* **2012**, *37*, 357–372. [[CrossRef](#)]
120. Mukherjee, P.P.; Wang, C.-Y. Direct numerical simulation modeling of bilayer cathode catalyst layers in polymer electrolyte fuel cells. *J. Electrochem. Soc.* **2007**, *154*, B1121. [[CrossRef](#)]
121. Wang, G.; Mukherjee, P.P.; Wang, C.-Y. Direct numerical simulation (DNS) modeling of PEFC electrodes: Part I. Regular microstructure. *Electrochim. Acta* **2006**, *51*, 3139–3150. [[CrossRef](#)]
122. Wang, G.; Mukherjee, P.P.; Wang, C.-Y. Direct numerical simulation (DNS) modeling of PEFC electrodes: Part II. Random microstructure. *Electrochim. Acta* **2006**, *51*, 3151–3160. [[CrossRef](#)]
123. Wang, Y.; Feng, X. Analysis of reaction rates in the cathode electrode of polymer electrolyte fuel cell I. Single-layer electrodes. *J. Electrochem. Soc.* **2008**, *155*, B1289. [[CrossRef](#)]
124. Mathias, M.; Roth, J.; Fleming, J.; Lehnert, W. Diffusion media materials and characterisation. *Handb. Fuel Cells—Fundam. Technol. Appl.* **2003**, *3*, 517–537.
125. Larminie, J.; Dicks, A.; McDonald, M.S. *Fuel Cell Systems Explained*; Wiley: Chichester, UK, 2003; Volume 2.
126. Sasikumar, G.; Ihm, J.; Ryu, H. Dependence of optimum Nafion content in catalyst layer on platinum loading. *J. Power Sources* **2004**, *132*, 11–17. [[CrossRef](#)]
127. Cindrella, L.; Kannan, A.M.; Lin, J.; Saminathan, K.; Ho, Y.; Lin, C.; Wertz, J. Gas diffusion layer for proton exchange membrane fuel cells—A review. *J. Power Sources* **2009**, *194*, 146–160. [[CrossRef](#)]
128. Kannan, A.M.; Veedu, V.P.; Munukutla, L.; Ghasemi-Nejhad, M.N. Nanostructured Gas Diffusion and Catalyst Layers for Proton Exchange Membrane Fuel Cells. *Electrochem. Solid-State Lett.* **2007**, *10*, B47. [[CrossRef](#)]
129. Lim, C.; Wang, C. Effects of hydrophobic polymer content in GDL on power performance of a PEM fuel cell. *Electrochim. Acta* **2004**, *49*, 4149–4156. [[CrossRef](#)]
130. Chen, T.; Liu, S.; Zhang, J.; Tang, M. Study on the characteristics of GDL with different PTFE content and its effect on the performance of PEMFC. *Int. J. Heat Mass Transf.* **2019**, *128*, 1168–1174. [[CrossRef](#)]
131. Cindrella, L.; Kannan, A.M.; Ahmad, R.; Thommes, M. Surface modification of gas diffusion layers by inorganic nanomaterials for performance enhancement of proton exchange membrane fuel cells at low RH conditions. *Int. J. Hydrog. Energy* **2009**, *34*, 6377–6383. [[CrossRef](#)]
132. Zamel, N.; Li, X. Effect of contaminants on polymer electrolyte membrane fuel cells. *Prog. Energy Combust. Sci.* **2011**, *37*, 292–329. [[CrossRef](#)]
133. Wood, D.L.; Rulison, C.; Borup, R.L. Surface properties of PEMFC gas diffusion layers. *J. Electrochem. Soc.* **2009**, *157*, B195. [[CrossRef](#)]
134. Wang, Y.; Chen, K.S.; Mishler, J.; Cho, S.C.; Adroher, X.C. A review of polymer electrolyte membrane fuel cells: Technology, applications, and needs on fundamental research. *Appl. Energy* **2011**, *88*, 981–1007. [[CrossRef](#)]
135. Mukherjee, P.P.; Mukundan, R.; Borup, R.L. Modeling of durability effect on the flooding behavior in the PEFC gas diffusion layer. In *International Conference on Fuel Cell Science, Engineering and Technology*; ASME: New York, NY, USA, 2010.
136. Qi, Z.; Kaufman, A. Improvement of water management by a microporous sublayer for PEM fuel cells. *J. Power Sources* **2002**, *109*, 38–46. [[CrossRef](#)]
137. Wargo, E.; Schulz, V.; Çeçen, A.; Kalidindi, S.; Kumbur, E. Resolving macro-and micro-porous layer interaction in polymer electrolyte fuel cells using focused ion beam and X-ray computed tomography. *Electrochim. Acta* **2013**, *87*, 201–212. [[CrossRef](#)]
138. Zamel, N.; Litovsky, E.; Shakhshir, S.; Li, X.; Kleiman, J. Measurement of in-plane thermal conductivity of carbon paper diffusion media in the temperature range of $-20\text{ }^{\circ}\text{C}$ to $+120\text{ }^{\circ}\text{C}$. *Appl. Energy* **2011**, *88*, 3042–3050. [[CrossRef](#)]
139. Weber, A.Z.; Newman, J. Effects of microporous layers in polymer electrolyte fuel cells. *J. Electrochem. Soc.* **2005**, *152*, A677. [[CrossRef](#)]
140. Nagai, Y.; Eller, J.; Hatanaka, T.; Yamaguchi, S.; Kato, S.; Kato, A.; Marone, F.; Xu, H.; Büchi, F.N. Improving water management in fuel cells through microporous layer modifications: Fast operando tomographic imaging of liquid water. *J. Power Sources* **2019**, *435*, 226809. [[CrossRef](#)]
141. Chen, Y.; Liu, Y.; Xu, Y.; Guo, X.; Cao, Y.; Ming, W. Review: Modeling and Simulation of Membrane Electrode Material Structure for Proton Exchange Membrane Fuel Cells. *Coatings* **2022**, *12*, 1145. [[CrossRef](#)]
142. Atkinson, R.W.; Rodgers, J.A.; Hazard, M.W.; Stroman, R.O.; Gould, B.D. Influence of Cathode Gas Diffusion Media Porosity on Open-Cathode Fuel Cells. *J. Electrochem. Soc.* **2018**, *165*, F1002. [[CrossRef](#)]
143. Mezedur, M.M.; Kaviani, M.; Moore, W. Effect of Pore Structure, Randomness and Size on Effective Mass Diffusivity. *AIChE J.* **2002**, *48*, 15–24. [[CrossRef](#)]
144. Martínez, M.J.; Shimpalee, S.; van Zee, J.W. Measurement of MacMullin Numbers for PEMFC Gas-Diffusion Media. *J. Electrochem. Soc.* **2009**, *156*, B80. [[CrossRef](#)]
145. Nam, J.H.; Lee, K.; Hwang, G.; Kim, C.; Kaviani, M. Microporous layer for water morphology control in PEMFC. *Int. J. Heat Mass Transf.* **2009**, *52*, 2779–2791. [[CrossRef](#)]
146. El-Kharouf, A.; Rees, N.V.; Steinberger-Wilckens, R. Gas Diffusion Layer Materials and their Effect on Polymer Electrolyte Fuel Cell Performance—Ex Situ and In Situ Characterization. *Fuel Cells* **2014**, *14*, 735–741. [[CrossRef](#)]

147. Navarro, A.J.; Gomez, A.M.; Daza, L.; Molina-Garcia, A.; Lopez-Cascales, J.J. Influence of the gas diffusion layer on the performance of an open cathode polymer electrolyte membrane fuel cell. *Int. J. Hydrog. Energy* **2022**, *47*, 7990–7999. [[CrossRef](#)]
148. Sun, W.; Peppley, B.A.; Karan, K. Modeling the Influence of GDL and flow-field plate parameters on the reaction distribution in the PEMFC cathode catalyst layer. *J. Power Sources* **2005**, *144*, 42–53. [[CrossRef](#)]
149. Saebea, D.; Chaiburi, C.; Authayanun, S. Model based evaluation of alkaline anion exchange membrane fuel cells with water management. *Chem. Eng. J.* **2019**, *374*, 721–729. [[CrossRef](#)]
150. Wang, T.; Shi, L.; Wang, J.; Zhao, Y.; Setzler, B.P.; Rojas-Carbonell, S.; Yan, Y. High-performance hydroxide exchange membrane fuel cells through optimization of relative humidity, backpressure and catalyst selection. *J. Electrochem. Soc.* **2019**, *166*, F3305. [[CrossRef](#)]
151. Gao, X.; Yu, H.; Qin, B.; Jia, J.; Hao, J.; Xie, F.; Shao, Z. Enhanced water transport in AEMs based on poly (styrene–ethylene–butylene–styrene) triblock copolymer for high fuel cell performance. *Polym. Chem.* **2019**, *10*, 1894–1903. [[CrossRef](#)]
152. Deng, H.; Wang, D.; Wang, R.; Xie, X.; Yin, Y.; Du, Q.; Jiao, K. Effect of electrode design and operating condition on performance of hydrogen alkaline membrane fuel cell. *Appl. Energy* **2016**, *183*, 1272–1278. [[CrossRef](#)]
153. Zhang, J.; Zhu, W.; Huang, T.; Zheng, C.; Pei, Y.; Shen, G.; Nie, Z.; Xiao, D.; Yin, Y.; Guiver, M.D. Recent insights on catalyst layers for anion exchange membrane fuel cells. *Adv. Sci.* **2021**, *8*, 2100284. [[CrossRef](#)]
154. Ozen, D.N.; Timurkutluk, B.; Altinisik, K. Effects of operation temperature and reactant gas humidity levels on performance of PEM fuel cells. *Renew. Sustain. Energy Rev.* **2016**, *59*, 1298–1306. [[CrossRef](#)]
155. Parthasarathy, A.; Srinivasan, S.; Appleby, A.J.; Martin, C.R. Temperature dependence of the electrode kinetics of oxygen reduction at the platinum/Nafion® interface—A microelectrode investigation. *J. Electrochem. Soc.* **1992**, *139*, 2530. [[CrossRef](#)]
156. Williams, M.V.; Kunz, H.R.; Fenton, J.M. Operation of Nafion®-based PEM fuel cells with no external humidification: Influence of operating conditions and gas diffusion layers. *J. Power Sources* **2004**, *135*, 122–134. [[CrossRef](#)]
157. Natarajan, D.; Van Nguyen, T. Current distribution in PEM fuel cells. Part 2: Air operation and temperature effect. *AIChE J.* **2005**, *51*, 2599–2608. [[CrossRef](#)]
158. Truong, V.M.; Duong, N.B.; Wang, C.-L.; Yang, H. Effects of cell temperature and reactant humidification on anion exchange membrane fuel cells. *Materials* **2019**, *12*, 2048. [[CrossRef](#)]
159. Park, G.-G.; Sohn, Y.-J.; Yang, T.-H.; Yoon, Y.-G.; Lee, W.-Y.; Kim, C.-S. Effect of PTFE contents in the gas diffusion media on the performance of PEMFC. *J. Power Sources* **2004**, *131*, 182–187. [[CrossRef](#)]
160. Yassin, K.; Rasin, I.G.; Willdorf-Cohen, S.; Diesendruck, C.E.; Brandon, S.; Dekel, D.R. A surprising relation between operating temperature and stability of anion exchange membrane fuel cells. *J. Power Sources Adv.* **2021**, *11*, 100066. [[CrossRef](#)]
161. Machado, B.S.; Chakraborty, N.; Das, P.K. Influences of flow direction, temperature and relative humidity on the performance of a representative anion exchange membrane fuel cell: A computational analysis. *Int. J. Hydrog. Energy* **2017**, *42*, 6310–6323. [[CrossRef](#)]
162. Li, X.; Ke, C.; Qu, S.; Li, J.; Shao, Z.; Yi, B. High Temperature PEM Fuel Cells Based on Nafion®/SiO₂ Composite Membrane. In *Energy Storage in the Emerging Era of Smart Grids*; IntechOpen: London, UK, 2011.
163. Douglin, J.C.; Varcoe, J.R.; Dekel, D.R. A high-temperature anion-exchange membrane fuel cell. *J. Power Sources Adv.* **2020**, *5*, 100023. [[CrossRef](#)]
164. Yassin, K.; Rasin, I.G.; Brandon, S.; Dekel, D.R. Quantifying the critical effect of water diffusivity in anion exchange membranes for fuel cell applications. *J. Membr. Sci.* **2020**, *608*, 118206. [[CrossRef](#)]
165. Gao, X.; Yu, H.; Jia, J.; Hao, J.; Xie, F.; Chi, J.; Qin, B.; Fu, L.; Song, W.; Shao, Z. High performance anion exchange ionomer for anion exchange membrane fuel cells. *RSC Adv.* **2017**, *7*, 19153–19161. [[CrossRef](#)]
166. Mohanty, A.D.; Bae, C. Mechanistic analysis of ammonium cation stability for alkaline exchange membrane fuel cells. *J. Mater. Chem. A* **2014**, *2*, 17314–17320. [[CrossRef](#)]
167. Sturgeon, M.R.; Macomber, C.S.; Engtrakul, C.; Long, H.; Pivovar, B.S. Hydroxide based benzyltrimethylammonium degradation: Quantification of rates and degradation technique development. *J. Electrochem. Soc.* **2015**, *162*, F366. [[CrossRef](#)]
168. Marino, M.; Kreuer, K. Alkaline stability of quaternary ammonium cations for alkaline fuel cell membranes and ionic liquids. *ChemSusChem* **2015**, *8*, 513–523. [[CrossRef](#)]
169. Park, E.J.; Maurya, S.; Hibbs, M.R.; Fujimoto, C.H.; Kreuer, K.-D.; Kim, Y.S. Alkaline stability of quaternized Diels–Alder polyphenylenes. *Macromolecules* **2019**, *52*, 5419–5428. [[CrossRef](#)]
170. Li, H.; Tang, Y.; Wang, Z.; Shi, Z.; Wu, S.; Song, D.; Zhang, J.; Fatih, K.; Zhang, J.; Wang, H. A review of water flooding issues in the proton exchange membrane fuel cell. *J. Power Sources* **2008**, *178*, 103–117. [[CrossRef](#)]
171. Ji, M.; Wei, Z. A review of water management in polymer electrolyte membrane fuel cells. *Energies* **2009**, *2*, 1057–1106. [[CrossRef](#)]
172. Carlson, A.; Shapturenka, P.; Eriksson, B.; Lindbergh, G.; Lagergren, C.; Lindström, R.W. Electrode parameters and operating conditions influencing the performance of anion exchange membrane fuel cells. *Electrochim. Acta* **2018**, *277*, 151–160. [[CrossRef](#)]
173. Benziger, J.; Kimball, E.; Mejia-Ariza, R.; Kevrekidis, I. Oxygen mass transport limitations at the cathode of polymer electrolyte membrane fuel cells. *AIChE J.* **2011**, *57*, 2505–2517. [[CrossRef](#)]
174. Owejan, J.P.; Trabold, T.A.; Mench, M.M. Oxygen transport resistance correlated to liquid water saturation in the gas diffusion layer of PEM fuel cells. *Int. J. Heat Mass Transf.* **2014**, *71*, 585–592. [[CrossRef](#)]
175. Büchi, F.N.; Srinivasan, S. Operating proton exchange membrane fuel cells without external humidification of the reactant gases: Fundamental aspects. *J. Electrochem. Soc.* **1997**, *144*, 2767. [[CrossRef](#)]

176. Kim, T.; Kim, J.; Sim, C.; Lee, S.; Kaviany, M.; Son, S.; Kim, M. Experimental approaches for distribution and behavior of water in PEMFC under flow direction and differential pressure using neutron imaging technique. *Nucl. Instrum. Methods Phys. Res. Sect. A Accel. Spectrometers Detect. Assoc. Equip.* **2009**, *600*, 325–327. [[CrossRef](#)]
177. Mishler, J.; Wang, Y.; Mukundan, R.; Spendelow, J.; Hussey, D.S.; Jacobson, D.L.; Borup, R.L. Probing the water content in polymer electrolyte fuel cells using neutron radiography. *Electrochim. Acta* **2012**, *75*, 1–10. [[CrossRef](#)]
178. Wang, Y.; Wang, C.-Y. Dynamics of polymer electrolyte fuel cells undergoing load changes. *Electrochim. Acta* **2006**, *51*, 3924–3933. [[CrossRef](#)]
179. Yang, W.; Cha, D.; Kim, Y. Effects of flow direction on dynamic response and stability of nonhumidification PEM fuel cell. *Energy* **2019**, *185*, 386–395. [[CrossRef](#)]
180. Pasaogullari, U.; Wang, C.-Y.; Chen, K.S. Two-phase transport in polymer electrolyte fuel cells with bilayer cathode gas diffusion media. *J. Electrochem. Soc.* **2005**, *152*, A1574. [[CrossRef](#)]
181. Weber, A.Z.; Darling, R.M.; Newman, J. Modeling two-phase behavior in PEFCs. *J. Electrochem. Soc.* **2004**, *151*, A1715. [[CrossRef](#)]
182. Mukundan, R.; Davey, J.R.; Rockward, T.; Spendelow, J.S.; Pivovar, B.; Hussey, D.S.; Jacobson, D.L.; Arif, M.; Borup, R. Imaging of water profiles in PEM fuel cells using neutron radiography: Effect of operating conditions and GDL composition. *ECS Trans.* **2007**, *11*, 411. [[CrossRef](#)]
183. Su, H.; Sita, C.; Pasupathi, S. The effect of gas diffusion layer PTFE content on the performance of high temperature proton exchange membrane fuel cell. *Int. J. Electrochem. Sci.* **2016**, *11*, 2919–2926. [[CrossRef](#)]
184. Uchida, M.; Aoyama, Y.; Eda, N.; Ohta, A. Investigation of the microstructure in the catalyst layer and effects of both perfluorosulfonate ionomer and PTFE-loaded carbon on the catalyst layer of polymer electrolyte fuel cells. *J. Electrochem. Soc.* **1995**, *142*, 4143. [[CrossRef](#)]
185. Orogbemi, O.; Ingham, D.; Ismail, M.; Hughes, K.; Ma, L.; Pourkashanian, M. The effects of the composition of microporous layers on the permeability of gas diffusion layers used in polymer electrolyte fuel cells. *Int. J. Hydrog. Energy* **2016**, *41*, 21345–21351. [[CrossRef](#)]
186. Park, S.; Lee, J.-W.; Popov, B.N. A review of gas diffusion layer in PEM fuel cells: Materials and designs. *Int. J. Hydrog. Energy* **2012**, *37*, 5850–5865. [[CrossRef](#)]
187. Ismail, M.; Damjanovic, T.; Hughes, K.; Ingham, D.; Ma, L.; Pourkashanian, M.; Rosli, M. Through-plane permeability for untreated and PTFE-treated gas diffusion layers in proton exchange membrane fuel cells. *J. Fuel Cell Sci. Technol.* **2010**, *7*, 051016.1–051016.7. [[CrossRef](#)]
188. Ismail, M.; Borman, D.; Damjanovic, T.; Ingham, D.; Pourkashanian, M. On the through-plane permeability of microporous layer-coated gas diffusion layers used in proton exchange membrane fuel cells. *Int. J. Hydrog. Energy* **2011**, *36*, 10392–10402. [[CrossRef](#)]
189. Zhegur-Khais, A.; Kubannek, F.; Krewer, U.; Dekel, D.R. Measuring the true hydroxide conductivity of anion exchange membranes. *J. Membr. Sci.* **2020**, *612*, 118461. [[CrossRef](#)]
190. Wang, L.; Bellini, M.; Miller, H.A.; Varcoe, J.R. A high conductivity ultrathin anion-exchange membrane with 500+ h alkali stability for use in alkaline membrane fuel cells that can achieve 2 W cm⁻² at 80 C. *J. Mater. Chem. A* **2018**, *6*, 15404–15412. [[CrossRef](#)]
191. Dang, H.-S.; Jannasch, P. High-performing hydroxide exchange membranes with flexible tetra-piperidinium side chains linked by alkyl spacers. *ACS Appl. Energy Mater.* **2018**, *1*, 2222–2231. [[CrossRef](#)]
192. Zhegur, A.; Gjineci, N.; Willdorf-Cohen, S.; Mondal, A.; Diesendruck, C.; Gavish, N.; Dekel, D. Changes of anion exchange membrane properties during chemical degradation. *ACS Appl. Polym. Mater.* **2020**, *2*, 360–367. [[CrossRef](#)]
193. Mandal, M.; Huang, G.; Kohl, P.A. Highly conductive anion-exchange membranes based on cross-linked poly (norbornene): Vinyl addition polymerization. *ACS Appl. Energy Mater.* **2019**, *2*, 2447–2457. [[CrossRef](#)]
194. Pusara, S.; Srebnik, S.; Dekel, D.R. Molecular simulation of quaternary ammonium solutions at low hydration levels. *J. Phys. Chem. C* **2018**, *122*, 11204–11213. [[CrossRef](#)]
195. Douglin, J.; Singh, R.; Haj-Bsoul, S.; Li, S.; Biemolt, J.; Yan, N.; Varcoe, J.; Rothenberg, G.; Dekel, D. A high-temperature anion-exchange membrane fuel cell with a critical raw material-free cathode. *Chem. Eng. J. Adv.* **2021**, *8*, 100153. [[CrossRef](#)]
196. Li, Z.; He, X.; Jiang, Z.; Yin, Y.; Zhang, B.; He, G.; Tong, Z.; Wu, H.; Jiao, K. Enhancing hydroxide conductivity and stability of anion exchange membrane by blending quaternary ammonium functionalized polymers. *Electrochim. Acta* **2017**, *240*, 486–494. [[CrossRef](#)]
197. Li, N.; Guiver, M.D.; Binder, W.H. Towards high conductivity in anion-exchange membranes for alkaline fuel cells. *ChemSusChem* **2013**, *6*, 1376–1383. [[CrossRef](#)]
198. Paul, D.K.; McCreery, R.; Karan, K. Proton transport property in supported Nafion nanothin films by electrochemical impedance spectroscopy. *J. Electrochem. Soc.* **2014**, *161*, F1395. [[CrossRef](#)]
199. Wang, C.; Mo, B.; He, Z.; Xie, X.; Zhao, C.X.; Zhang, L.; Shao, Q.; Guo, X.; Wujcik, E.K.; Guo, Z. Hydroxide ions transportation in polynorbornene anion exchange membrane. *Polymer* **2018**, *138*, 363–368. [[CrossRef](#)]
200. Zelovich, T.; Tuckerman, M.E. Water layering affects hydroxide diffusion in functionalized nanoconfined environments. *J. Phys. Chem. Lett.* **2020**, *11*, 5087–5091. [[CrossRef](#)] [[PubMed](#)]
201. Gao, X.; Lu, F.; Dong, B.; Wu, A.; Sun, N.; Zheng, L. Anion exchange membranes with well-defined ion transporting nanochannels via self-assembly of polymerizable ionic liquids. *J. Mater. Chem. A* **2016**, *4*, 13316–13323. [[CrossRef](#)]

202. Dubey, V.; Maiti, A.; Daschakraborty, S. Predicting the solvation structure and vehicular diffusion of hydroxide ion in an anion exchange membrane using nonreactive molecular dynamics simulation. *Chem. Phys. Lett.* **2020**, *755*, 137802. [[CrossRef](#)]
203. Ziv, N.; Dekel, D.R. A practical method for measuring the true hydroxide conductivity of anion exchange membranes. *Electrochem. Commun.* **2018**, *88*, 109–113. [[CrossRef](#)]
204. Müller, J.; Zhegur, A.; Krewer, U.; Varcoe, J.R.; Dekel, D.R. Practical ex-situ technique to measure the chemical stability of anion-exchange membranes under conditions simulating the fuel cell environment. *ACS Mater. Lett.* **2020**, *2*, 168–173. [[CrossRef](#)]
205. Wang, L.; Brink, J.J.; Liu, Y.; Herring, A.M.; Ponce-González, J.; Whelligan, D.K.; Varcoe, J.R. Non-fluorinated pre-irradiation-grafted (peroxidated) LDPE-based anion-exchange membranes with high performance and stability. *Energy Environ. Sci.* **2017**, *10*, 2154–2167. [[CrossRef](#)]
206. Mahmoud, A.M.A.; Elsaghier, A.M.M.; Otsuji, K.; Miyatake, K. High hydroxide ion conductivity with enhanced alkaline stability of partially fluorinated and quaternized aromatic copolymers as anion exchange membranes. *Macromolecules* **2017**, *50*, 4256–4266. [[CrossRef](#)]
207. Lin, B.; Qiu, L.; Qiu, B.; Peng, Y.; Yan, F. A soluble and conductive polyfluorene ionomer with pendant imidazolium groups for alkaline fuel cell applications. *Macromolecules* **2011**, *44*, 9642–9649. [[CrossRef](#)]
208. Cao, X.; Novitski, D.; Holdcroft, S. Visualization of hydroxide ion formation upon electrolytic water splitting in an anion exchange membrane. *ACS Mater. Lett.* **2019**, *1*, 362–366. [[CrossRef](#)]
209. Eriksson, B.; Grimler, H.; Carlson, A.; Ekström, H.; Lindström, R.W.; Lindbergh, G.; Lagergren, C. Quantifying water transport in anion exchange membrane fuel cells. *Int. J. Hydrog. Energy* **2019**, *44*, 4930–4939. [[CrossRef](#)]
210. Ono, H.; Miyake, J.; Shimada, S.; Uchida, M.; Miyatake, K. Anion exchange membranes composed of perfluoroalkylene chains and ammonium-functionalized oligophenylenes. *J. Mater. Chem. A* **2015**, *3*, 21779–21788. [[CrossRef](#)]
211. Adachi, M.; Navessin, T.; Xie, Z.; Frisken, B.; Holdcroft, S. Correlation of in situ and ex situ measurements of water permeation through Nafion NRE211 proton exchange membranes. *J. Electrochem. Soc.* **2009**, *156*, B782. [[CrossRef](#)]